Development and optimization of a high-performance thermal reactor for metal hydride-based refrigeration machines

A thesis accepted by the Faculty of Energy-, Process- and Bio-Engineering of the University of Stuttgart
to fulfill the requirements for the degree of Doctor of Engineering Sciences
(Dr.-Ing.)

by

Alexander Michael Wimmer

born in Stuttgart

Main referee:	Prof. Dr. rer. nat. habil. André Thess
Co-referee:	Prof. Dr. rer. nat. habil. Lars Röntzsch
Date of oral exam:	14.01.2026

Institute for Building Energetics, Thermotechnology and Energy Storage at the University of Stuttgart

2026

Acknowledgement

This work could not be formed without the help of several persons that I would like to thank:

First of all, I would like to express my deepest thankfulness to my direct supervisor Inga Bürger. From the beginning she delighted me for the topic and believed in me through all the time even in the 'Death Valley' of my Ph.D. journey. I really appreciated the honest and constructive exchange, the super-fast feedback times and the personal collaboration in the daily work. From her I could learn a lot, not only on professional working but also personally.

A big thank also goes to my professor, Mr. Thess, for giving me the possibility to conduct my Ph.D. work in his institute. His strict physical and also economical point of view enriched this work and also my professional development a lot.

I also would like to thank Mr. Röntzsch for his commitment for the independent co-examination as a metal hydride expert with application focus.

Furthermore, I would like to thank all the colleagues of the research group 'Thermochemical Systems', with which I had the pleasure to collaborate. I could profit from the plenty peer-reviews and discussions on scientific questions but also methods, technical possibilities and representation styles. In this regard a special thank goes to Christian Brack for his technical support during the experiments and to my group leader Marc Linder, who encouraged me from time to time to take an abstracted view on my work and the application possibilities, but also had often very practical and pragmatic tips from his decades-long experience on metal hydrides.

But at all, this work would not be possible without my loving parents, who built in many years before the basis for me to start my Ph.D. journey. Also, during this time, they supported me personally and mentally a lot.

Last but not least and almost most important I would like to thank my betrothed Sina. Patiently she listened to many try-out presentations for Ph.D. seminars and conferences and stabilized me mentally during this periods. In the final phase of my Ph.D. journey, she supported me in the daily life and often had to miss me on free time.

There are certainly others who have contributed to making this modest contribution to the scientific world happen. I would like to take this opportunity to extend my sincere thanks to all of them.

Abstract

Hydrogen-powered vehicles can be a key component of a future decarbonized energy system. In the state-of-the-art, hydrogen is stored in 350 bar- or 700 bar-tanks for this purpose, whereby the energy expense for compression, accounting to approximately 15% (based on the lower heating value of hydrogen), reduces the overall efficiency of hydrogen-powered vehicles. By means of the thermochemical reaction of metal hydrides, parts of this energy can be converted into a heat pump effect in order to support or replace the conventional vehicle air conditioning system and thus increase the vehicle efficiency. The core of this work is the fundamental analysis and technological development of the metal hydride-based cooling system (MHCS) for vehicle applications.

In the course of the work, the dominating influences on the performance of the MHCS were identified to be the parameters for thermodynamic and kinetic of the metal hydride, the heat and mass transport properties and thermal mas of the reactor and the boundary conditions in terms of pressure, temperature and mass flow rate. A simplified model was built, which represents these influences, using a 0+1D approach. It enables the determination of the characteristics of the MHCS: On the one hand, a decreasing efficiency with increasing specific desorption mass flow and, and on the other hand, a maximum specific performance at an optimum specific desorption mass flow. Due to the generic modelling approach, the determined characteristics can also be transferred to other quasi-continuous and desorption-controlled thermochemical systems. The validated model was used for the systematic design of a lightweight reactor with increased thermal performance. A comprehensive characterization of the realized reactor verified the increased specific power of 80-300% compared to the state of the art. With an experimentally proven value of 229 W/kg_{MH} at a temperature lift of 40 K, the application-relevant target requirements were met and the basis was set for initial vehicle integration.

Kurzfassung

Wasserstoffbetriebene Fahrzeuge können eine Schlüsselkomponente in einem zukünftigen dekarbonisierten Energiesystem sein. Nach dem Stand der Technik wird Wasserstoff zu diesem Zweck in 350 bar- oder 700 bar-Tanks gespeichert, wobei der Energieaufwand für die Komprimierung von etwa 15% (basierend auf dem unteren Heizwert von Wasserstoff) die Gesamteffizienz von wasserstoffbetriebenen Fahrzeugen verringert. Durch die thermochemische Reaktion von Wasserstoff mit Metallhydriden kann ein Teil dieser Energie in einen Wärmepumpeneffekt umgewandelt werden, um die konventionelle Fahrzeugklimaanlage zu unterstützen oder zu ersetzen und so die Effizienz des Fahrzeugs zu erhöhen. Der Kern dieser Arbeit ist die grundlegende Analyse und technologische Weiterentwicklung der Metallhydrid-basierten Kältemaschine (MHKM) für Fahrzeuganwendungen.

Im Verlauf der Arbeit wurden die dominierenden Einflüsse auf die Leistung der MHKM identifiziert. Diese sind die thermodynamischen und kinetischen Parameter des Metallhydrids, die Wärme- und Stofftransporteigenschaften und die thermische Masse des Reaktors sowie die Randbedingungen in Bezug auf Druck, Temperatur und Massenstrom. Es wurde ein vereinfachtes Modell erstellt, das diese Einflüsse mit Hilfe eines 0+1D-Ansatzes darstellt und die Bestimmung der Charakteristiken der MHKM ermöglicht: Diese sind zum einen eine abnehmende Effizienz mit zunehmendem spezifischen Desorptionsmassenstrom und zum anderen eine maximale spezifische Leistung bei einem optimalen spezifischen Desorptionsmassenstrom. Aufgrund des generischen Modellierungsansatzes lassen sich die ermittelten Eigenschaften auch auf andere quasi-kontinuierliche und desorptionsgesteuerte thermochemische Systeme übertragen. Das validierte Modell wurde für den systematischen Entwurf eines Leichtbaureaktors mit erhöhter thermischer Leistung verwendet. Eine umfassende Charakterisierung des realisierten Reaktors verifizierte die erhöhte spezifische Leistung von 80-300% im Vergleich zum Stand der Technik. Mit einem experimentell nachgewiesenen Wert von 229 W/kg_{MH} bei einem Temperaturhub von 40 K wurden die anwendungsrelevanten Zielanforderungen erfüllt und die Grundlage für eine erste Fahrzeugintegration geschaffen.

Table of contents

Nomenclature, indices and abbreviations

Symbol	Description	Units
Formula symbols		
E	activation energy	J/mol
η_c	cooling efficiency	-
ΔH	reaction enthalpy	J/mol
m	mass	kg
$\dot{m}$	mass flow rate	kg/s
p	pressure	bar
Q	heat	J
$\dot{Q}$	heat flow	J/s
R	universal gas constant	J/(mol K)
ΔS	reaction entropy	J/(mol K)
T	temperature	K
x	reaction conversion	-
Indices		
0	standard conditions	
amb	ambient	
c	cold	
compr	compressor	
eq	equilibrium	
FC	fuel cell	
h	hot	
hi	high	
hc	half cycle	
ini	initial	
lo	low	
s	(heat) source	
t	tank	

Abbreviations

1D/0D/2D	zero-/one-/two-dimensional
α	solid solution phase
β	metal hydride phase
A	stable hydride forming metal
abs	absorption
B	unstable hydride forming metal
COP	coefficient of performance
des	desorption
DLR	German Aerospace Center
FC	fuel cell
FCEV	fuel cell electric vehicle
g	gaseous
H	atomic hydrogen
H_2	molecular hydrogen
LHV	lower heating value
M	metal
MH	metal hydride
MHCS	metal hydride cooling system
MHKM	Metallhydrid-basierte Kältemaschine
opt	optimal
PCT	pressure concentration temperature curve
R	reactor
R1a	reactor 1 filled with MH type a
s	solid
SCP	specific cooling power
VCS	vapour compression system

1. Introduction

1.1. Motivation

Great efforts are made worldwide to decarbonize the energy system, in which road transport is the second largest CO_2 issuer after the electricity sector, accounting for 16 % of the worldwide CO_2 emissions [1]. One option being pursued to decarbonize the transport sector is the use of hydrogen as an energy carrier and fuel for vehicles. Hydrogen can be produced using various production processes from renewable energy sources such as wind and solar energy. These include electrochemical electrolysis, in which hydrogen can be produced using renewable electricity, but also other processes such as thermochemical production using concentrated solar thermal energy. In vehicles, hydrogen can be used in a fuel cell or an internal combustion engine for propulsion, which is recently under development, especially for heavy-duty applications such as trucks, but also for buses and trains [2].

As an energy carrier, hydrogen has a high weight-specific energy density, which is higher than that of liquid hydrocarbons such as gasoline, kerosene or diesel. However, being gaseous at ambient conditions, hydrogen has the lowest density of all gases, which leads to a low energy storage density of only 3 kWh/m^3 related to the volume. The density of hydrogen must therefore be increased for technical utilization, which can be realized by different ways. One option is liquification, however, due to the low boiling point of 20.4 K at 1 atm, this requires very low temperatures and thus a high energy input for liquefaction and a high effort for thermal insulation. Another option is chemically bounded hydrogen, for example in liquid organic hydrogen carriers (LOHC), ammonia (NH_3), methanol (CH_3OH) or in metal hydrides (MH), all of which have certain advantages and disadvantages. The most obvious way to increase the density is the compression of the gaseous hydrogen. Therefore pressure tanks represent the most established storage technology for hydrogen in vehicles so far, using thick-walled carbon-fiber reinforced pressure cylinders at pressures of 350 or 700 bar [3].

However, the compression requires approximately 15% of the lower heating value (LHV) of hydrogen and thus reduces the efficiency of hydrogen powered vehicles [4]. Parts of this energy are reversibly stored in the compressed gaseous state of hydrogen and can be recovered. It can be calculated as the exergy of the closed pressure tank and amounts to 6%

of the LHV for a 700 bar-tank. In order to utilize this available energy potential, there exist few concepts in the literature based on mechanical expansion machines [5-7], but these are not used in the state of the art due to their technical complexity and low energy efficiency.

Another very promising concept is the open metal hydride cooling system (MHCS), a refrigeration system based on metal hydrides. It is driven by the pressure difference between the tank and the fuel cell and converts the available potential energy directly into a usable heat pump effect. As a dry solid sorption system, it has the advantage of no moving parts and shows the potential of a high efficiency, as 18% of the electrical fuel cell output can be generated as cooling power by known metal hydrides. At the same time, most vehicles require a refrigeration machine for air-conditioning of the passenger compartment, which is usually the largest auxiliary consumer and reduces the range by up to 20% [8]. In this case the open MHCS can be used as a replacement of the conventional refrigeration machine in order to significantly increase the efficiency of the vehicle by utilizing the available enthalpy in the hydrogen flow.

The technology of the open MHCS has been invented at the DLR and a functional prototype was already demonstrated in former works of this research group. The core of this work is at first an extended investigation of the open MHCS in order to gain a deeper understanding of the system and at second a further development of the reactor as its main component in order to meet application-relevant requirements.

1.2. Theoretical background

This thesis comprises a numerical as well as an experimental part. For the numerical model, the fundamentals of metal hydrides are essential and therefore given in the first subsection. In the second subsection an overview on metal hydride-based thermal machines is given, to discuss the numerical and experimental findings of this thesis in the context of comparable systems.

1.2.1. Fundamentals of metal hydrides

Metal hydrides (MH) are metals that are able to form a hydride phase by absorption of hydrogen. In most cases, this process is reversible and is accompanied by a thermal effect. The corresponding chemical reaction equation is formulated in Eq. (1).

$$\frac{2}{x}\,M(s) + H_2(g) \rightleftharpoons \frac{2}{x}MH_x(s) \qquad (\Delta H_f < 0) \qquad (1)$$

In this equation the solid (s) reaction partner M can be an individual metal, an intermetallic compound or an alloy. The enthalpy of formation is typically referred to one mol per molecular hydrogen. During the absorption process gaseous (g) hydrogen is adsorbed on the surface, dissociates to its atomic form and enters the metal lattice. Another way of hydrogen loading is via an electrolyte, where hydrogen is already in its atomic form. For common intermetallic compound hydrides, the hydrogen occupies interstitial sides in the metal lattice, leading to a lattice expansion of 10-30 % [9]. The absorption process is exothermic, whereas the desorption as the reverse reaction represents an endothermic process. For many intermetallic hydrides the absorption and desorption process show a fast intrinsic kinetic and full conversion within seconds. Due to the release or uptake of thermal energy during the process, the reaction in an application context is often referred to as thermochemical reaction with MH as a thermochemical material. In this regard MHs belong to the group of other thermochemical gas-solid reaction system, as they are for instance hydroxides e.g. calcium hydroxide Ca(OH) [10], salt hydrates like $SrBr_2$ [11] or metal oxides [12].

Besides the specific MH material considered in this work, there is a large variety of metal hydrides that are investigated and known in literature[13, 14] . One way of classify them is by the type of bond, which divides them into intermetallic and conversion materials. The most common class of metal hydrides is the one of intermetallic compounds. This class includes the low temperature hydrides that are relevant for this work, since they are able to generate a cooling effect at a pressure level slightly above atmospheric pressure, which is typical for the fuel cell supply.

Such hydrides of intermetallic compounds are mostly ternary hydrides, consisting of an element A, that forms a relatively stable hydride under normal conditions (requiring several hundreds of °C to desorb hydrogen, e.g. TiH_2) and an element B that forms only an unstable hydride (requiring thousands of bar to absorb hydrogen, e.g. NiH). Compounds of these elements show intermediate hydrogen absorption properties and are able to absorb significant

amounts of hydrogen near ambient conditions. Thus, intermetallic MHs can be divided into types of AB, AB_5, or A_2B, but also other combinations like AB_3 or A_2B_7. Common examples are for instance TiFe, $TiMn_2$, $LaNi_5$ or Zr_2Fe. Most AB_5-type MHs show a hydrogen storage capacity of 1.5 wt.-% whereas AB_2-type MHs, as the one used in this work, show a capacity of mostly 1.8 wt.-%.

The absorption of hydrogen in any of the interstitial metal hydrides proceeds in several steps. At first gaseous hydrogen is attracted by Van der Vaals forces to the surface where it forms a physisorbed state. After overcoming an activation barrier, the hydrogen molecule dissociates, diffuses into the metal lattice as atomic H and forms a solid solution, commonly referred to as α-phase. In this phase for small hydrogen concentrations the concentration is proportional to the square root of the pressure (Sievert's law). If the pressure increases over a certain saturation pressure the hydride phase (β-phase) starts to grow, where hydrogen atoms fill interstitial sides mostly in a tetrahedral or octahedral way. The hydride forming is an exothermic process since the entropy of the hydride phase is lower than the one of the solid metal and the gaseous hydrogen phase. With an heat release in the order of 20-150 kJ/mol_{H2}, the energy is much higher than that of a pure absorption material (4-6 kJ/mol_{H2}) [15].

Considering the Gibb's phase rule, the emergence of a new phase reduces the degrees of freedom to only one. Therefore, during the formation of the β-phase the reaction temperature and the reaction pressure are coupled, leading to a constant pressure at an isothermal reaction. After the β-phase is completely formed, the pressure decreases further due to hydrogen solution in the β-phase, as depicted in Fig. 1.

Using the concept of chemical potentials one can deduce the relationship between reaction pressure and temperature to Eq. (2), that is known as the Van't Hoff equation of MHs in literature [14].

$$\ln\left(\frac{p}{p_0}\right) = \frac{\Delta H}{RT} - \frac{\Delta S}{R} \tag{2}$$

According to this equation the equilibrium temperature increases with increasing gas pressure and vice versa. Furthermore, it shows that the enthalpy and entropy of formation determine the plateau pressure of the hydride phase developing at a certain temperature. It is referred to as the thermodynamic property of a respective MH and can be tailored by the partial substitution of elements in the host lattice [16].

For the practical application of MHs, as in the open MHCS, it is important that the equilibrium pressure slightly increases under isothermal conditions as the reaction progresses. Accordingly, in the pressure-compositions-temperature (PCT) curve of the MH, see Fig. 1, instead of an ideal flat plateau, a certain plateau slope is observable. The corresponding plateau slope factor is commonly calculated at the plateau mid according to $\mathrm{d}\ln(P)/\mathrm{d}\left(\frac{\mathrm{H}}{\mathrm{M}}\right)$. Moreover, most practical used hydrides show a lower equilibrium pressure at desorption than for absorption, that is denoted as hysteresis. The corresponding hysteresis factor is commonly calculated as $\ln(P_{\mathrm{abs}}/P_{\mathrm{des}})$ [14].

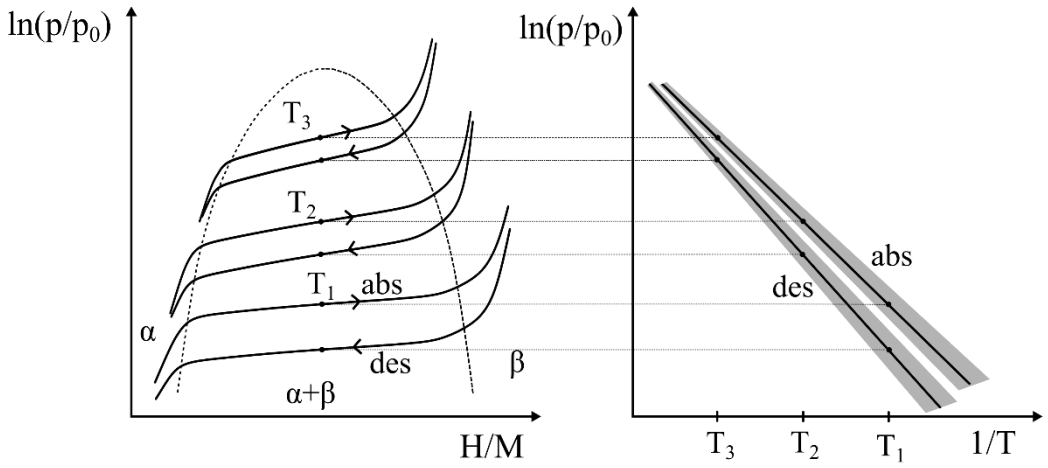

Fig. 1: Schematic representation of pressure concentration curves on different temperatures (PCTs) and respective van't Hoff plot

Besides the chemical thermodynamic, that determines the working temperature for the applied gas pressure, also the reaction dynamic is of special importance for a practical use of MHs, especially for a dynamically operated applications as the open MHCS. Instead of resolving the individual reaction steps by certain models, a general empirical expression (Eq. (3) is commonly used according to the recommendations of the International Confederation for Thermal Analysis and Calorimetry (ICTAC) [17]. It is also used in the modelling part of this thesis.

$$\frac{\mathrm{d}x}{\mathrm{d}t} = \mathrm{k}(T)\mathrm{f}(\alpha)\mathrm{h}(P) \tag{3}$$

For reversible gas-solid reactions the pressure function is proposed to be $\mathrm{h}(P) = 1 - p/p_{\mathrm{eq}}$ considering the actual pressure p of the gaseous phase and the pressure at the equilibrium state

p_{eq}. It shows that the reaction rate becomes faster, if the distance from the equilibrium is increased, and stops if the equilibrium is reached. The term $\mathrm{k}(T)$ accounts for the temperature dependence and is typically expressed with the Arrhenius equation as $\mathrm{k}(T) = A\exp(-E/(RT))$, where A is the kinetic parameter, E the activation energy and R the universal gas constant. The conversion dependence is represented by the function $\mathrm{f}(x)$, for which a large variety of formulations is available in literature for different chemical reactions including solid-state reactions [17]. For typical intermetallic MHs, as used in this work, it is reported in literature that a first order reaction can be assumed [18], leading to the expression of $\mathrm{f}(x) = 1 - x$.

Due to the variety of MHs with a different equilibrium pressure at room temperature, their reversible high volumetric absorption property, which is coupled with a strong thermal effect, and other characteristic effects such as lattice expansion and disintegration, there is a wide range of possible application for MHs. It ranges from neutron shielding in nuclear technology [19] over gas purification [20] and the use as a getter material in vacuum applications [21] to even permanent magnet production [22].

The most application-related research activities focus on solid state hydrogen storage [23], since it enables a safe method to store hydrogen on low pressure (<10 bar) and room temperature at a very high volumetric energy density. Due to the atomic incorporation in the metal lattice the volumetric energy density in MHs is even higher than in liquid hydrogen. However, intermetallic hydrides in this pressure and temperature domain (<100 °C) do not exceed gravimetric energy densities above 2.5 wt.-% [14], which makes them unattractive for mobile storage e.g. in hydrogen powered vehicles. Although there are also complex and interstitial hydrides based on light-metals as magnesium, aluminum or boron, reaching capacities above 7 wt.-%, they show other drawbacks as a high heat of formation at temperatures higher than 100 °C. It requires sufficient waste heat on elevated temperature or an additional thermal energy storage to prevent efficiency loss [24]. Thus, MH are currently not a widely spread technology for hydrogen storage.

Another application, which has already been studied for several decades and which is still intensively investigated in recent times is the thermal MH compressor [25-27]. Hydrogen is absorbed at low pressure (e.g. ambient or electrolyser supply pressure) while releasing the heat of absorption to the ambient. By heating-up the MH, the equilibrium pressure is increased according the Van't Hoff equation, Eq. (2). Then, hydrogen is discharged at a higher pressure

while the endothermic desorption takes up heat from a source above ambient temperature. This process represents a solid state hydrogen compression without moving parts and therefore no noise, vibration and mechanical wear. Moreover, the driving-force is heat that allows to use waste heat and reduce operating cost. Many experimental set-up MH compressors are published, demonstrating a compression from a few bar to below 100 bar with a heat source of 100-150 °C [28].

The substantial heat of reaction (20-60 kJ/mol for intermetallic hydrides) also suggests to use the thermal effect of MHs for a purely thermal application, like a thermal energy storage or thermal machine (heat pump or refrigerator) [29, 30]. As a thermal energy storage, MHs show a comparable and often better volumetric energy density compared to sensible or latent heat-based storage systems and no thermal losses in the storing period [22]. The released hydrogen, that is accompanied with heat uptake, can be captured for instance in a pressure vessel or in a second MH having a lower equilibrium temperature. Such a thermal energy storage, consisting of two MH reactors, was investigated for instance to assisting cold start for vehicles with combustion engine, where afterwards waste heat is stored again during operation to regenerate the cold start device [31]. A similar system was developed for a hydrogen powered vehicle, where the existing hydrogen source (tank) and hydrogen sink (fuel cell or combustion engine) are used to omit the requirement of a second MH [32]. Besides the application as a thermal energy storage, the thermal effect of MHs can also be utilized to realize a quasi-continuously operating thermal machine like the open MHCS. Such kind of systems will be presented in the next section in more detail.

1.2.2. Metal hydride-based thermal machines

Next to the open MHCS there are two other types of thermal machines as shown in Fig. 2, namely the thermal-driven and the compressor-driven heat pump/refrigeration system. They represent energy converters rather than storage systems, thus there are two commonly used figures of merit to evaluate these kind of systems. They are at first the specific cooling power (SCP), calculated by the cooling power $\dot{Q}_c$ related to the utilized amount of MH mass m_{MH}, Eq. (4), and the efficiency in terms of the coefficient of performance (COP), calculated as the cooling power related to the energy expend, confer Eq. (5). The energy input in this regard could be either mechanical work for the compressor or a heat flow $\dot{Q}_s$ from a driving heat source.

$$\mathrm{SCP} = \frac{\dot{Q}_\mathrm{c}}{m_\mathrm{MH}} \tag{4}$$

$$\mathrm{COP} = \begin{cases} \dfrac{\dot{Q}_\mathrm{c}}{P_\mathrm{compr}} & \mathrm{compressor-driven} \\ \dfrac{\dot{Q}_\mathrm{c}}{\dot{Q}_\mathrm{s}} & \mathrm{thermally-driven} \end{cases} \tag{5}$$

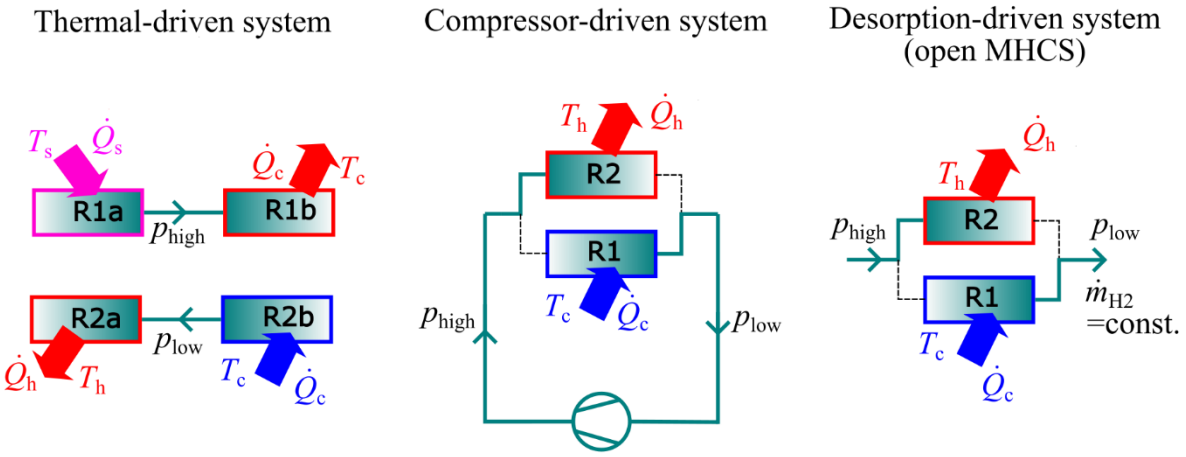

Fig. 2: Overview of metal hydride-based thermal machines

Thermal-driven heat pump/refrigerator and heat transformer

The concept with two coupled MH reactors that contain MHs with different equilibrium temperatures can be extended from a thermal energy storage to a quasi-continuously operating thermal-driven heat pump, firstly developed in the 1970s [33]. In this regard it must be distinguished between the heat-upgrading version and temperature-upgrading version. The heat upgrading version uses a heat source on high temperature in order to pump heat from a low to an intermediate temperature level. Dependent on the temperature level for ambient conditions, that is either on the low or the intermediated level, the version is denoted as heat pump or refrigeration machine, respectively. In contrast to this heat-upgrading version, there is also a temperature-upgrading version of this system (also referred to as heat transformer). This version produces usable heat on a higher temperature than the input heat was provided

on (mostly waste heat or solar heat) by releasing a part of the provided heat to a sink on a lower temperature level (mostly ambient).

Common to both versions of the thermal-driven systems is a batch-like cyclical behavior in two half-cycles, which requires two reactor pairs (4 reactors in total) to ensure continuous production of usable heat or cold. An comprehensive review on the progress of thermal-driven systems can be found in [29]. Similar systems are known based on other chemical systems, for instance other dry sorption systems like zeolite/water but also liquid sorption systems based on ammonia [34]. One of the main challenges is the achievement of a high COP and a high SCP, since it determines the size, weight and cost of the system. In this regard the requirements for the reactor design are well known. It has to facilitate a good heat and mass transfer into the reaction bed, but on the same time it has to show a low heat capacity, in order to reduce sensible heat losses caused by the alternating batch-like operation.

Compressor-driven MH heat pump/refrigerator

A derivate of the above mentioned thermal-driven system is the compressor-driven MH heat pump/refrigerator. It represents a simpler configuration, that comes along with only two reactors instead of four and uses just one type of MH. It replaces the second MH, which generates the pressure difference in the heat-driven system, by a mechanical or electrochemical hydrogen compressor. First proposed by [35], it was later investigated than the heat-driven system and since then less intensively studied compared to the heat-driven one. The challenges for this system are again the achievement of a high SCP and a high COP under a relevant temperature lift. However, due to the system configuration consisting of only 2 reactors instead of 4, in principle a higher SCP is possible, leading to a lower system mass, less space requirement and investment costs compared to the thermal-driven system. A summary of the corresponding experimental works in literature is given in Tab. 1 showing the reported SCP, COP and achieved temperature lift.

Since the energy input for this system is mechanical energy instead of heat, it represents a competitor to conventional vapor compression system. The study of Magnetto et al. experimentally demonstrated the achievement of a comparable COP of 2.9 at 20 K temperature lift. In this study they considered a mechanical compressor, as most of the reported studies on the compressor-driven system did. Tao et al., firstly, investigated the use of a highly efficient electrochemical compressor in a numerical study [36]. They showed that

it is beneficial especially for small power classes where mechanical compressors show a bad efficiency. The study revealed a possible COP of 3.4, that is higher than the COP of most commercial vapor compression systems, considering realistic conditions (5 °C and 45 °C for cooling and heating respectively).

Tab. 1: Literature overview of compressor-driven MH heat pumps/refrigerators

Author	Year	MH material	Reactor concept	Air-/water-cooled	t_{hc} [s]	Pressure ratio [-] (p_{max} [bar] / p_{min} [bar])	ΔT [K] (T_{hot} [°C] |T_{cold} [°C])	SCP [W/kg$_{MH}$]	COP [-]
Kim et al. **[37]**	1998	$Ca_{0.4}Mn_{0.6}Ni_5$	Copper plated pellets in brass tube (19.1 mm OD) with outer fins	air-cooled concept (water-cooled tests)	120	10 (27/2.7)	< 6 (22|22)	800	-
Park et al. **[38]**	2001	$Zr_{0.9}Ti_{0.1}Cr_{0.55}Fe_{1.45}$	Powder bed in copper tubes (15 mm OD) with heat-conducting discs of aluminum mesh	Air-cooled	156	18 (18/1)	~12 (~17|~29)	292	-
Park et al. **[39]**	2002	"	"	"	180	12.5 (10/0.8)	~26 (~6 | ~32)	411	1.8
Magnetto et al. **[40]**	2006	Rare-earth based MH	Cooper tubes (3.125 mm OD) with internal alloy support structure, tubes as spiral with outer fins	Air-cooled	210	4.4 (8/1.8)	~20 (~17|~37)	319	2.9
Muthukumar et al. **[41]**	2016	$LmNi_{4.91}Sn_{0.15}$	Powder bed in 103.4 mm ID stainless steel vessel with 60 inner cooling tubes of 6.35 mm OD	Water-cooled	240	15 (15/1)	5 (20|25) 10 (15|25) 25 (10|35)	54 35 29	2.2 1.7 1.3
Jana et al. **[42]**	2023	$La_{0.8}Ce_{0.2}Ni_5$	Powder bed in 19 stainless steel tubes (25.4 mm OD) surrounded by shell	Water-cooled	240	12.8 (9/0.7)	10 (20|30) 15 (20|35) 20 (10|30)	36 29 19	1.0 0.7 0.5

* for air-cooled systems the mean outlet air temperatures are stated, for water-cooled systems the water inlet temperatures are stated

Desorption-driven open heat pump/refrigerator

The third system in this context is the open MHCS and considered in this thesis. It takes advantage of an available hydrogen infrastructure in a hydrogen powered vehicle and thus omits the requirement of a second MH or a compressor, in contrast to the both closed systems described above. Instead, the open MHCS uses the already available pressure difference and therefore an existing potential energy. From an energetic point of view, the energy input was spent beforehand by the compressor of the refueling station to refill the tank. Thus, no efficiency in terms of the COP can be applied for the open system. Instead, the cooling efficiency η_c is used, which is defined in Eq. (6) as the actual cooling power divided by the maximum cooling power determined by the desorption enthalpy ΔH_{des} of the MH multiplied with the hydrogen flow rate. The cooling efficiency is therefore explicitly not a thermodynamic efficiency, but a material or application related one.

$$\eta_{\mathrm{c}} = \frac{\dot{Q}_{\mathrm{c}}}{\Delta H_{\mathrm{des}}\, \dot{m}_{\mathrm{H_2}}} \tag{6}$$

Fig. 3 (a) shows the operation principle, consisting of two half cycles, next to the temperature-pressure-correlation of the MH in Fig. 3 (b), which represents the basis of the heat pump functionality. In the first half cycle reactor R1 desorbs hydrogen on low pressure to the hydrogen consumer (e.g. fuel cell). According to the equilibrium correlation, the required heat for desorption is taken up on a temperature below the ambient, generating cold. At the same time reactor R2 is absorbing hydrogen from the pressure tank on high pressure, releasing heat to the ambient on high temperature, respectively. As soon as the desorbing reactor R1 cannot maintain the hydrogen supply to the fuel cell any more, the first half cycle is finished and the hydrogen valves are switched. In the second half cycle, reactor R1 is recharged with hydrogen and now releases the previously uptaken heat to the environment at a higher level, which represents a heat pump effect. Simultaneously, reactor R2 is now the cold generating reactor while it supplies hydrogen to the fuel cell. The alternating absorption and desorption of the two reactors in two half cycles represent the quasi-continuous operation principle of the open MHCS.

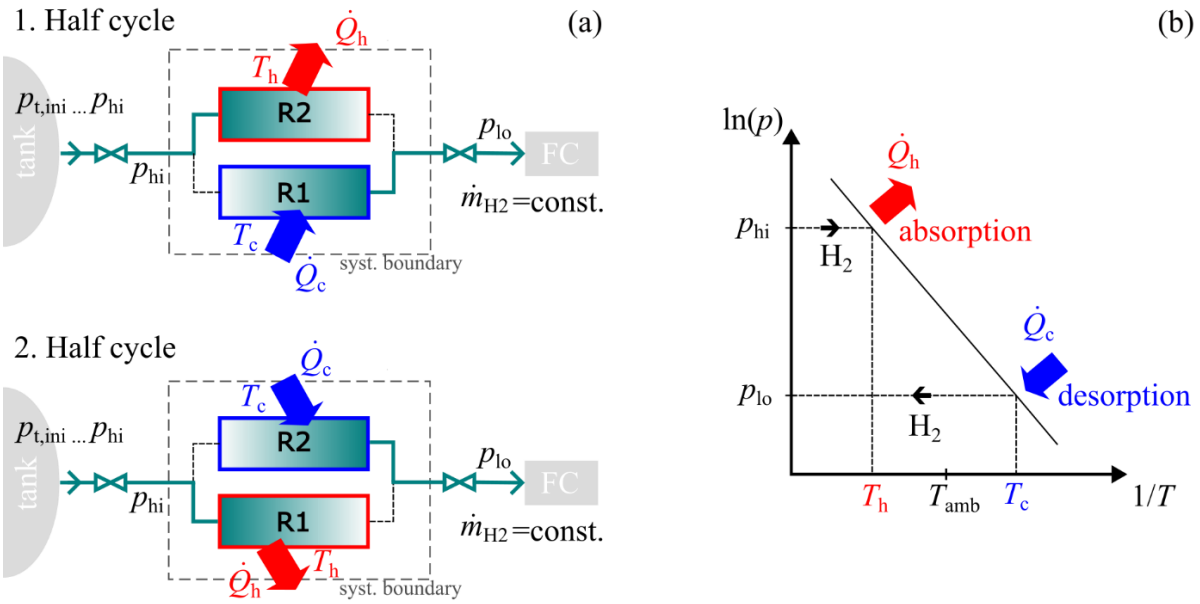

Fig. 3: Operation principle of the open metal hydride cooling system (a), a related representation of the process in the van't Hoff plot (b)

The system can also be denoted as desorption-driven MH heat pump/refrigeration system, since it is coupled directly with a hydrogen consumer at the outlet of the desorbing reactor, which controls the operation. Similar to the compressor-driven system, the MHCS has the same advantage in terms of SCP due to the requirement of only two reactors.

The MHCS was first proposed by Linder et al. to be used in the air-conditioner of a hydrogen powered vehicle where it could omit the extra energy that is usually required for air-conditioning [43]. Although the related experimental works demonstrated the generation of cold at 13 °C and at a heat sink temperature of 35 °C, by using vehicle relevant pressure levels of 50 and 6 bar for absorption and desorption, the system was not investigated at application-realistic conditions. Specifically, the experiments were conducted at a constant outlet pressure, whereas a constant hydrogen flow rate represents a more realistic boundary condition in a hydrogen powered vehicle due to the consumption of the fuel cell or hydrogen engine.

Therefore, in later experimental works, Weckerle et al. coupled the open MHCS directly to a fuel cell, which thus induces a constant hydrogen flow rate at the desorption reactor [44]. Furthermore, a novel reactor concept was used in that study, in order to reach a reasonable high SCP. Based on a plate heat exchanger the reactor realized a very small bed thickness that reduced the heat transfer limitation [45]. With this reactor and under application-realistic operation, an SCP of 276 W/kg$_{MH}$ was reached at the reference condition of 10 °C cold and 30 °C hot side temperature. However, with a ratio of the empty reactor mass related to the

incorporated MH mass of 3.2, the system still showed a very high mass of 15 kg per kilowatt cooling power. Moreover, further experiments for higher temperature lifts than 10 K showed a drastically reduced SCP, for instance only 61 W/kg_{MH} at 13 °C cold side temperature. Moreover, only a maximum temperature lift of 22 K was achieved, that is not high enough for vehicle application. Therefore, further technological development in terms of SCP, total system mass and achieved temperature lift is required to make the promising technology of the open MHCS suitable for vehicle applications.

1.3. Research question and aim of thesis

The works of Linder and Weckerle et al. represent the only published studies in literature on the open MHCS. Hence it is less investigated than the compressor-driven system or the older heat-driven system, leading to lack of understanding for this specific type of system.

In general, the reactor requirements for a high-performance MH reactor are known from the thermal and compressor-driven systems and also apply for the open system. However, the special configuration of being coupled directly to a hydrogen consumer supposes that there are special characteristics that have additionally to be considered. Such characteristics are known in literature [46] for general thermochemical gas-solid systems, as well the specific characteristics for the compressor- and thermal-driven system are known [47, 48], but yet have not been investigated for the open MHCS. However, they are of upmost importance for designing and sizing an optimal reactor for a particular application. It represents the research gap, which has to be closed in order to answer the following research question:

'How could a further developed open MHCS system look like that is suitable for vehicle integration?'

By defining the vehicle suitability in more detail, the technological aims for this work are deduced. At first, a SCP as high as possible is crucial since in vehicles the available space and the allowed mass addition is mostly limited. In this regard a higher SCP than reported in literature is aimed for. At second, a temperature lift exceeding 30 K has to be reached, in order to meet the requirements of vehicle air-conditioning systems and therefore facilitate its application. It was even not reached so far by an open- or compressor-driven system. At third, as much as possible from the available potential energy of the pressure tank has to be used in order to generate as much energy saving by the use of the open MHCS.

In conclusion the system must be better understood in order to build up an optimal reactor which reaches application suitability. Therefore, a systematic approach has to be found, implemented and validated, building the scientific core of this thesis. It was successfully developed and is presented in the following two peer-reviewed journal articles and in one article manuscript that is already submitted and aimed to published in a peer-reviewed journal as well.

2. Publications

Parts of this study have been presented in the following international conferences:

Wimmer, Alexander und Linder, Marc Philipp und Bürger, Inga (2024) *Using potential energy from pressure tanks in fuel cell vehicles for powering an innovative air-conditioning process based on metal hydrides.* 24th World Hydrogen Energy Conference (WHEC), 23-27.06.2024, Cancun, Mexico

Wimmer, Alexander und Linder, Marc Philipp und Bürger, Inga (2024) *Using the potential energy from high pressure tanks in fuel cell vehicles for powering an innovative air-conditioning process based on metal hydrides.* European Hydrogen Energy Conference (EHEC), 06.-08.03.2024, Bilbao, Spain

Wimmer, Alexander und Feierfeil, Steffen und Linder, Marc Philipp und Bürger, Inga (2022) *Improved reactor design for a metal hydride refrigeration system in hydrogen powertrains.* 23rd World Hydrogen Energy Conference (WHEC), 26-30.06.2022, Istanbul, Turkey

Pöhl, Joshua und Wimmer, Alexander und Bürger, Inga und Kordel, Markus und Heckert, Florian (2021) *Improving driving range for FCEVs by use of an innovative metal hydride air-conditioning system.* World Hydrogen Technology Convention, 20-24.06.2021, online

During the work on this study, the following theses related to the present work have been supervised:

Christ, Marcel (2024) *Entwicklung eines Metallhydridreaktors zur Klimatisierung von Brennstoffzellenfahrzeugen.* Bachelorarbeit, Hochschule Osnabrück

Lohnert, Elena Katharina (2023) *Charakterisierung des thermodynamischen Gleichgewichts von Metallhydriden zur Anwendung in Wärmepumpen auf Wasserstoff-Metallhydrid-Basis.* Bachelorarbeit, Hochschule Fresenius

Feierfeil, Steffen (2022) *Untersuchung von Maßnahmen zur Wärmeübergangserhöhung an einem Reaktor für eine Metallhydrid-Kältemaschine.* Masterarbeit, Universität Stuttgart

Zörlaut, Jakob (2021) *Konstruktion und Aufbau eines Reaktormoduls für eine Kältemaschine auf Metallhydridbasis.* Bachelorarbeit, Hochschule Esslingen

2.1. Paper I: Model development

As a systematical approach in order to meet the technological targets for the MHCS, the development of a mathematical model was chosen. The model should facilitate the analysis of the system behavior and quantitatively show parameter influences on the performance of an open MHCS. In this regard the particular research question for Paper I can be formulated as follows:

'How could a software-based pre-design tool look like to facilitate a fast and easy analysis and optimization of a reactor for a quasi-continuous gas-solids system such as the open MHCS?'

A steady-state model was built up considering the energy balance over a recurring half cycle by the concept of lumped masses. It focusses on the two key effects: The thermal losses due to the MH and especially the reactor mass, as well as the heat-and mass transport limitations on the reaction rate. The core of the model is the determination of the reaction conversion at different conditions. It depends on the material properties, the heat and mass transport inside the reactor and the boundary parameters. Therefore, the conversion-depended equilibrium relation, in form of PCTs of the MH, is combined with its kinetic equation and a steady-state one-dimensional temperature and pressure profile in the reactor. The calculated reaction conversion at a certain desorption mass flow together with the sensible losses finally determine the net thermal power and efficiency. The numerical computation of the governing equations was implemented based on common Open Source libraries in the python programming language and thus needs no software licenses. The model was validated with available experimental data from the studies of Weckerle et al [49].

As a main outcome, the results revealed a strong effect of the specific discharge rate on the reaction conversion leading to a characteristic maximum in the SCP at an optimum discharge rate. Furthermore, this effect leads to a decreasing efficiency with increasing discharge rate showing that power and efficiency are in conflict with each other. Moreover, in this Paper I a parameter study was conducted on the basis of the validation reactor. It showed that with the used MH material, under the application realistic pressure boundaries of 35 and 5 bar, the SCP at reference temperatures (20 °C and 30 °C) could be increased by a factor of 5 if ideal heat and mass transport conditions could be provided and even 10, if the reactor heat capacity can be further omitted.

Applied Thermal Engineering 241 (2024) 122250

Contents lists available at ScienceDirect

Applied Thermal Engineering

journal homepage: www.elsevier.com/locate/apthermeng

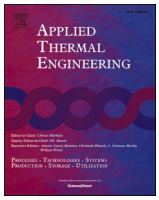

Research Paper

Lumped model for a quasi-continuously operating open metal hydride heat pump system

Alexander Wimmer *, Marc Linder, Inga Bürger

Institute of Engineering Thermodynamics, German Aerospace Center (DLR), Pfaffenwaldring 38-40, 70569 Stuttgart, Germany

ARTICLE INFO

Keywords:
Thermochemical heat pump
Metal hydride
Lumped model
Quasi-continuous operation
Reactor design

ABSTRACT

Hydrogen as a potential future fuel for fuel cell vehicles is mostly stored in high-pressure tanks at 350 or 700 bar, which requires energy-intense compression of typically 15 % of the lower heating value. For the recovery of parts of the compression work, a promising possibility is the usage of an open metal hydride heat pump. Similarly to other sorption-based heat pump systems, in order to reach high specific thermal power, it is crucial to find a trade-off in the design and operation of the reactor between two main factors: enabling fast reaction dynamics and reducing losses due to temperature switches. The present work introduces a steady-state model with lumped metal hydride and reactor mass considering one-dimensional heat and mass transfer, which is able to quickly predict the corresponding specific thermal power and efficiency. A special focus is on the calculation of the non-complete conversion due to an operation at constant gas flow. The model is validated with existing experimental data over a broad range of operation conditions in terms of metal hydride specific hydrogen mass flow (1.6–7.6 g_{H2} min^{-1} kg_{MH}^{-1}) and temperature boundary conditions (cold side temperature: 13–25 °C, hot side temperature: 24–42 °C). It is capable of describing the specific thermal power and the efficiency as the two main performance indicators with a suitable accuracy. To give an example of the applicability of the developed tool, a generic discussion of the performance limitations of the selected reactor design is carried out, indicating that the reactor of the validation experiment is mainly mass transport limited.

1. Introduction and operation principle

In order to transform our present energy system towards a CO_2-emmision-free system, electrical energy storage in gaseous or liquid chemical bonds is considered to play an important role [1]. Electrochemical electrolysis and other technologies allow electricity to be converted to hydrogen which can be stored in its pure form and used as a fuel for stationary or mobile applications. For onboard storage of compressed hydrogen in vehicles pressure vessels for 700 bar and 350 bar are established [2]. Nevertheless, a significant amount of energy is needed to compress the hydrogen during the refueling process, accounting for approximately 15 % of the hydrogen's energy content in terms of lower heating value [3,4]. The reusable stored potential energy of a 700 bar tank can be calculated to be 6 % of the hydrogen's energy content considering expansion to the ambient pressure. Conventionally however the hydrogen gas is simply throttled down via a pressure reducer to the fuel cell working pressure slightly above ambient pressure (<3 bar) whereas the potential energy of the compressed gas is dissipated [5]. In the state of research, there are options to utilize the potential energy from the compressed gaseous state. The most obvious one using a mechanical machine as a piston or turbo expander is discussed in [6]. Another promising and more widely studied way to recover this work was first proposed by Linder et. al [7] using an open metal hydride system. In contrast to thermally driven or compressor-driven closed metal hydride heat pumps [8–10] this system utilizes the potential energy of the high-pressure on-board tank and converts it directly into a heat pump effect. The heat pump effect can be used for heating or cooling purposes in fuel cell electric vehicles with a potential to reach a cooling or heating power of approximately 18 % of the fuel cell's electrical power. The first experiments with an open metal hydride heat pump by Linder et. al. and Maier et al. [7,11] were conducted on the low-pressure outlet with a fixed pressure boundary condition leading to a highly fluctuating hydrogen outlet flow, which does not fit practical consumption profiles of a real hydrogen consumer for instance of a fuel cell. Further experiments by Weckerle with a newly designed reactor [12] investigated the operation on a constant outlet flow to a hydrogen sink in the form of a real operating fuel cell and obtained a specific thermal power of 276 W/kg_{MH} at a temperature lift of 10 K [13]. Several

* Corresponding author.
E-mail address: alexander.wimmer@dlr.de (A. Wimmer).

https://doi.org/10.1016/j.applthermaleng.2023.122250
Received 26 October 2023; Received in revised form 13 December 2023; Accepted 17 December 2023
Available online 23 December 2023

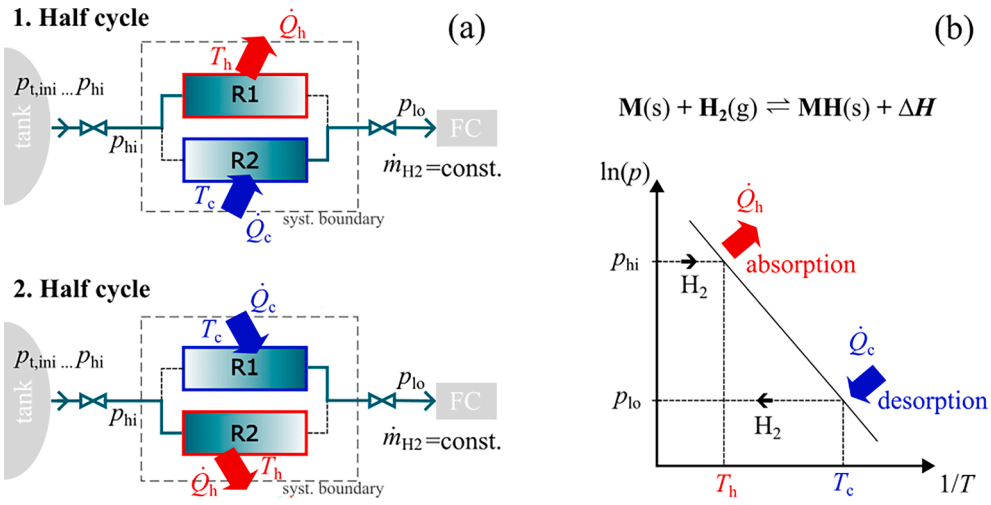

Fig. 1. (a) Operation principle consisting of two half cycles, (b) absorption and desorption on different pressure levels drawn in a Van't Hoff plot.

laboratory reactor prototypes for mobile applications are summarized and discussed in [14]. The application of the open metal hydride heat pump in a fuel cell car offers several advantages when compared to a state-of-the-art vapor compression cycle. The first and most important one is the fact that it does not consume mechanical or electrical energy. Its driving force was applied prior at the refueling station in any case and is stored in the high-pressure gaseous state in the onboard pressure tank. Moreover, the system contains no problematic refrigerant and no moving parts.

In the present publication, such an open metal hydride heat pump is considered. The system consists of two reactors filled with the same type of metal hydride reacting reversibly with hydrogen. The relation between equilibrium temperature and equilibrium pressure of the reaction can be represented by a straight line in a Vaṅt Hoff diagram, cf. Fig. 1 (b). Both reactors work in alternating batch mode allowing a quasi-continuous operation at a constant hydrogen flow and a quasi-constant heat flow through the system. The quasi-continuous operation consists of two half cycles, cf. Fig. 1 (a). In the first half cycle reactor 1 is connected with the high-pressure hydrogen inlet side coming from the high-pressure on-board tank. Before entering reactor 1, the inlet pressure from the high-pressure tank (350 or 700 bar) is reduced in a pressure reducer to a constant pressure level in the range of approximately 20–70 bar. This allows the open metal hydride heat pump to work on constant pressure levels until the pressure inside the pressure tank reaches this value which is considered as its discharge end state or the beginning of operation on emergency reserve. The metal hydride inside reactor 1 absorbs hydrogen and releases heat during this exothermic reaction. The temperature where this heat is released depends on the thermodynamic property of the applied metal hydride material, expressed by its equilibrium line in the Van't Hoff diagram in Fig. 1 (b). Simultaneously, during this first half cycle reactor 2 is connected with the low-pressure side and desorbs hydrogen. Due to the Van't Hoff correlation of the metal hydride reaction with hydrogen, the reaction at lower pressure is related to a lower temperature than at the absorption. Hence, heat is taken up during the desorption at a lower temperature than heat is released at the absorption on high pressure. Once the hydrogen outlet flow cannot maintain the required outlet flow, the pressure inside reactor 2 has decreased to the back pressure at the low-pressure outlet. At this point, the reaction is switched between the two reactors again in order to maintain the hydrogen flow to the fuel cell.

The two pressure levels on which such kind of metal hydride system is based are considered as a prerequisite and a compression is not part of the system consideration represented in Fig. 1 (a). Hence this metal hydride heat pump is denoted as an open system. As it releases heat at a higher temperature than it takes it up, it can be either utilized as a heat pump or a refrigeration machine, depending on either the heat or the cold generating side is considered as the useful thermal power output.

The so far illustrated working principle is based on a quasi-continuous operation which is characterized by two effects: thermal losses at the half-cycle switching as well as non-complete conversion. Thermal losses occur since each reactor first has to cool down respectively heat up itself to the temperature level of the next half cycle before usable cold respectively heat can be generated. Consequently, the usable cold and heat is reduced and considered as thermal losses. Non-complete conversion appears especially due to the specific operation of this open system at a constant gas flow. Depending on the applied gas flow the reaction in the reactor can proceed only to a specific degree of conversion before the lower pressure level is reached. Thus, in contrast to other sorption systems where specific half-cycle times can be defined for the process, in the present system, the apparent half-cycle time depends on the applied gas flow.

Both effects – thermal loss and non-complete conversion – strongly influence the performance and the operation behavior at different boundary conditions. To design a system for high power and efficiency, the reactor has to be well-constructed and the metal hydride material properly selected. For this purpose, a model is necessary reflecting the main effects in an appropriate way. For instance, to achieve a high specific power, the reactor has to facilitate good heat transport, which requires heat transport-enhancing structures. These structures, however, increase the overall heat capacity of the reactor, which leads to thermal losses and thus reduces the usable thermal power. This is in contrast to the design of a metal hydride hydrogen storage tank which represents a completely other application of metal hydrides. For a metal hydride hydrogen storage tank, a higher heat transfer directly improves the power in terms of charge and discharge time. In contrast, the open metal hydride heat pump modeled in this work is a thermal energy converter. With its cyclic switches between the two temperature levels, it leads to a more complex optimization task and requires as a basis a simple and fast model which is still sufficiently precise in predicting the specific thermal power and efficiency as the main performance indicators.

For the open metal hydride heat pump system most studies were done experimentally [7,13]. Only a very detailed time and spatial resolved finite element model exists, which is suitable for only one dedicated reactor and only capable of simulating one half cycle [15]. Hence, a more fundamental model approach than the one by Weckerle et. al. [15] is necessary to represent the main effects of its quasi-stationary operation and utilize it for a model-based preliminary design process.

Thus, the aim of this work is the development of a model to assist the systematic design of an open metal hydride heat pump. The model should predict the time average thermal power and efficiency as the two main performance indicators. Moreover, the model should facilitate a fast computation for varying influencing design and material parameters. Applying such a model could help to find an answer to the question of how an optimal reactor should look like in order to achieve a high thermal power with a low mass of the solid reactant under a given set of boundary conditions. Ideally, the model approach is also applicable to other gas–solid reaction systems.

In section 2, the newly developed model with its simplifications, required details and the solver procedure is presented. While in section 3 the model is validated with literature data whereby the operation characteristic of the validation reactor is further analyzed. Finally, in section 4 the model is used as a tool to evaluate the design of the validation reactor itself and its influence on the performance as an example of how the model could be used for designing a new reactor.

2. Model description

Firstly, this section describes how the process of such a quasi-continuous operation can be characterized and the main characteristic properties will be identified to define a lumped system representation. Then the calculation of the reacted fraction as the most crucial characteristic property is explained in the following sub-section. Therefore, the metal hydrides reaction kinetic and one-dimensional modeling of the heat and mass transport for commonly used reactor types are included in the analytical description. Finally, the solver procedure is explained in the last sub-section.

2.1. Fundamentals of quasi-continuous operation and characteristic properties

Due to the quasi-continuous operation principle, the real thermal power profile is not constant over time, even if the hydrogen outlet flow rate is constant. At each half-cycle switch, the reactor has to be heated up or cooled down, to reach the working temperature of the hot or cold side, respectively. This leads to a negative peak in the temporal progress of the power curve at the beginning of a new half cycle followed by an ascending course until a steady-state phase occurs, as shown experimentally in [13]. However, in the present model, the time average of the thermal power and efficiency rather than their periodic time-dependent course are used since the purpose of the model is a fast model for preliminary design and optimization. For a practical integration, the real periodic power profile does not cause any problems and can easily be damped by the heat exchangers in the surrounding fluid loop, as could be shown in simulations in [16]. Thus, a time average thermal power and efficiency are sufficient outcome measures of the model.

Hence, the approach of the present lumped model is based on an energy balance over the half-cycle duration, wherein the cooling down or heating up phase is considered with its time integral heat. In each half cycle the effective usable thermal energy Q_{eff} consequently equals the heat of reaction minus the capacitive heat $Q_{\Delta T}$ from the temperature switch between the hot and cold side, cf. Eq. (1). This balance equation looking simple at first glance is the basis for the subsequent determination of the thermal power and efficiency and is important to keep in mind when looking at the results discussed in the next section.

$$Q_{\mathrm{eff}} = Q_{\mathrm{r}} - Q_{\Delta T} \tag{1}$$

The heat of reaction in Eq. (1) can be expressed by the reacted amount of hydrogen and the reaction enthalpy ΔH_{r}. With the definition of the conversion $\Delta w = \Delta m_{\mathrm{H_2}}/m_{\mathrm{mh}}$ as the reacted mass of hydrogen $\Delta m_{\mathrm{H_2}}$ per half cycle related to the mass of metal hydride m_{mh}, the first summand of Eq. (1) can be formulated as follows:

$$Q_{\mathrm{r}} = m_{\mathrm{H_2}}\frac{\Delta H_{\mathrm{r}}}{M_{\mathrm{H_2}}} = m_{\mathrm{mh}}\Delta w\frac{\Delta H_{\mathrm{r}}}{M_{\mathrm{H_2}}} \tag{2}$$

The heat loss $Q_{\Delta T}$ due to the temperature switching is described by the temperature difference $\Delta T_{\mathrm{lift}} = T_{\mathrm{h}} - T_{\mathrm{c}}$ between hot and cold side, the masses m_{mh} of used metal hydride and applied reactor mass m_{rt} as well as its corresponding specific heat capacities (c_{mh} and c_{rt}):

$$Q_{\Delta T} = (c_{\mathrm{mh}}m_{\mathrm{mh}} + c_{\mathrm{rt}}m_{\mathrm{rt}})\Delta T_{\mathrm{lift}} \tag{3}$$

To determine the average thermal power of this quasi-continuous operation, the usable heat per half cycle is divided by the half-cycle duration Δt_{hc}. This time duration is determined by the reacted amount of hydrogen and the applied hydrogen mass flow $\dot{m}_{\mathrm{H_2}}$ and can also be expressed by the conversion Δw and the used mass of metal hydride:

$$\Delta t_{\mathrm{hc}} = \frac{m_{\mathrm{H_2}}}{\dot{m}_{\mathrm{H_2}}} = \frac{m_{\mathrm{mh}}\Delta w}{\dot{m}_{\mathrm{H_2}}} \tag{4}$$

The hydrogen mass flow is assumed to be constant over time, as a quasi-continuous system is considered.

Since the thermal power of a metal hydride system is dependent on the applied mass of metal hydride inside the reactor, the specific power instead of the absolute power is considered in literature to evaluate the performance of such a system. Therefore, the time-averaged specific thermal power related to the applied metal hydride mass is determined and denoted further just as specific thermal power. It represents the first of the two main performance indicators in this work and is described in Eq. (5) using Eq. (1) up to (4).

$$\frac{\bar{\dot{Q}}}{m_{\mathrm{mh}}} = \frac{1}{m_{\mathrm{mh}}}\frac{Q_{\mathrm{eff}}}{\Delta t_{\mathrm{hc}}} = \frac{\dot{m}_{\mathrm{H_2}}}{m_{\mathrm{mh}}}\left(\frac{\Delta H_{\mathrm{r}}}{M_{\mathrm{H_2}}} - \frac{c_{\mathrm{mh}}(1+k_{\mathrm{C}})}{\Delta w}\Delta T_{\mathrm{lift}}\right) \tag{5}$$

In analogy to the thermal power also the hydrogen mass flow is referred to the applied mass of metal hydride and is further denoted as specific hydrogen flow. The factor k_{C} in Eq. (5) describes the ratio of the heat capacity of the reactor C_{rt} to the heat capacity of the metal hydride C_{mh}. If the mass-specific heat capacities of the reactor and the metal hydride are the same, k_{c} is reduced to the ratio of used reactor mass per mass of metal hydride, which was formerly introduced in the literature as the indicator k for evaluation of a reactor design [14].

$$k_{\mathrm{C}} := \frac{C_{\mathrm{rt}}}{C_{\mathrm{mh}}} = \frac{c_{\mathrm{rt}}m_{\mathrm{rt}}}{c_{\mathrm{mh}}m_{\mathrm{mh}}} \tag{6}$$

Besides the specific thermal power, the second important performance indicator is represented by the so-called cooling efficiency η_{c}, introduced in [13]. It is defined as the usable thermal power considering the capacitive heat losses related to the theoretical thermal power solemnly due to the thermochemical reaction. With Eq. (2) and (5) the cooling efficiency as the second of the two main performance indicators in this work can be formulated according to Eq. (7) and is further denoted just as efficiency.

$$\eta_C = \frac{\bar{\dot{Q}}}{\dot{Q}_{\mathrm{r}}} = 1 - \frac{c_{\mathrm{mh}}(1+k_{\mathrm{C}})\Delta T_{\mathrm{lift}}}{\Delta w\,\frac{\Delta H_{\mathrm{r}}}{M_{\mathrm{H2}}}} \tag{7}$$

In contrast to the formula for the specific thermal power, in this equation, it is noteworthy that the specific hydrogen flow is not a directly influencing variable.

If one would like to use Eq. (5) and Eq. (7) to explicitly calculate the two performance indicators specific thermal power and efficiency, except the reacted fraction Δw all variables in the two equations are either constant for a chosen material ($\Delta H_{\mathrm{r}}, c_{\mathrm{mh}}$), depend on the reactor design (k_{C}) or depend on the chosen operation condition ($\dot{m}_{\mathrm{H_2}}/m_{\mathrm{mh}}$, ΔT_{lift}). These parameters can be in most cases approximated in a simple way. The reacted fraction Δw, however, depends itself on several influencing parameters. It determines how the capacitive heat losses compare to the heat from the reaction and therefore it has a strong

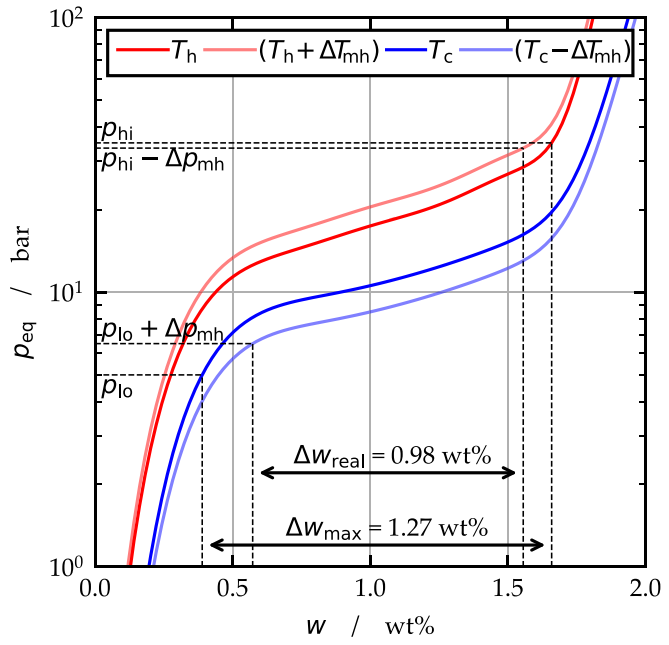

Fig. 2. Reaction conversion in the PCI plot with and without heat and mass transport.

influence on both, the specific thermal power and also the efficiency. So far, for the design of thermal metal hydride applications, the reacted fracted is commonly considered as constant. This is a too-rough simplification and yields improper performance predictions. Thus, the calculation of the reacted fraction Δw is crucial and builds the core of the present model.

First of all, there is a maximum reachable conversion Δw_{max} for a certain material and boundary setting. It can be determined from the metal hydrides pressure-concentration-isotherm (PCI) curves and the boundary conditions T_h, T_c, p_{hi} and p_{lo}, as described in detail in [17]. The intersection of the isotherm referring to T_h with the absorption pressure p_{hi} defines the maximum concentration w_{max} and the intersection of the lower isotherm referring to T_c with the lower desorption pressure p_{lo} defines the minimum concentration w_{min} of hydrogen inside the metal hydride (cf. Fig. 2). The maximum possible reaction conversion Δw_{max} can then be calculated as the difference of the maximum and minimum concentration, $\Delta w_{max} = w_{max} - w_{min}$. This maximum reaction conversion is constant for a given material and given temperature and pressure boundaries of the system.

However, the two states w_{max} and w_{min} represent equilibrium states but during operation they typically will not be reached at the end of each half cycle, in particular when a high specific hydrogen flow is applied. As it can be seen from real metal hydride reactors designed for hydrogen storage application, the actual conversion Δw is strongly dependent on the applied specific hydrogen flow [18–20]. This behavior can be also transferred to a single reactor in this open metal hydride heat pump in each half cycle since it acts like a small and rapidly discharged metal hydride storage tank. Using the condition of a constant specific hydrogen flow $\dot{m}_{H_2}/m_{mh}$, the reached conversion decreases continually with increasing specific hydrogen flow. From that widely reported behavior in literature and the simplified formula Eq. (5), one can see that there must exist an optimal specific hydrogen flow for the highest specific thermal power. This is apparent from the linear factor of $\dot{m}_{H_2}/m_{mh}$ on the one hand and the decreasing Δw in the denominator on the negative term of the second factor on the other hand. It represents an optimal operation point, which appears due to the high reaction dynamic on the one hand and the higher thermal losses on the other side.

In order to describe the actual reacted conversion in comparison to the maximum possible conversion, the utilization factor F can be used

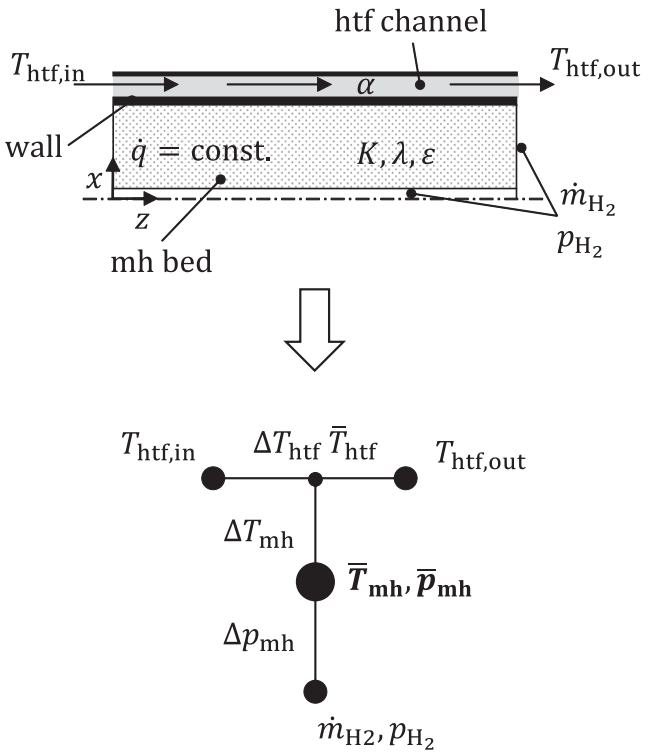

Fig. 3. Geometric reduction to a lumped model representation.

[21]:

$$F = \frac{\Delta w}{\Delta w_{max}} = \frac{w_{end,abs} - w_{end,des}}{w_{max} - w_{min}} \tag{8}$$

With this relation Eq. (5) can be formulated as following:

$$\frac{\bar{Q}}{m_{mh}} = \frac{\dot{m}_{H_2}}{m_{mh}} \left(\frac{\Delta H_r}{M_{H_2}} - \frac{c_{mh}(1+k_C)}{F\,\Delta w_{max}} \Delta T_{lift} \right) \tag{9}$$

In order to use Eq. (9) to predict the specific thermal power and the cooling efficiency, the actual course of the function $F = f(\dot{m}_{H_2}/m_{mh})$ is essential. This function strongly depends on the applied temperature and pressure boundary conditions, the material's equilibrium properties (determined by its PCI curves) and the chosen reactor design, determining the heat and mass transport resistance. Its calculation is crucial for the model and will be presented in the following section.

2.2. Simplified geometry and lumped model equations

This section describes the newly developed methodology to calculate the functional relationship between the actual conversion Δw or its deduced utilization factor F as a functional relationship of the specific hydrogen flow considering pressure and temperature boundary conditions, material and reactor properties. As mentioned before, in existent analytical models the conversion is assumed to be constant, in particular either the material's maximum hydrogen storage capacity $w_{max,total}$, the maximum end concentration w_{max} or the maximum reachable conversion $\Delta w_{max} = w_{max} - w_{min}$. Such an assumption does not lead to reliable values for the power of the system and the efficiency at this rated power, nor does it show how both vary with different applied hydrogen flows.

The main assumptions used in the present model can be summarized as follows:

- Lumped metal hydride mass (cf. Fig. 3)
- Steady-state
- Homogeneous reaction

- One-dimensional heat and mass flow
- Constant porosity ε, thermal conductivity λ, specific heat capacity c, density ρ, viscosity η, and permeability κ
- Constant reaction enthalpy $\Delta H_{r,abs}, \Delta H_{r,des}$
- Constant outer heat transfer coefficient α
- No contact resistance from metal hydride bed to reactor wall
- Neglectable temperature difference over wall thickness
- Low amount of stored hydrogen in pores compared to hydrogen inside the metal hydride

The basis for this calculation of the reached conversion provides the kinetic equation, which describes the reaction rate. Since a low amount of stored hydrogen in the pores compared to hydrogen inside the metal hydride is assumed, the hydrogen inside the pores is neglected. In that case, the reaction rate $\mathrm{d}w/\mathrm{d}t$ equals the specific hydrogen flow $\dot{m}_{H_2}/m_{mh} = \mathrm{d}w/\mathrm{d}t$. As for most thermochemical gas–solid reaction systems, the conversion rate for this reaction depends on the current hydrogen concentration w inside the metal hydride. Specifically, for the intermetallic metal hydride used in the experiments to validate the model [17], a first-order kinetic equation can be utilized in the form of Eq. (10) and (11) [22].

$$\text{Desorption}: \quad \frac{\dot{m}_{H_2}}{m_{mh}} = \frac{\mathrm{d}w}{\mathrm{d}t} = \dot{w} = k_T(T)\frac{p - p_{eq}}{p_{eq}}w \tag{10}$$

$$\text{Absorption}: \quad \dot{w} = k_T(T)\frac{p - p_{eq}}{p_{eq}}(w_{max,total} - w) \tag{11}$$

In Eq. (11) the variable $w_{max,total}$ denotes the maximum hydrogen capacity of the applied metal hydride material. The kinetic coefficient $k_T(T)$ can be described via an Arrhenius term, cf. Eq. (12), where K_0 is the kinetic constant, E_a is an activation energy and k_B is the universal Boltzmann constant [22].

$$k_T(T) = -K_0 \exp\left(-\frac{E_a}{k_B T}\right) \tag{12}$$

Since a lumped model is considered, Eq. (10) and (11) for the absorption and desorption respectively can be applied to the lumped metal hydride mass point. These differential Equations do not have to be integrated, since temporal courses are not relevant. The end concentration $w = w_{end}$ of each half cycle can be calculated directly from these equations for a given specific hydrogen flow.

For an ideal system at isothermal and isobaric conditions with an ideal material showing no plateau slope in the PCI curve ($p_{eq} = \text{const.} \neq f(w)$), the course of the function $F = f(\dot{m}_{H_2}/m_{mh})$ shows a linear shape. It is then determined solely by a constant applied distance from the equilibrium, by means of the applied boundary pressure and the materials equilibrium pressure at the applied boundary temperature, and the kinetic constant at the applied boundary temperature. This describes an ideal metal hydride system, which is only limited by its intrinsic reaction kinetics.

However, further modeling is necessary in order to consider the two important non-ideal effects. The first one is that indeed all practical metal hydrides show a more or less steep plateau slope, which leads to a non-constant distance to the equilibrium during reaction and therefore a non-constant driving force of the pressure term in Eq. (10) and (11), respectively. Thus, a concentration-dependent equilibrium pressure in the form of a real PCI for the applied metal hydride has to be considered.

The second is that non-ideal heat and mass transport inside the reactor leads to non-isothermal and non-isobaric conditions inside the real reactor. Hence the pressure p and the temperature T in Eq. (10) and (11) are not equal to the pressure and temperature boundary conditions applied. A suitable implementation of heat and mass transport is of high importance since most really constructed reactors are limited in their reaction rate through either heat or mass transport.

2.2.1. Implementation of a real PCI behavior

The first of the two mentioned important steps is the modeling of the equilibrium behavior of a real metal hydride as a function $f(T,p,w)$. In the initial implementation of the present model and for the validation presented in the following section a semi-physical approach is used like the one in [15,20]. Therein the temperature dependency is modeled using a van't Hoff equation with the physical properties of the reaction enthalpy ΔH_r and the reaction entropy ΔS_r. The concentration dependency in contrast is modelled by a mathematical approach with a higher-order polynomial. In order to consider the hysteresis between absorption and desorption PCI curve, each of them is described with a separate set of ΔH_r, ΔS_r and polynomial parameters. Thus, the constant equilibrium pressure p_{eq} in Eq. (10) and (11) is replaced by a more precise expression for the equilibrium pressure in the form of $p_{eq} = f(T, w)$.

2.2.2. Geometric reduction to the lumped model

For the second important step of the modeling, the implementation of heat and mass transport resistances, a geometric reduction is necessary.

The general requirement for sufficient heat transfer in the reactor leads for most realized reactors to small heat transfer distances and a high heat exchange surface even for hydrogen storage applications. There are several reactor types reported in the literature, which are often variations of a tube reactor or a plate reactor [15,23]. Therefore, it is assumed that a basic geometry as depicted in Fig. 3 simplistically represents a majority of common reactor designs. This basic geometry represents the cross-section of either a planar or rotationally symmetric structure. The metal hydride bed is confined by a reactor wall and a channel with a heat transfer fluid. In the case of a planar symmetric structure, several of these plane layers are stacked together to form a plate reactor. Then the upper wall of the fluid channel is not an additional wall as for a rotationally symmetric tube reactor but consists of the reactor wall of the next layer. In the case of a tube reactor, the wall of the fluid channel can be thinner than the reactor wall since it does not face the stress from the inner hydrogen pressure. The hydrogen inlet and outlet can either be arranged at the side or orthogonal to the bed length direction z through a center hole or feed layer. For this basic geometry an upscaled reactor could be realized as tube bundle. Based on this geometry a geometric reduction to a zero-dimensional lumped model (cf. Fig. 3) is conducted in order to properly calculate this mean temperature and the temperature difference. The lumped elements represent the fluid inlet and outlet state as well as a mean fluid state, the mean metal hydride state and the hydrogen feed state. The heat and mass transport phenomena will be included by mean pressure and temperature differences between these lumped elements. In the following, the implementation of the heat transfer resistance and then the implementation of the mass transfer are described separately.

2.2.3. Implementation of the heat transfer resistance

To consider the heat transfer resistance, a mean temperature difference between the mean fluid temperature $\overline{T}_{htf}$ and the mean metal hydride temperature $\overline{T}_{mh}$ is used, denoted as $\Delta\overline{T}_{mh} = \overline{T}_{htf} - \overline{T}_{mh}$, cf. Fig. 3. Accordingly, the constant temperature T in Eq. (10) and (11) is replaced by $\overline{T}_{mh} = \overline{T}_{htf} + \Delta\overline{T}_{mh}$. Due to the above-mentioned motivation to reduce the heat transport limitation, the bed thickness mostly is small compared to the bed length of the reactor. In this case, the heat transfer in the cross-section direction from the metal hydride to the surrounded heat transfer fluid represents the dominating heat transfer process. Since a small bed thickness and a high reaction rate $\mathrm{d}w/\mathrm{d}t = \dot{m}_{H_2}/m_{mh}$ are considered, the heat source (absorption) respectively heat sink (desorption) are assumed to be homogeneous over the bed thickness. A similar model approach is presented in [24] and was validated successfully. Moreover, in the scope of the model, the fluid flow is set sufficiently high that the temperature difference between fluid inlet and

outlet is small compared to the temperature difference over the bed thickness. In this case, also the reaction in bed length (axial) direction can be considered to be homogeneous. Thus, a steady-state one-dimensional temperature profile in bed thickness direction for a homogenous and constant heat source can be deduced analytically. The mean metal hydride temperature difference $\Delta\overline{T}_{\mathrm{mh}}$ is then defined as the integral mean value of the temperature profile over the bed depth d_{mh} and leads to Eq. (13) for a plane geometry.

$$\Delta\overline{T}_{\mathrm{mh}} = \frac{1}{d_{\mathrm{mh}}}\int_0^{d_{\mathrm{mh}}} T(x)\mathrm{d}x = \frac{\dot{q}_{\mathrm{vol}}}{2\lambda} d_{\mathrm{mh}}^2 \left(\frac{2}{\mathrm{Bi}} + \frac{2}{3}\right) \tag{13}$$

To determine the volumetric heat source $\dot{q}$ of the reaction from the specific hydrogen flow, the porosity ε and metal hydride density ρ_{mh} have to be considered according to:

$$\dot{q}_{\mathrm{vol}} = \frac{\dot{m}_{\mathrm{H_2}}}{m_{\mathrm{mh}}} \frac{\Delta H_{\mathrm{r}}}{M_{\mathrm{H_2}}} (1-\varepsilon)\rho_{\mathrm{mh}} \tag{14}$$

A mean heat transfer coefficient α over the reactor length is used. Together with the thermal conductivity λ and bed depth d_{mh} they form the Biot-number $\mathrm{Bi} = \alpha d_{\mathrm{mh}}/\lambda$ in Eq. (13). The temperature gradient over the reactor wall is neglected. This is reasonable, as usually the reactor wall is much thinner than the metal hydride bed thickness and also has a much higher thermal conductivity. Additionally, the thermal conduct resistance from the porous metal hydride bed to the inner wall side is neglected as a further model simplification. For a rotationally symmetric geometry, the mean temperature difference can be calculated in the same way as it can be seen in the Appendix.

2.2.4. Implementation of the mass transfer resistance

Similarly to the heat transfer resistance also for the mass transfer resistance, a mean pressure difference $\Delta\overline{p}_{\mathrm{mh}} = p_{\mathrm{H_2}} - \overline{p}_{\mathrm{mh}}$ is used to describe the difference between the applied boundary pressure in the feed pipe $p_{\mathrm{H_2}}$ to the mean pressure $\overline{p}_{\mathrm{mh}}$ inside the metal hydride bed, cf. Fig. 3. Accordingly, in Eq. (10) and (11) the constant boundary pressure p is replaced by $\left(p_{\mathrm{H_2}} + \Delta\overline{p}_{\mathrm{mh}}\right)$. In analogy to the heat transport modeling, only a mean pressure $\overline{p}_{\mathrm{mh}}$ inside the metal hydride bed is considered as the integral mean value of the pressure profile. The pressure profile is also calculated with the assumption of a homogeneous reaction. Since the reaction couples heat and mass changes, the homogeneous reaction leads not only to a homogeneous heat source or sink but also to a homogeneous hydrogen mass source or sink. The pressure profile can be calculated with Darcy's law and the equation of state for an ideal gas to consider the pressure-dependent gas density. This leads to the following differential equation:

$$\frac{\mathrm{d}p}{\mathrm{d}x} = \frac{\eta}{\kappa} \frac{\dot{m}_{\mathrm{H_2}}}{m_{\mathrm{mh}}} \frac{RT}{M_{\mathrm{H_2}}} \frac{1}{p} (1-\varepsilon)\rho_{\mathrm{mh}}(d_{\mathrm{mh}} - x) \tag{15}$$

It contains the dynamic viscosity η of the hydrogen gas and the permeability κ of the metal hydride bed. The differential equations can be can be solved for the pressure profile $p(x)$ by separating the variables. The mean pressure difference is defined in analogy to the temperature as the integral mean value of the pressure profile over the bed depth d_{mh} and arises to Eq. (16) for a planar geometry:

$$\begin{aligned}\Delta\overline{p}_{\mathrm{mh}} &= \frac{1}{d_{\mathrm{mh}}}\int_0^{d_{\mathrm{mh}}} p(x)\mathrm{d}x \\ &= \frac{1}{d_{\mathrm{mh}}}\int_0^{d_{\mathrm{mh}}} \left\{ 2\frac{\eta}{\kappa}\frac{RT}{M_{\mathrm{H_2}}}\frac{\dot{m}_{\mathrm{H_2}}}{m_{\mathrm{mh}}}(1-\varepsilon)\rho_{\mathrm{mh}}\left(d_{\mathrm{mh}}x - \frac{x^2}{2}\right) + {p_{\mathrm{H_2}}}^2 \right\}^{\frac{1}{2}} \mathrm{d}x - p_{\mathrm{H_2}}\end{aligned} \tag{16}$$

Since the function for the pressure profile has a very elongated analytical solution for its integral, the mean pressure is solved numerically in the present model implementation. If the hydrogen gas feed is not provided from the bottom in the bed thickness direction, but from the side through the whole length of the bed (cf. Fig. 3), d_{mh} can simply be replaced by the reactor length and the variable x by the variable z. The mean pressure difference of a rotationally symmetric geometry is calculated in analogy to it and provided in the Appendix.

2.2.5. Heat transfer fluid temperature

The temperature profile of the heat transfer fluid in its channel (cf. Fig. 3) is not spatially resolved in the channel height direction (in case of a planar geometry) respectively radial direction (in case of a tube geometry), instead a bulk temperature T_{htf} is considered. The temperature profile in the channel length direction, respectively in the axial direction, however, is considered as $T_{\mathrm{htf}} = \mathrm{f}(z)$. It can be derived from the energy balance between the heat source or sink of the metal hydride bed and the fluid flow, cf. Eq. (16). Due to the assumption of a homogeneous reaction in the metal hydride bed, the axial fluid temperature profile is linear. Therefore, a mean fluid temperature $\overline{T}_{\mathrm{htf}} = (T_{\mathrm{htf,in}} + T_{\mathrm{htf,out}})/2$ is defined as the arithmetic average of the input and output fluid temperature. The fluid input temperature $T_{\mathrm{htf,in}}$ serves as an input variable for the model. The output temperature $T_{\mathrm{htf,out}}$ is either calculated with a given metal hydride mass specific fluid flow $\dot{V}_{\mathrm{htf}}/m_{\mathrm{mh}}$ and the specific hydrogen flow according to Eq. (17) or has a given constant difference ΔT_{htf} to the input temperature.

$$\frac{\dot{V}_{\mathrm{htf}}}{m_{\mathrm{mh}}}\rho_{\mathrm{htf}}c_{\mathrm{htf}}\left(T_{\mathrm{htf,out}} - T_{\mathrm{htf,in}}\right) = \frac{\dot{m}_{\mathrm{H_2}}}{m_{\mathrm{mh}}}\frac{\Delta H_{\mathrm{r}}}{M_{\mathrm{H_2}}}(1-\varepsilon)\rho_{\mathrm{mh}} \tag{17}$$

In the first case, the specific fluid flow is given as an input variable, whereas the output temperature is calculated. In the latter case, the output temperature is given as the input variable, whereas the specific fluid flow is calculated. Both calculation types can be selected individually for the absorption half cycle (hot side fluid loop) and desorption half cycle (cold side fluid loop).

2.3. Solving procedure

In the previous subsections, all necessary equations for the present lumped model are presented. They are consecutively connected and evaluated in the following presented solving procedure to first determine the crucial conversion Δw (and the derived utilization factor F) and then the two main performance indicators the specific thermal power and efficiency. Therefore the kinetic Eq. (10) for the desorption can be extended to Eq. (18) using the equilibrium pressure expressed by a real PCI in the form $p_{\mathrm{eq}}(T, w)$ and the heat and mass transport resistances expressed by the mean temperature and mean pressure differences $\Delta\overline{T}_{\mathrm{mh}}$ and $\Delta\overline{p}_{\mathrm{mh}}$. In analogy to this, the kinetic equation (11) for the absorption can be extended in the same way in order to calculate the end concentration $w_{\mathrm{end,abs}}$ for the absorption, respectively.

$$\frac{\dot{m}_{\mathrm{H_2}}}{m_{\mathrm{mh}}} = \dot{w} = k_{\mathrm{T}}\left(\overline{T}_{\mathrm{htf}} + \Delta\overline{T}_{\mathrm{mh}}(\dot{w})\right)\left(\frac{p + \Delta\overline{p}_{\mathrm{mh}}(\dot{w})}{p_{\mathrm{eq}}\left(\overline{T}_{\mathrm{htf}} + \Delta\overline{T}_{\mathrm{mh}}(\dot{w}), w\right)} - 1\right) w \tag{18}$$

In order to determine a functional dependency between the reaction rate $\dot{w}$ and the desorption end concentration $w_{\mathrm{end,des}}$ in the form of $w = \mathrm{f}(\dot{w})$ or $\dot{w} = \mathrm{f}(w)$, Eq. (18) has to be solved. Since $\Delta\overline{p}_{\mathrm{mh}} = \mathrm{f}(\dot{w})$ and $p_{\mathrm{eq}} = \mathrm{f}(w)$ as parts of this equation are not solvable analytically for their function argument, the equation has to be solved numerically. In the present implementation, this is done for the form of $w = \mathrm{f}(\dot{w})$.

The overall calculation procedure of the present model consists of the following subsequent steps:

1. The maximum and the minimum concentrations w_{max} and w_{min} are calculated from the PCI representation with the boundary temperature and pressure conditions T_{h}, p_{hi} and T_{c}, p_{lo} respectively.
2. A specific hydrogen flow is chosen.

Table 1
Parameters used for the validation.

Parameter	Symbol	Value
Metal hydride material properties		
absorption reaction enthalpy, J mol^{-1}	$\Delta H_{r,abs}$	17.8*10^{3}
desorption reaction enthalpy, J mol^{-1}	$\Delta H_{r,des}$	21.9*10^{3}
polynomial parameters of the PCI representation according to [15]		
maximum total storage capacity, wt.-%	$w_{max,total}$	1.9
absorption end concentration, wt.-%	$w_{abs,end}$	1.35
kinetic constant, s^{-1}	K_0	190,400
activation energy, J	E_a	5.083*10^{-20}
density of mh, kg m^{-3}	ρ_{mh}	6300
mass specific heat capacity of reactor material, J kg^{-1} K^{-1}	c_{mh}	500
Reactor properties		
mass specific heat capacity of reactor material, J kg^{-1} K^{-1}	c_{rt}	500
fraction of reactor to metal hydride heat capacity, -	k_C	3.16
depth for heat transport, m	d_{ht}	0.88*10^{-3}
depth for mass transport, m	d_{mt}	0.276
heat transfer coefficient, W m^{-2} K^{-1}	α	700
porosity, -	ε	0.67
permeability, m^{-2}	κ	1.75*10^{-13}
effective thermal conductivity, W m^{-1} K^{-1}	λ	1
Boundary conditions		
hot side (absorption) temperature, K	T_h	303.15
cold side (desorption) temperature, K	T_c	293.15
high (absorption) pressure, Pa	p_{hi}	35*10^{5}
low (desorption) pressure, Pa	p_{lo}	5*10^{5}
Operation conditions		
mh mass specific volume flow of htf, m^3 s^{-1}	$\dot{V}_{htf}/m_{mh}$	4.55*10^{-5}
Hydrogen and htf properties		
dynamic viscosity of hydrogen, Pa s^{-1}	η	9.05*10^{-6}*(T / 293) $^{0.68}$
density of htf, kg m^{-3}	ρ_{htf}	1082
mass specific heat capacity of the htf, J kg^{-1} K^{-1}	c_{htf}	3260

3. The mean temperature and mean pressure differences $\Delta\overline{T}_{mh}$ and $\Delta\overline{p}_{mh}$ and the mean fluid temperature $\overline{T}_{htf}$ for the desorption process are calculated by means of Eq. (13), (16) and (17).
4. Eq. (18) is solved numerically for the concentration w, which gives the reached end concentration $w_{end,des}$ during the desorption half cycle.
5. Step 3 and 4 are repeated for the absorption process respectively or a given absorption end concentration $w_{end,abs}$ is used.
6. Die achieved conversion $\Delta w = w_{end,abs} - w_{end,des}$ and the deduced utilization factor F are calculated according to Eq. (8).
7. By Eq. (5) and (7) the capacitive heat losses are considered to finally calculate the average specific thermal power $\overline{\dot{Q}}/m_{mh}$ and efficiency η_c, respectively.

In the context of the quasi-continuous operation consisting of subsequent absorption and desorption half cycles, there is a noteworthy effect apparent. If the calculated end concentration of the desorption half cycle reaches the minimum equilibrium concentration ($w_{end,abs} = w_{min}$), the desorption is not limiting the performance of the system at this operation point (the chosen specific hydrogen flow). The more the desorption end concentration is greater than the minimum concentration, the more the desorption limits the power and efficiency of the system at this operation point. The same relation is applicable for the absorption. In the present implementation of the model, it is optionally possible to set a certain constant absorption end concentration $w_{end,abs}$. In this case, step 5 in the above-mentioned procedure is left out. The absorption is then assumed to be not limiting. This option is useful to model the characteristic of an experimentally examined material, which does not reach its full capacity regarding its PCI curve due to an incomplete activation process. It is used for the presented validation results in the section below.

3. Model validation and discussion of operation characteristic

In this section, the proposed model is successfully validated with experimental data from our previous work. The validation was conducted for a fixed reactor over a wide range of operation and boundary conditions. By use of the validated model, the experimental results can be further analyzed and its characteristics can be explained. A major focus is on the effect of the different applied specific hydrogen flows on the two performance indicators the specific thermal power and the

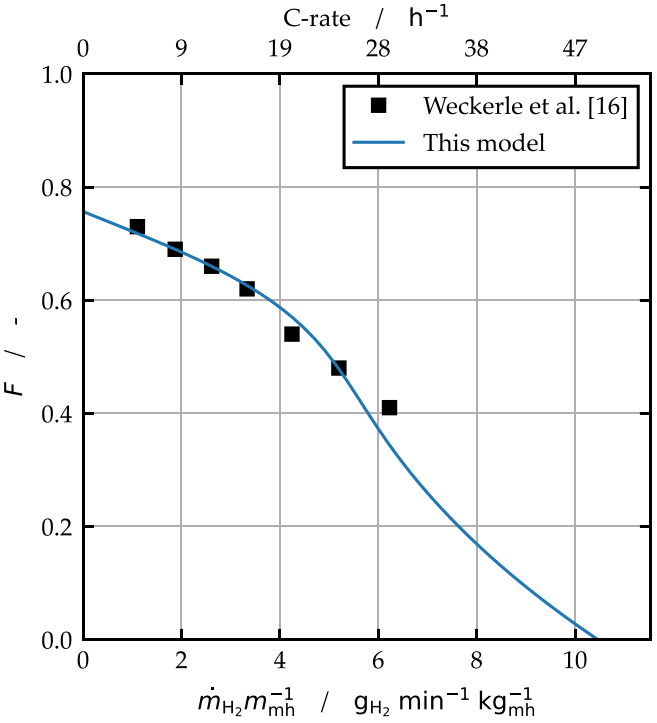

Fig. 4. Utilization factor versus specific hydrogen flow.

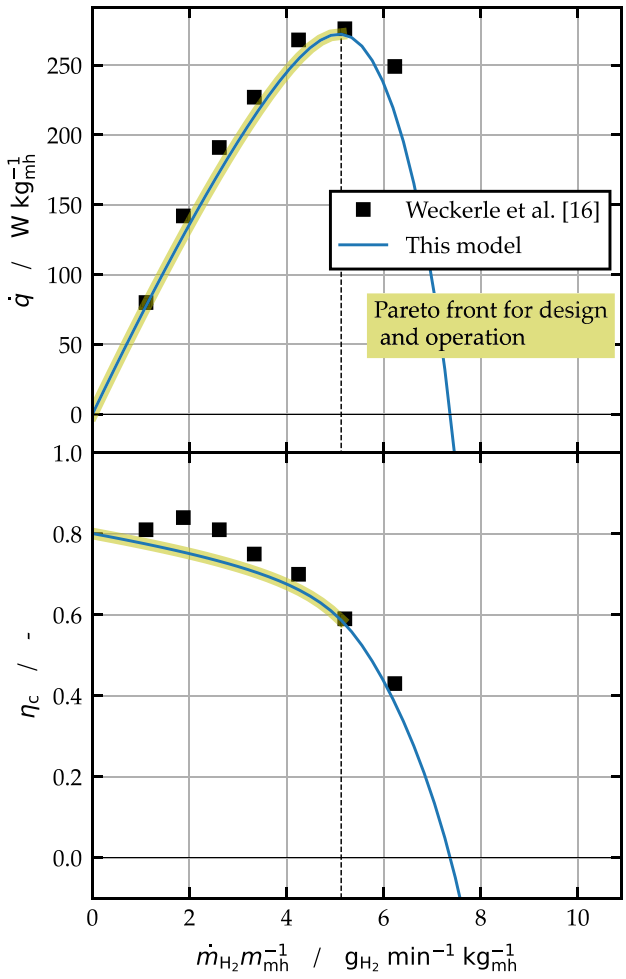

Fig. 5. Operation characteristic for power and efficiency.

efficiency. The observed behavior is denoted herein as operation characteristic and its consequences for the operation as well as for proper sizing for an application are described in this section.

3.1. Details on the validation experiment

The experimental data from [17] are used to validate the present model. In this publication, the two alternating working metal hydride reactors operate in the way of a fixed hydrogen outlet flow with a fuel cell arranged downstream which represents a real quasi-continuous operation. Its experimental setup is shortly summarized in the following. In each reactor, approximately 1,5 kg of the intermetallic semi-binary AB2 type metal hydride "Hydralloy C2" was applied, which is a room-temperature metal hydride based on TiMn1.5. Its PCIs are reported and modelled with a semi-physical polynomial approach in [15]. The reactor is a plate reactor based on a conventional plate heat exchanger with a small bed depth of 0.88 mm on average and a length of 279 mm. The heat transfer coefficient α for this kind of heat exchanger has been calculated with an appropriate Nusselt correlation [25] to be 700 W m^{-2} K^{-1}. The metal hydride is not compacted. Instead, the bed consists of loose powder. Its average porosity ε was measured gravimetrically in the referred experiment. In contrast, the effective thermal conductivity λ and also the permeability κ were not measured there. The thermal conductivity for the validation is taken from the literature, where it does not vary over an order of magnitude. A commonly reported value for a bulk powder is 1 W m^{-1} K^{-1}. Together with the bed depth and the heat transfer coefficient one can deduce a Biot number $\mathrm{Bi} = \alpha d_{ht}/\lambda = 0.62$. However, the permeability is the greatest uncertainty. The reported values in the literature vary in a wide range from approximately 4.5*10^{-15} m^2 to 1.2*10^{-11} m^2 [26,27]. Therefore, within this range, the permeability is used as the fitting parameter. It has been defined as 1.75*10^{-13} m^2 which lies in the order of magnitude of the carefully measured value in [28]. As temperature boundary conditions the hot side temperature for the absorption half cycle is set to 30 °C and the cold side temperature for the desorption half cycle is set to 20 °C, respectively. As pressure boundary conditions the high pressure on the input side is set to 35 bar and the low pressure on the output side is set to 5 bar, respectively. All applied parameters are summarized in Table 1.

3.2. Operation characteristic

As explained in the previous section, the knowledge of the reached conversion Δw or of the deduced variable, the utilization factor F, is essential to use Eq. (5) and (7) to calculate the specific thermal power and the efficiency, respectively. Accordingly, in Fig. 4 the utilization factor F is plotted against the specific hydrogen flow for the experimental data and also for the model results. The utilization factor has a range from zero to one. The value zero represents no conversion and the value one represents that the whole theoretically possible conversion is reached determined by the pressure and temperature boundaries (cf. Fig. 2).

Fig. 4 shows that as the specific hydrogen flow increases, the curve for the utilization factor decreases monotonically. The model curve is in good agreement with the data points from the experiment, showing that the model is able to describe the course of the utilization factor. In contrast to what could be expected, the experimental data show that an extrapolation obviously would not reach the value of $F = 1$ with vanishing specific hydrogen flow. One explanation is that the material in the experiment was not fully activated and did not reach its full capacity. Thus, the end concentration was set as a second fitting parameter besides the permeability. As a result, the end concentration was found to be 1.35 wt% and thus smaller than the one that can be deduced from its PCI curve. The other extremum is the point where the curve of the utilization factor reaches zero. It refers to the maximum achievable specific hydrogen flow. However, at this point no actual conversion is realized and therefore no heat is generated or taken up. Concurrently this point is not relevant for design.

As a secondary x-axis, the discharge rate is plotted. It shows an analogy to electrochemical storages where this discharge rate is denoted as C-rate with the unit 1/h. Blinov et al. [20] first introduced this analogy for metal hydride hydrogen storage systems. It can be interpreted as the reciprocal time duration until the storage is fully discharged. Since the discharge end state expressed by the utilization factor decreases with increasing discharge rate, the reciprocal discharge duration for full discharging shown on the x-axis is a theoretical value. It must not be confused with the real discharge time, which is equal to the real half-cycle time, that will occur during operation.

Fig. 4 just shows an important intermediate result, which is nevertheless important to understand the further results. The actual objective of the model, the calculation of the two performance indicators the specific thermal power and the efficiency, is shown in Fig. 5 against the specific hydrogen flow in comparison with the experimental data.

The curve shows an almost linear course with increasing specific hydrogen flow until a maximum occurs. This follows a rapid decrease with a higher gradient than the rise of the curve. The model fits the experimental quite well including the maximum. The highest deviation between the calculated specific thermal power and the experimentally obtained value is 13.4 % occurring at the highest measured specific mass flow. The maximum power, however, is predicted with a deviation of 1.6 % which is in measurement uncertainty of 7.1 – 7.4 %. For the cooling efficiency, the highest deviation between model and experiment is calculated to be 11.1 %. For the further declining course of the curve no additional experimental data points were available.

The linear raising is obvious from Eq. (5). The point where the

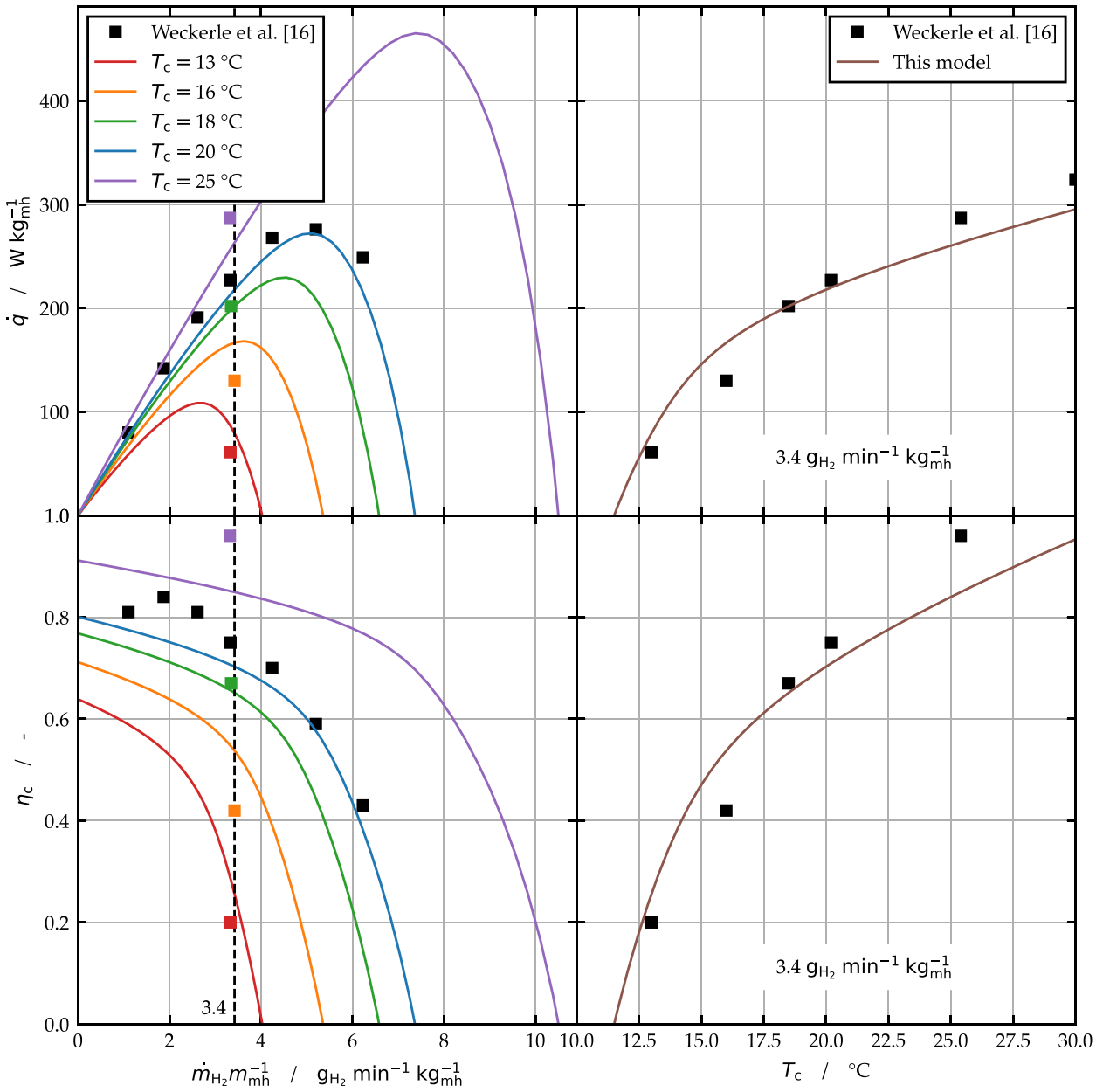

Fig. 6. Influence of different cold side temperatures on specific thermal power and efficiency.

maximum emerges is the point where the declining conversion or utilization factor becomes relevant for the energy balance. The model curve also shows that negative values of pumped heat can occur with a specific hydrogen flow above 7.4 g_{H2} min^{-1} kg_{mh}^{-1} and still lead to some conversion (e.g. $F = 0.22$ for $\dot{q} = 0$, cf. Fig. 4). However, in this case the, conversion has such a small value that the negative term in Eq. (5) becomes larger than the positive term. It implies that the capacitive heat losses are larger than the heat of reaction for these high specific flows. Such a maximum in the specific thermal power for an optimal specific hydrogen flow is also apparent for compressor-driven system as described in [29], where instead of the specific hydrogen flow the real half-cycle time was used.

The cooling efficiency ranges from negative values to one. The value one implies that the whole heat of reaction is pumped from the cold side to the hot side. Fig. 5 shows, that the efficiency decreases monotonically with increasing specific hydrogen flow. At the flow value where the maximum for the thermal power appears, the gradient becomes significantly higher. Moreover, the figure shows that the efficiency of one is not reached with vanishing specific hydrogen flow. This is explained by the utilization factor, which does not become 1 for a vanishing hydrogen flow, as described above.

This subsection showed that the model is capable of describing the two performance indicators the specific thermal power and the efficiency very accurately in the range of different specific hydrogen flows and explains the observed characteristics of the quasi-continuous operation with the help of the decreasing utilization factor. In the following, the consequences of this characteristic for operation and design are discussed. Then in the last subsection, the validation is extended to further variation also on the temperature boundary conditions.

3.3. *Consequences for operation and sizing*

From the fact that the curve of the specific thermal power over the specific hydrogen flow shows a maximum, consequences for operation and sizing can be drawn. For the operation, one can deduce a strategy knowing the characteristic curve in Fig. 5 of a certain system. In this

strategy hydrogen, is bypassed if during operation a hydrogen flow occurs in the region of the declining curve. This prevents the system from reducing its thermal power output due to dominating thermal losses.

Another consequence is the assistance of the characteristic curve in Fig. 5 for a proper sizing of the system. Here two sizing cases have to be distinguished. In the first sizing case, a target value for the absolute thermal power is specified. Then the system could be sized to the optimum of the characteristic curve. This would provide the lowest necessary mass of metal hydride and therefore the smallest system. As an alternative sizing, one could increase the applied mass of metal hydride. Then a higher cooling efficiency can be achieved since this shifts the operations point to a lower specific hydrogen flow, cf. Fig. 5. A higher cooling efficiency in that case means that a lower absolute hydrogen flow is necessary. Moreover, the system is then not sized 'to the edge'. It implies that if a system is sized for such an operation point, it is capable of providing a higher absolute thermal power if the hydrogen flow increases over the value as used as the typical flow value. In the first sizing option, which would yield the smallest system, the thermal power output would decrease or remain constant, if the discussed bypass is implemented. The second sizing option would enable a more flexible operation but with the drawback of a higher applied mass of metal hydride and therefore a bigger system for the typical operation point.

In the second sizing case, an available hydrogen flow is given. In this case, the mass of metal hydride which gives the best power density (specific thermal power) can be determined from this characteristic curve. However, this is not the sizing which gives the highest absolute thermal power output. Since the cooling efficiency increases with decreasing specific hydrogen flow, a sizing with a higher mass of metal hydride would also lead to a higher efficiency and therefore to a higher absolute thermal power output, but with the drawback of a bigger system.

According to these two sizing cases, it can be concluded that a Pareto front can be drawn in the plots for the thermal power and cooling efficiency. For the thermal power, the Pareto front is located on the complete ascending part of the curve until the maximum point, shown in Fig. 5. For the cooling efficiency it is located on the left part of the curve ending at that specific hydrogen flow, where the maximum thermal power is reached. Specifically for the curve of the validation experiment, this means that every specific hydrogen flow up to 5.1 g_{H2} min^{-1} kg^{-1}_{mh} is a valid design point. In this range, it is not possible to increase the thermal power without reducing the cooling efficiency. In contrast, for higher specific flow rates than 5.1 g_{H2} min^{-1} kg^{-1}_{mh}, there are design points where both, the thermal power and also the efficiency can be increased. That is why design points greater than this specific value are excluded from the marked Pareto front.

3.4. Effect of different boundary conditions

In the publication presenting the validation data [17], not only different specific hydrogen flows were applied, but also different cold side and hot side temperatures. Thus, the model can be validated in a range of different temperatures as boundary conditions. The validation and discussion of different cold side (desorption) temperatures are presented in the following. In Fig. 6 the specific thermal power and cooling efficiency are plotted in the same way as in Fig. 5 over the specific hydrogen flow. The model shows a characteristic curve for each cold side temperature. In the experiments, the same specific hydrogen flow was applied for each cold side temperature. Thus, just one data point for each temperature is available to validate the characteristic curve predicted by the model. Nevertheless, it shows a good agreement with the experimental data. The right side of Fig. 6, shows this agreement more distinctly where the thermal power and cooling efficiency are plotted against the cold side temperature for the constant specific hydrogen flow of 3.4 g_{H2} min^{-1} kg^{-1}_{mh} used in the experiment.

Fig. 6 indicates that with lower cold side temperatures the characteristic curves for the specific thermal power reveal a lower maximum.

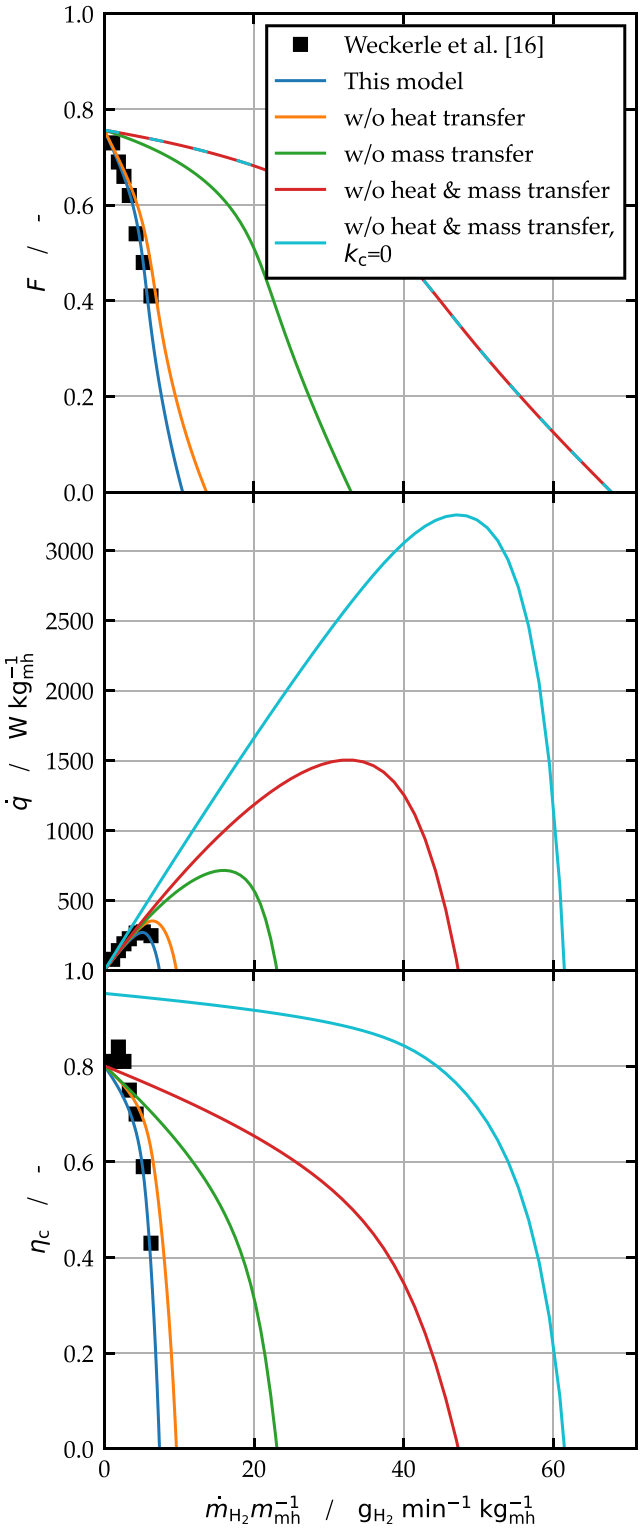

Fig. 7. Influence of reactor properties on the system performance.

The gradient at the beginning is very similar for all of the characteristic curves. But the lower the cold side temperature, the earlier the curve deviates from this common gradient at the beginning and flattens toward the maximal turning point. Accordingly, the value of the specific hydrogen flow on the x-axis for the maximum specific thermal power is shifted to lower values. This leads to the fact that for the same system, the applied hydrogen flow in the experiment lies either left, right or close to the maximum of the characteristic curve, depending on the

applied cold side temperature. For example, for the cold side temperature of 25 °C the hydrogen flow is on the left-hand side of the peak of the characteristic curve implying that an increased hydrogen flow would also increase the thermal power significantly. In contrast, at a cold side temperature of 16 °C the applied hydrogen flow is almost exactly the flow that corresponds to the maximum thermal power output. Further increasing the hydrogen flow would quickly decrease the thermal power. Furthermore, at a cold side temperature of 13 °C the applied hydrogen flow is beyond the optimal value. Consequently, a decreased flow would increase the thermal output.

The first and obvious reason for a lower possible maximal thermal power at colder desorption temperatures is the higher temperature difference for the half-cycle switching, cf. Eq. (5). The second reason is the smaller distance to the equilibrium at the desorption side. As Fig. 2 shows, a lower temperature leads in the PCI diagram to a lower equilibrium pressure, whereas the desorption end pressure is kept the same. Consequently, the driving force of the reaction decreases, cf. Eq. (10) and Eq. (11). For lower cold side temperatures, this leads to a faster decreasing utilization factor on increasing specific hydrogen flows.

Next to the specific thermal power, the curves for the cooling efficiency are lower for lower desorption temperatures. As the hot side temperature is fixed, a lower cold side temperature results in a higher temperature difference between the hot and cold side. Hence the capacitive heat losses are increasing and the cooling efficiency decreases according to Eq. (7). This is also the reason why for a hydrogen flow towards zero the curves do not converge. Although the utilization factor tends to have similar values for small hydrogen flows, the different temperature differences still remain the same. This leads to the fact that each of the curves has a different intersection with the y-axis in Fig. 6.

This sub-section showed that the model is also valid when the cold side temperature as a boundary condition is set on different values. The analog validation on the hot side (absorption) temperatures could also be conducted successfully and is given in the Appendix. As a key finding the model curves show that the peak in the specific thermal power is shifted to other optimal specific hydrogen flows if the cold side temperature is set on different values.

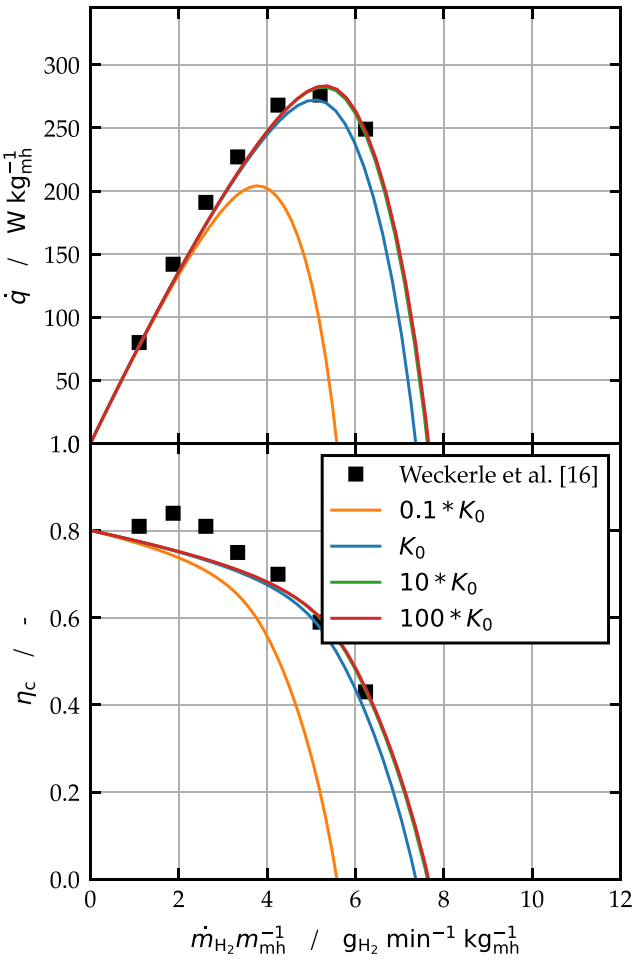

Fig. 8. Influence of the intrinsic kinetic constant K_0 on system performance.

4. Main influences of reactor properties on system performance

While in the previous section, the influences of the operation and boundary conditions for the given validation reactor are described, this section analyses the influence of the reactor itself on the system performance. The proposed model allows to identify which property of the reactor limits the reaction dynamic and the effect is shown when this limitation is overcome. Thereby it is demonstrated how the models can assist future reactor design tasks.

In the following, the individual influences of the reactor properties are analyzed. The influence of heat transfer on the one hand and mass transport on the other hand on the characteristic curves for the specific thermal power and efficiency can be evaluated with the model by setting $\Delta\overline{T}_{mh}$ or $\Delta\overline{p}_{mh}$ to zero, respectively. Another important property of the reactor besides heat and mass transport resistance is the heat capacity of its structural mass, which leads to the previously mentioned capacitive heat losses and is considered with the variable k_C in the describing Eqs. (5) and (7). By setting $k_C = 0$ its influence can be evaluated. The results for the individual disabled limitations are discussed in the following and shown in Fig. 7.

The orange curve in Fig. 7 represents a disabled **heat transport**, whereby the mass transport is still considered. The whole metal hydride bed is then in an isothermal state at the mean temperature of the outer heat transport fluid $\overline{T}_{htf}$, due to an infinite high thermal heat conductivity and heat transfer coefficient. The corresponding curve of the utilization factor is just slightly above the validation curve. Thus, the curves for the maximum specific thermal power and efficiency are as well just on a slightly increased level. This indicates that the system in the current reactor under the applied boundary conditions is not heat transport limited.

The green curve in Fig. 7 represents a disabled **mass transport** resistance, whereby the heat transport is still considered. The applied end desorption pressure in the hydrogen pipe is then also prevailing in the whole metal hydride leading to an isobaric pressure distribution bed due to infinite high gas permeability. The corresponding curve of the utilization factor shows significantly higher possible specific flow rates for the same utilization factor than in the validation case. Hence, the corresponding curve of the specific thermal power has a longer ascending part and later decline after the maximal turning point. As a result, a higher maximum specific thermal power is achieved at a higher specific hydrogen flow. Accordingly, the efficiency is above the validation case in the whole operation range. From this, it can be concluded that the reactor in this setup is limited by its mass transport resistance. Looking at the reactor's layout one can see that the mass transport has a high transport distance through the bed since the through-flow of gas is arranged in the bed length direction, whereas the heat transport distance is arranged in the much smaller bed thickness direction. The mass transport limitation for this reactor was also described by detailed 2D simulations in [15].

In the next step both, the heat as well as the mass transport resistance are disabled. The corresponding red curve shows in the upper plot part of Fig. 7 even higher specific hydrogen flows for the same utilization factor F than in the previous cases, but still a descending course. This is caused by the nature of the kinetic equation, Eqs. (10) and (11), itself. For the specific thermal power, the corresponding curve exceeds the others resulting in an approximately doubled maximum power.

Likewise, the efficiency curve is shifted to higher specific flow rates. Although it is not heat transport limited in its original state, Fig. 7 shows that if the mainly limiting mass transport resistance is eliminated, again the system is heat transport limited and its additional elimination could theoretically improve the performance significantly. It emphasizes the importance of reactor design to consider always both heat and mass transport resistance to identify the limiting factor.

The turquoise curve in Fig. 7 refers to a hypothetical case, in which in addition to the disabled heat and mass transport resistance a massless reactor with vanishing heat capacity is considered. The corresponding curve of the utilization factor is similar to the red one which refers to only disabled heat and mass transport resistance but still considers the **heat capacity ratio** k_C of the validation reactor. The equality of the two curves is obvious since the heat capacity ratio k_C has no influence on the utilization factor, cf. Eq. (17). The capacitive heat losses are only considered in Eqs. (5) and (7) for the specific thermal power and efficiency, respectively. In contrast to the utilization factor, the specific thermal power of this case shows a more than doubled maximum compared to the one, which considers the reactor's heat capacity. The curve shows a maximum although the reactor's heat capacity is not considered. This is caused by the fact that the heat capacity of the metal hydride itself, which cannot be avoided by the best reactor design, is still considered. For the efficiency higher values over the extended operation range in terms of specific hydrogen flow can be observed. Furthermore, it is apparent, that the maximum efficiency at vanishing specific hydrogen flow reaches a higher value, whereas all other curves with the original value of k_C are converging to a single lower value. The results of this hypothetical case point out that besides the importance of a preferable low heat and mass transport resistance, it is also very important to aim for a lightweight reactor design with a preferable low heat capacity.

In order to evaluate the influence of the metal hydride's **intrinsic kinetic** property, the constant K_0 is varied with factors of 1/10, 10, and 100. All other parameters remain the same as for the validation case. The results in Fig. 8 show only a marginal performance increase for ten

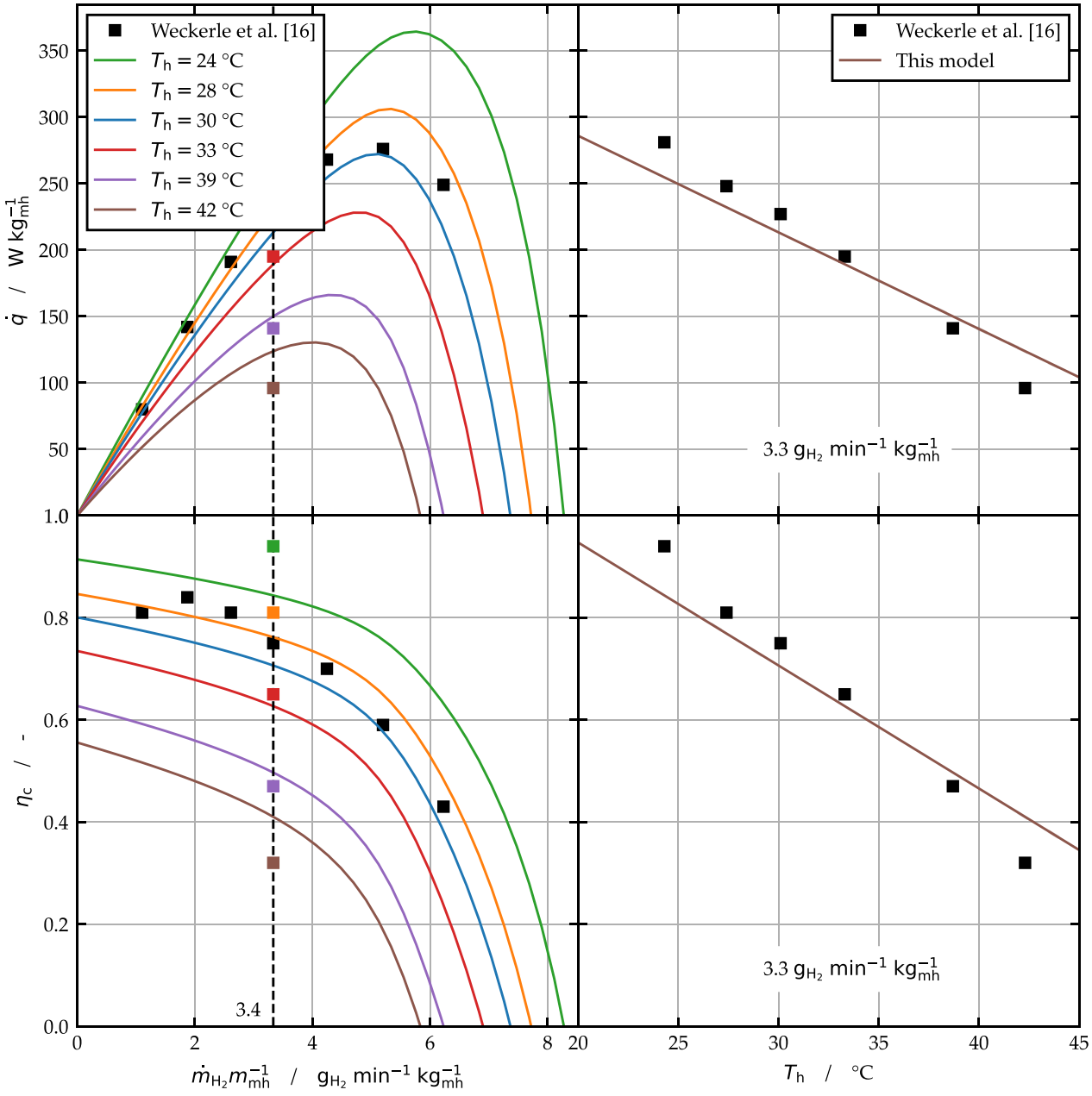

Fig. 9. Influence of different hot side temperatures on specific thermal power and efficiency.

times the original kinetic constant and no further increase for a multiplication by 100. The variation with a tenth of the constant K_0 shows a performance loss to appr. 80 % of the original maximum specific thermal power. This result reveals that the reaction rate and therefore the specific thermal power is not limited by the material's intrinsic reaction constant, but solely by the heat and mass transport resistance and the heat capacity of the reactor. It emphasizes the importance of an elaborated reactor design to exploit the full potential of the system in terms of high specific thermal power and efficiency. The proposed model thereby allows to quickly reveal the potential of a certain metal hydride material under selected boundary conditions.

5. Conclusion

An approach for a lumped model for a quasi-continuous operating open thermochemical heat pump is presented. It is capable of predicting the performance in terms of specific thermal power and efficiency under different pressure and temperature boundary conditions as well as depending on the gas flow rate. The model considers the three main effects, the heat and mass transport resistance with its influence on the conversion of reacted hydrogen per half-cycle and the thermal losses due to the heat capacity of the metal hydride and its surrounding reactor structure. For the heat and mass transport, a steady-state one-dimensional profile is assumed in bed thickness direction which allows to apply the model to typical plane and rational symmetric geometries for loose powder as well as for compacted beds. The metal hydride equilibrium properties are considered by a PCI approximation and the kinetic equation is applied to the lumped metal hydride mass point.

The model is validated over a wide range of boundary conditions (specific hydrogen flow: 1.6–7.6 $g_{H2}\ min^{-1}\ kg^{-1}_{MH}$, cold side temperature: 13–25 °C, hot side temperature: 24–42 °C) with available experimental data for a quasi-continuous operating open heat pump based on metal hydrides. It properly describes the thermal power and efficiency for different specific hydrogen flows. This characteristic curve reveals a maximum for the specific thermal power at an optimal specific hydrogen flow. The governing effects of the quasi-continuous operation are evaluated using the developed model. This is for increasing specific hydrogen flow a high reaction rate that leads on the one hand to high specific thermal power, but on the other hand reduces the conversion, due to the heat and mass transport resistance. As a result, for an increasing specific hydrogen flow, relatively high thermal losses occur which cause a decrease of the resulting thermal power after an occurring maximum. With the knowledge of this characteristic curve, the operation of an existing system can be controlled. For instance, a bypass for hydrogen flows higher than the optimal flow can prevent a decreasing thermal power output. Moreover, the knowledge of the operation characteristic curve of an existing concept is useful for the sizing of the system for an application. It determines the required mass of metal hydride for either the highest specific thermal power or for a more flexible system with a higher efficiency. For that purpose, a Pareto front can be depicted in the operation characteristic curve. Additionally, the model facilitates the fast analysis of the influence of the reactor itself on the system performance. For example, the separate influence of heat and mass transport as well as the reactor heat capacity ratio can be evaluated as demonstrated for the validation reactor revealing its mass transport limitation.

In summary, the validated model can assist the system design of a quasi-continuous operating heat pump system in several stages. Firstly, it can assess the suitability of a certain metal hydride for utilization in such a system under specified temperature and pressure boundary conditions. Secondly, it quickly shows the individual influence of the main influencing effects on the reactor performance, to help finding an optimum reactor design. Lastly, it helps to properly size the system to obtain the favored design criteria, which can be the highest specific thermal power or a more flexible operation behavior with a higher efficiency. Due to its generic approach, basic heat and mass transport modeling and simple kinetic implementation, the model is not only limited to metal hydride systems but could further be applied to other gas–solid reaction systems working in a quasi-continuous mode.

Nomenclature.

Latin letters	
Bi	Biot-number, -
C	heat capacity, $J\ K^{-1}$
c	mass specific heat capacity, $J\ kg^{-1}\ K^{-1}$
d	depth, m
E_a	activation energy, J
F	utilization factor, -
ΔH_r	reaction enthalpy, $J\ mol^{-1}$
K_0	kinetic constant, s^{-1}
k_B	Boltzmann constant, $J\ K^{-1}$
k_T	kinetic coefficient, s^{-1}
k_C	fraction of heat capacities reactor to metal hydride, -
M	molar mass, $kg\ mol^{-1}$
m	mass, kg
$\dot{m}$	mass flow, $kg\ s^{-1}$
p	pressure, Pa
Q	heat, J
$\dot{Q}$	heat flux, W
$\dot{q}_{vol}$	volumetric heat source, $W\ m^{-3}$
$\dot{q}$	metal hydride specific thermal power, $W\ kg^{-1}_{mh}$
R	universal gas constant, $J\ mol^{-1}\ K^{-1}$
r	radius, m
ΔS_r	reaction entropy, $J\ mol^{-1}\ K^{-1}$
T	temperature, K
t	time, s
w	hydrogen capacity, $kg_{H2}\ kg^{-1}_{mh}$
$\dot{V}$	volume flow, $m^3\ s^{-1}$
x	run variable in bed thickness direction, m
z	run variable in bed length direction, m
Greek letters	
α	heat transfer coefficient, $W\ m^{-2}\ K^{-1}$
ε	porosity, -
κ	permeability, m^{-2}
λ	thermal conductivity, $W\ m^{-1}\ K^{-1}$
η	dynamic viscosity of hydrogen, $Pa\ s^{-1}$
η_c	cooling efficiency, -
ρ	density, kgm^{-3}
Subscripts	
ΔT	temperature lift
abs	absorption
c	cold/cooling
des	desorption
eff	effective
end	end (of half cycle)
eq	equilibrium
h	hot
H_2	hydrogen
hc	half cycle
hi	high
ht	heat transfer
htf	heat transfer fluid
i	inner
ini	initial
lift	(temperature) lift
lo	low
max	maximum
mh	metal hydride
min	minimum
mt	mass transfer
o	outer
r	reaction
rt	reactor
t	tank
Abbreviations	
FC	fuel cell
htf	heat transfer fluid
PCI	pressure concentration isotherm
w/o	without

CRediT authorship contribution statement

Alexander Wimmer: Conceptualization, Methodology, Formal analysis, Investigation, Data curation, Writing – original draft preparation. **Marc Linder:** Writing – review & editing. **Inga Bürger:** Conceptualization, Formal analysis, Writing – review & editing.

Declaration of competing interest

The authors declare that they have no known competing financial interests or personal relationships that could have appeared to influence the work reported in this paper.

Data availability

No data was used for the research described in the article.

Acknowledgments:

Discussions with Jonina Felbinger, Eva Klockow, Hanna Lösch and Markus Kordel have been appreciated.

Appendix A

Mean temperature and pressure difference for a rotional symmetric geometry

For a rotation symmetrical geometry with the inner radius r_i and the outer radius r_o, the mean temperature difference $\Delta\overline{T}_{mh}$ of the metal hydride is defined in the same way as for a planar geometry in Eq. (13) and results in Eq. (19). In this case the Bio-number is defined as $Bi = \alpha r_a/\lambda$.

$$\Delta\overline{T}_{mh} = \frac{1}{r_o - r_i}\int_{r_o}^{r_i} T(x)\mathrm{d}x = \frac{\dot{q}r_o^2}{4\lambda}\left(\frac{2}{Bi}\left(1-\frac{r_i^2}{r_o^2}\right) + 2\frac{r_i^2}{r_o^2}\frac{-r_o + \frac{7}{6}r_i - r_i\ln\left(\frac{r_i}{r_o}\right)}{r_o - r_i} + \frac{\frac{2}{3}r_o - r_i}{r_o - r_i}\right) \tag{19}$$

In the case of a rotational symmetric geometry, the same assumptions and the same method as for a planar geometry are used, leading to the following differential equation for the pressure profile:

$$\frac{\mathrm{d}p}{\mathrm{d}r} = \frac{\eta}{\kappa}\frac{RT}{M_{H_2}}\frac{\dot{m}_{H_2}}{m_{mh}}(1-\varepsilon)\rho_{mh}\frac{\left(r_o^2 - r^2\right)}{2pr} \tag{20}$$

The solution arises to:

$$p(r) = \left\{\frac{\eta}{\kappa}\frac{RT}{M_{H_2}}\frac{\dot{m}_{H_2}}{m_{mh}}(1-\varepsilon)\rho_{mh}\left(r_o^2\ln\left(\frac{r}{r_i}\right) - \frac{1}{2}\left(r^2 - r_i^2\right)\right) + p_i^2\right\}^{\frac{1}{2}} \tag{21}$$

For this function, no analytical integral formulation exists. Therefore, the mean integral pressure $\overline{p}_{mh}$ has to be calculated numerically in the case of a rotational symmetric geometry.

Validation on different hot side temperatures

In Fig. 9 on the left side, the characteristic curves for the specific thermal power and the efficiency are shown for different hot side temperatures whereby the cold side temperature T_c remains at 20 °C. The characteristic curves describe the two performance indicators the specific thermal power and the efficiency depending on the applied specific hydrogen flow as the operation condition. The principal shape of the curves with a maximum for the specific thermal power and the continuously decreasing efficiency is the same as for different cold side temperatures. Higher hot side temperatures than 30 °C lead to lower maximums in specific thermal power at lower optimal specific hydrogen flows and also to efficiency curves below each other. For hot side temperatures lower than 30 °C, the behavior is just inversed. On the right side of Fig. 9, the specific thermal power and efficiency are plotted versus the varied hot side temperature at the fixed specific hydrogen flow, which was used in the validation experiment. It shows good agreement between the experimental data and the model results. In comparison to the analog plot for the varied cold side temperature, these curves exhibit a more linear course. It implies that only the temperature difference in Eq. (5) and (7), but not the utilization factor has changed significantly. Furthermore, it can be concluded that in this range of varied hot side temperatures, the absorption is not the limiting process.

References

[1] S.J. Davis, N.S. Lewis, M. Shaner, S. Aggarwal, D. Arent, I.L. Azevedo, S.M. Benson, T. Bradley, J. Brouwer, Y.M. Chiang, C.T.M. Clack, A. Cohen, S. Doig, J. Edmonds, P. Fennell, C.B. Field, B. Hannegan, B.M. Hodge, M.I. Hoffert, E. Ingersoll, P. Jaramillo, K.S. Lackner, K.J. Mach, M. Mastrandrea, J. Ogden, P.F. Peterson, D. L. Sanchez, D. Sperling, J. Stagner, J.E. Trancik, C.J. Yang, K. Caldeira, Net-zero emissions energy systems, Science 360 (2018), https://doi.org/10.1126/science.aas9793.

[2] D.J. Durbin, C. Malardier-Jugroot, Review of hydrogen storage techniques for on board vehicle applications, Int. J. Hydrogen Energy 38 (2013) 14595–14617, https://doi.org/10.1016/j.ijhydene.2013.07.058.

[3] J. Wolf, Liquid-hydrogen technology for vehicles, MRS Bull. 27 (2002) 684–687, https://doi.org/10.1557/mrs2002.222.

[4] J.O. Jensen, A.P. Vestbø, Q. Li, N.J. Bjerrum, The energy efficiency of onboard hydrogen storage, J. Alloys Compd. 446–447 (2007) 723–728, https://doi.org/10.1016/j.jallcom.2007.04.051.

[5] F. Barbir, PEM fuel cells: theory and practice, Academic press, 2012.

[6] N. Muck, S. Wieser, O. Deniz, M. Scharmach, Model-based investigation and evaluation of a hydrogen expansion engine by determining system efficiency as well as market development for heavy-duty hydrogen vehicles, in: 2022 Second International Conference on Sustainable Mobility Applications, Renewables and Technology (SMART), 2022, pp. 1–7.

[7] M. Linder, R. Kulenovic, An energy-efficient air-conditioning system for hydrogen driven cars, Int. J. Hydrogen Energy 36 (2011) 3215–3221, https://doi.org/10.1016/j.ijhydene.2010.11.101.

[8] K. Malleswararao, P. Dutta, S. Murthy, Applications of metal hydride based thermal systems: A review, Appl. Therm. Eng. 215 (2022), https://doi.org/10.1016/j.applthermaleng.2022.118816.

[9] S. Jana, P. Muthukumar, Experimental studies on a closed cycle compressor operated metal hydride based cooling system with large hydrogen inventory, Int. J. Hydrogen Energy (2023), https://doi.org/10.1016/j.ijhydene.2023.07.007.

[10] Y.T. Ge, P.Y. Lang, Performance analysis of a metal hydride refrigeration system, Appl. Therm. Eng. 234 (2023), https://doi.org/10.1016/j.applthermaleng.2023.121264.

[11] K. Meier, C. Kurtz, C. Weckerle, M. Hubner, I. Bürger, Air-conditioning system for vehicles with on-board hydrogen, Appl. Therm. Eng. 129 (2018) 1150–1159, https://doi.org/10.1016/j.applthermaleng.2017.10.087.
[12] C. Weckerle, I. Bürger, M. Linder, Novel reactor design for metal hydride cooling systems, Int. J. Hydrogen Energy 42 (2017) 8063–8074, https://doi.org/10.1016/j.ijhydene.2017.01.066.
[13] C. Weckerle, M. Nasri, R. Hegner, I. Bürger, M. Linder, A metal hydride air-conditioning system for fuel cell vehicles – Functional demonstration, Appl. Energy 259 (2020), https://doi.org/10.1016/j.apenergy.2019.114187.
[14] M. Kölbig, C. Weckerle, M. Linder, I. Bürger, Review on thermal applications for metal hydrides in fuel cell vehicles: Operation modes, recent developments and crucial design aspects, Renewable Sustainable Energy Rev. 162 (2022), https://doi.org/10.1016/j.rser.2022.112385.
[15] C. Weckerle, I. Bürger, M. Linder, Numerical optimization of a plate reactor for a metal hydride open cooling system, Int. J. Hydrogen Energy 44 (2019) 16862–16876, https://doi.org/10.1016/j.ijhydene.2019.04.260.
[16] J. Pöhl, M. Kordel, F. Heckert, A. Wimmer, I. Bürger, Benefit studies of an innovative metal hydride air-conditioning system for FCEVs by using thermal management simulation, in: 2021 ECS simulation conference.
[17] C. Weckerle, M. Nasri, R. Hegner, M. Linder, I. Bürger, A metal hydride air-conditioning system for fuel cell vehicles – Performance investigations, Appl. Energy 256 (2019), https://doi.org/10.1016/j.apenergy.2019.113957.
[18] M.V. Lototskyy, M.W. Davids, I. Tolj, Y.V. Klochko, B.S. Sekhar, S. Chidziva, F. Smith, D. Swanepoel, B.G. Pollet, Metal hydride systems for hydrogen storage and supply for stationary and automotive low temperature PEM fuel cell power modules, Int. J. Hydrogen Energy 40 (2015) 11491–11497, https://doi.org/10.1016/j.ijhydene.2015.01.095.
[19] C.A. Chung, S.-W. Yang, C.-Y. Yang, C.-W. Hsu, P.-Y. Chiu, Experimental study on the hydrogen charge and discharge rates of metal hydride tanks using heat pipes to enhance heat transfer, Appl. Energy 103 (2013) 581–587, https://doi.org/10.1016/j.apenergy.2012.10.024.
[20] D.V. Blinov, V.I. Borzenko, D.O. Dunikov, I.A. Romanov, Experimental investigations and a simple balance model of a metal hydride reactor, Int. J. Hydrogen Energy 39 (2014) 19361–19368, https://doi.org/10.1016/j.ijhydene.2014.07.048.
[21] I. Bürger, M. Dieterich, C. Pohlmann, L. Röntzsch, M. Linder, Standardized hydrogen storage module with high utilization factor based on metal hydride-graphite composites, J. Power Sources 342 (2017) 970–979, https://doi.org/10.1016/j.jpowsour.2016.12.108.
[22] V.M. Skripnyuk, M. Ron, Hydrogen desorption kinetics in intermetallic compounds C2, C51 and C52 with Laves phase structure, Int. J. Hydrogen Energy 28 (2003) 303–309, https://doi.org/10.1016/S0360-3199(02)00081-2.
[23] P. Muthukumar, M. Groll, Erratum to “Metal hydride based heating and cooling systems: A review” [International Journal of Hydrogen Energy (2010) 35: 3817–3831], Int. J. Hydrogen Energy. 35 (2010) pp8816-8829 Doi: 10.1016/j.ijhydene.2010.04.087.
[24] I. Bürger, M. Linder, Operation strategies for gas solid reactions in thermal energy storage systems, J. Energy Storage 40 (2021), https://doi.org/10.1016/j.est.2021.102767.
[25] H. Martin, A theoretical approach to predict the performance of chevron-type plate heat exchangers, Chem. Eng. Process. Process Intensif. 35 (1996) 301–310, https://doi.org/10.1016/0255-2701(95)04129-X.
[26] T. Maeda, K. Nishida, M. Tange, T. Takahashi, A. Nakano, H. Ito, Y. Hasegawa, M. Masuda, Y. Kawakami, Numerical simulation of the hydrogen storage with reaction heat recovery using metal hydride in the totalized hydrogen energy utilization system, Int. J. Hydrogen Energy 36 (2011) 10845–10854, https://doi.org/10.1016/j.ijhydene.2011.06.024.
[27] M. Botzung, S. Chaudourne, O. Gillia, C. Perret, M. Latroche, A. Percheronguegan, P. Marty, Simulation and experimental validation of a hydrogen storage tank with metal hydrides, Int. J. Hydrogen Energy 33 (2008) 98–104, https://doi.org/10.1016/j.ijhydene.2007.08.030.
[28] D.V. Blinov, D.O. Dunikov, A.N. Kazakov, Measuring the gas permeability of a metal hydride bed of the LaNi5 type alloy, High Temp. 54 (2016) 153–156, https://doi.org/10.1134/s0018151x1506005x.
[29] J.-G. Park, K.-J. Jang, P.S. Lee, J.-Y. Lee, The operating characteristics of the compressor-driven metal hydride heat pump system, Int. J. Hydrogen Energy 26 (2001) 701–706, https://doi.org/10.1016/S0360-3199(01)00006-4.

2.2. Paper II: Reactor development

In Paper I a numerical model was developed that represents a well-suited design tool. In the subsequent Paper II it is now applied for designing a new reactor that is specifically optimized for use in an open MHCS. The first Paper I also showed a huge potential to increase the specific power, if the heat and mass transport is further enhanced or the sensible mass of reactor is further reduced. This potential should be now exploited and a higher performance than state-of-the-art experimentally verified. It leads to the particular research question for Paper II:

‚How could a model-based developed MH reactor, specifically for the open MHCS, look like to show a higher SCP than the state of the art?'

Therefore, compacts of MH composites, as a promising option from the literature, were applied for the enhancement of the heat conduction in the MH bed. Moreover, functional integration was realized through additive manufacturing resulting in a sophisticated, but scalable reactor design. In this course, for the first time a reactor for an open MHCS is realized that is pressure-resistant up to 70 bar, despite its lightweight design.

The subsequent experimental characterization was carried out at the same pressure ratio of 7 as in the previous work by Weckerle et al. in order to achieve comparability with the predecessor reactor. The steady-state performance was measured at different specific discharge rates in order to determine the characteristic maximum in the SCP supposed to occur according to the findings in Paper I. A maximum SCP of 511 W/kg_{MH} at reference conditions (20 °C and 30 °C) could be demonstrated, which corresponds to an increase of 89% compared to the state-of-the-art. Additionally, at an increased temperature lift of 20 K, for all investigated temperature sets (10|30°C, 15|35°C and 20|45°C) a significantly higher maximum SCP at a comparable efficiency could be proven. Moreover, the model developed in Paper I could be further validated with the new reactor. In conclusion, the results show that a significantly higher SCP than the state-of-the-art can actually be achieved with a suitable reactor design.

Applied Energy 391 (2025) 125911

Contents lists available at ScienceDirect

Applied Energy

journal homepage: www.elsevier.com/locate/apenergy

High performance reactor of a metal hydride based cooling system for air-conditioning of fuel cell electric vehicles

Alexander Wimmer [a,*], Markus Kordel [b], Marc Linder [a], Inga Bürger [a,*]

[a] Institute of Engineering Thermodynamics, German Aerospace Center (DLR), Pfaffenwaldring 38-40, 70569 Stuttgart, Germany
[b] Institute of Vehicle Concepts, German Aerospace Center (DLR), Pfaffenwaldring 38-40, 70569 Stuttgart, Germany

HIGHLIGHTS

- Open metal hydride cooling as an efficient air-conditioner for fuel cell vehicles.
- Appropriate performance indicators are proposed and design requirements are derived.
- Lightweight reactor design with high heat and mass transport properties is presented.
- Experimental characterization verifies outstanding specific power and efficiency.

GRAPHICAL ABSTRACT

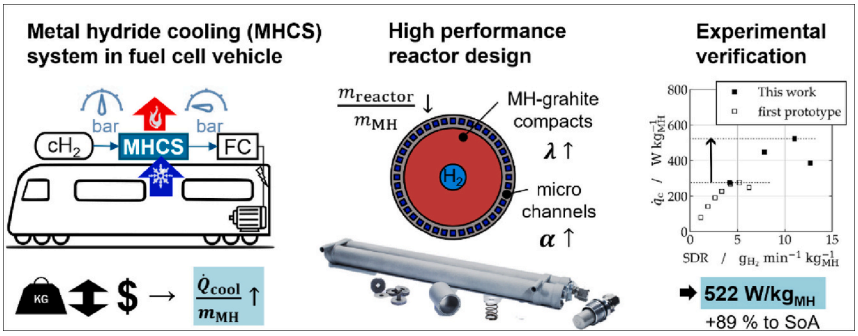

ARTICLE INFO

Keywords:
Metal hydrides
Reactor design
Cooling
Air-conditioning
Fuel cell electric vehicles

ABSTRACT

Refueling fuel cell electric vehicles (FCEVs) needs energy for the compressor at the refueling station that is afterwards stored inside the high-pressure tank on board of the vehicle. On the one side, the State of the Art does not allow to recover this energy which results in a negative impact on the efficiency chain of a FECV. On the other side, air-conditioning systems in vehicles consume significant amounts of energy, further reducing the limited driving range and increasing the operation costs. This problem can be addressed by the open metal hydride cooling system (MHCS) arranged between the pressure tank and fuel cell, that converts the available potential energy into a heat pump effect. The challenges of the MHCS is its thermal performance referred to the amount of metal hydride (MH) that is required. This study presents a reactor design that significantly increases the specific cooling power of previous MHCS. The new reactor features MH-graphite composites and micro fluid channels for heat transport enhancement as well as an additive-manufactured lightweight structure of aluminum to reduce sensible losses. Experimental characterization at a pressure ratio of 7, a cold side temperature of 20 °C and hot side temperature of 30 °C show a specific cooling power of 522 W kg_{MH}^{-1}, that is nearly twice as high as the best value reported in the literature. Furthermore, not only cooling efficiencies above 60 % could be maintained on higher specific power, but also the performance at an elevated temperature lift of 20 K is improved in comparison to previous systems. The experimentally proven high performance verifies the good heat and mass transport properties with a low structural heat capacity at the same time. This significantly improved reactor allows to meet the demanding requirements in terms of weight, space and cost for the applications in the mobile application such as a FCEV.

* Corresponding authors.
E-mail addresses: alexander.wimmer@dlr.de (A. Wimmer), inga.buerger@dlr.de (I. Bürger).

https://doi.org/10.1016/j.apenergy.2025.125911
Received 18 November 2024; Received in revised form 23 January 2025; Accepted 7 April 2025
Available online 18 April 2025

1. Introduction

As part of the worldwide energy transition it is established that hydrogen can play a significant role, since it represents a versatile energy carrier that can store renewable energy in large quantities [1]. Hydrogen can be used among other purposes as a fuel for vehicles where it powers a combustion engine or a fuel cell (FC). Especially FC vehicles are a promising solution for the usage of hydrogen in the mobility sector as they exhibit significant advantages in efficiency, noise and nitrogen oxide pollution in comparison to combustion engines. Current research and industrial development for FC vehicles focus on heavy duty vehicles like trucks, buses and also trains, where the advantages in driving range, refueling time and weight can compensate the complexity and higher costs compared to battery electric vehicles. For the on-board storage of hydrogen, high-pressure tanks with 350 bar and 700 bar are State-of-the-Art. Although this storage option is less energy intensive than liquification, refueling a 700 bar-tank requires still approximately 15 % of the hydrogen's energy content [2]. Since FCs do not require that high pressure to work, but operate at 1 up to 3 bar on cell level, parts of the compression work could be recovered. For a 700 bar-tank, additional 7.5 % of the usable electrical energy can be gained theoretically considering an isothermal expansion to 5 bar [3]. The obvious possibility to recover the compression work is by utilizing a mechanical expansion machine [4]. Another more widely studied possibility is by applying a thermochemical reaction of hydrogen with metal hydrides (MH) on different pressure and temperature levels to realize a heat pump or cooling effect [5]. Since the air-conditioning reduces the driving range in a fuel cell car by up to 20 % [6], such a system can support or even replace the existing air-conditions systems without consuming hydrogen and therefore enhances the overall efficiency of the vehicles. Thus, it increases the driving range and reduces operation costs.

In literature, this system is denoted as open MH cooling system (MHCS) and represents one special kind of MH thermal system. It is considered as an open system, since it has to be integrated into an existing hydrogen path with an available pressure difference. Therewith, it differs from the more widely studied heat driven [7] or the compressor driven MH cooling systems [8], that represent closed systems. Linder et al. [5] were the first proposing and experimentally studying the MH cooling system as an open system removing the thermal or mechanical compressor and replacing it with the already available pressure difference that occurs in a FC vehicle with a high-pressure tank. Fig. 1, illustrates this concept of the open MHCS applied between the high-pressure tank and the fuel cell. Hydrogen from the tank is throttled first to a constant high pressure (e.g. 30–100 bar) at which it is absorbed in reactor 1. During this exothermic absorption heat is released to the ambient until the full capacity of the metal hydride is reached. In parallel the previously absorbed reactor 2 desorbs hydrogen on the low-pressure side to the FC (typically 5–10 bar), leading to an endothermic reaction that takes up heat on a lower temperature than the previous absorption, according to the van't Hoff law. Subsequently, the hydrogen valves are switch in order to let reactor 2 absorb hydrogen from the tank and release heat to the ambient, while now reactor 1 is producing cold and feeding hydrogen to the FC. This alternating switching between two subsequent half cycles leads to a quasi-continuous operation where the open MHCS acts as a heat pump. Fig. 1 also shows the main requirements from an application point of view, that are a high cooling power, low amount of MH required and a high temperature lift to enable many integration options in FC vehicles.

Linder et al. [5] already demonstrated the function of an open MHCS at relevant pressure conditions of 50 bar and 6 bar for absorption and desorption, respectively. However, their experiments were not conducted under realistic operation condition, since the pressure was set constant at the outlet of the desorbing reactor. In a real application in contrast, where hydrogen flows through the open MHCS to a FC at steady state, a constant hydrogen mass flow represents the more realistic boundary condition. Consequently, Weckerle et al. [9] conducted experiments with a fuel cell coupled to the hydrogen outlet of the MHCS. In that study the operation mode on constant desorption flow was experimentally proven by using a reactor based on a plate heat exchanger.

For MH thermal systems in general it is widely reported in literature that increasing the thermal performance is a challenge [10]. This applies also to the open MHCS and can therefore be specified by three main performance indicators, cf. Eq. (1)–(3). The first one is the specific cooling power $\dot{q}_c$ referred to the applied mass of MH material, cf. Eq. (1). It is a crucial performance indicator since it determines the required mass of MH m_{MH} for a certain thermal power $\dot{Q}_c$ and thus mainly influences the weight, size and cost of the open MHCS. In contrast, in the conventional application of MHs as a hydrogen storage, the required mass of MH is almost solely determined by the hydrogen capacity of the material [11]. Therefore, the reactor design has a minor influence on the required mass of MH. However, for thermal applications, where the reactor acts as a power converting component instead of a storage container, the reactor itself is mostly the crucial component restricting

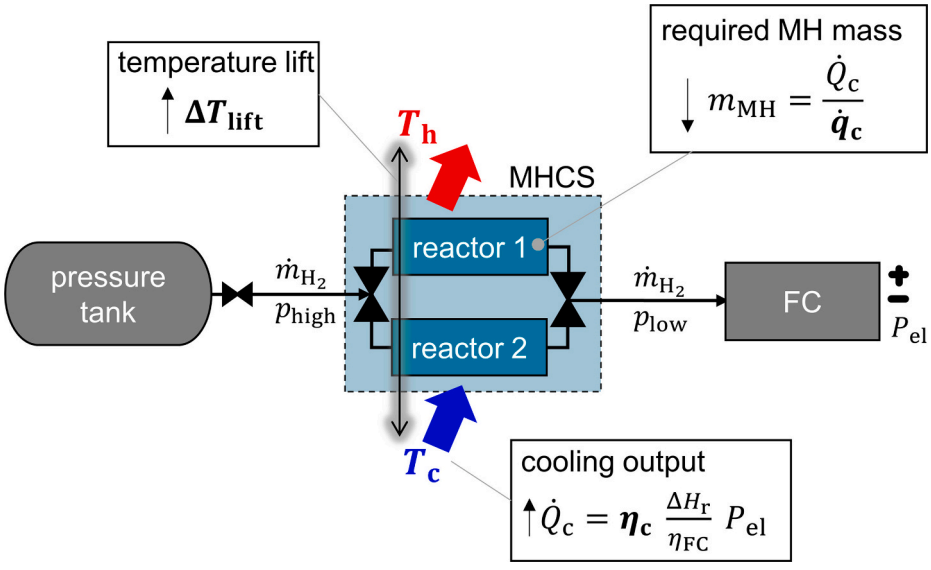

Fig. 1. Integration of the MHCS into the hydrogen path of a FC vehicle and development targets.

the specific cooling power and thus determining the required amount of MH material. For that reason, the reactor of an open MHCS is rather comparable to the reactor designs of a MH hydrogen compressor, described for instance in [12].

The second performance indicator is the cooling efficiency η_c. It is defined according to Eq. (2) as the actual cooling power referred to the product of the applied hydrogen mass flow $\dot{m}_{H_2}$ and the reaction enthalpy ΔH_R. First introduced by Weckerle et al. [13] it can be considered as the efficiency of the reactor with respect to the materials maximum and acts explicitly not as a thermodynamic efficiency. It is obviously also an important performance indicator as it directly describes the thermal output at a given hydrogen flow rate. For a constant FC efficiency ($\eta_{FC} = \frac{P_{FC}}{\dot{m}_{H_2}} = \text{const.}$) the thermal power output is proportional to the FC power multiplied by the cooling efficiency. Consequently, the cooling efficiency has to be high to achieve a high thermal power output for a given FC setup.

The third performance indicator to be mentioned is the actually achievable temperature lift, defined as the difference between the hot side temperature T_h and cold side temperature T_c, cf. Eq. (3). The temperature lift can be considered as a measure of the grade of the generated cold. Besides this thermodynamic characterization, the temperature lift has a practical importance as well. The higher the hot side temperature, the easier the heat can be dissipated to the ambient, leading to a smaller air heat exchanger for. At the cold side, a lower temperature enables the utilization of a smaller heat exchanger or to use a lower air stream at the same heat exchanger to transfer the same cooling power to the compartment, but with lower outlet velocities. Lower cold side temperatures can also enable the possibility to dehumidify the air. Thus, the specific cooling power and cooling efficiency have to be considered with respect to the achieved temperature lift.

$$\textbf{Spec.cooling power } \dot{q}_c := \frac{\dot{Q}_c}{m_{MH}} \tag{1}$$

$$\textbf{Cooling efficiency } \eta_c := \frac{\dot{Q}_c}{\Delta H_R \, \dot{m}_{H_2}} \tag{2}$$

$$\textbf{Temperature lift } \Delta T_{lift} := T_h - T_c \tag{3}$$

The limits of the three performance indicators are determined by the pressure and temperature boundaries and the selected MH material. But at specific boundaries and a chosen MH material, they only depend on the design of the reactor, which makes them suitable parameters to assess the design quality.

There are many of studies of MH reactors as thermal energy converter in literature. Most of them relate to the known closed MH system with 4 reactors and 2 pairs of different MH materials for cold generation or heat pumping. However, closed MH systems and the open MHCS differ strongly in their mode of operation, being thermally driven in the case of typical closed system in contrast to being hydrogen pressure and mass flow driven for open systems. Consequently, performance indicators like the specific cooling power cannot be compared directly. Recently, also open MH systems for thermal applications are investigated more widely. A comprehensive overview of closed and open MH thermal systems with the differentiation between continuous and discontinuous systems was published by Kölbig et al. [3]. Although there are open systems in literature with specific cooling powers >1 kW/kgMH, they are obtained just in a single discharge process as peak power of a discontinuous operation (e.g. for application as a preheater/precooler). This is again not comparable to the average thermal power of a quasi-continuous operation by the open MHCS in two half cycles. The study of Weckerle et al. [13] represents the only available literature data known to the authors for an open MHCS on a constant desorption flow rate. There, a maximum specific cooling power of 276 W kg_{MH}^{-1} at a cooling efficiency of 60 % was achieved at a temperature lift of 10 K. At a higher temperature lift of 22 K the specific cooling power was reduced to 96 W kg_{MH}^{-1} at a cooling efficiency of 32 %. Therefore, this data is used as a reference for the present work.

These reference experiments were conducted at an absorption pressure of 35 bar with a desorption end pressure of 5 bar leading to a pressure ratio of 7. However, many FC systems require inlet pressures higher than 5 bar to insure proper hydrogen recirculation in the anode loop and also proper purging [14]. When applying a higher desorption end pressure to the same system, corresponding simulations [15] suggest that the thermal power will decrease. Thus, the aim of this work is to develop, build and experimentally demonstrate a new reactor that outperforms the best published reactor in literature for an open MHCS in terms of the above-mentioned indicators, namely the specific cooling power, cooling efficiency and temperature lift. Additionally, the system should demonstrate for the first time the quasi-continuous cold generation of an open MHCS at a back pressure of 10 bar. Therefore, as a first step explicit design requirements, that apply to any quasi-continuous thermochemical heat pumps, are analytically deduced from a previously published model. Considering these requirements, a new design is then exemplarily realized on a small but scalable size. Finally, the new reactor is systematically characterized to evaluate its performance on different steady-state operation points.

2. Reactor design

The design methodology consists of a detailed deduction of the design requirements for reaching a high thermal performance. Following this, ring-shaped MH pellets with a central radial gas supply and radial heat dissipation to the surrounding reactor tube are identified as a promising concept that is capable of fulfilling the requirements to a high extent. The specific dimensioning, especially of the diameters, is then based on principal considerations, practical manufacturing limits and simulative parameter variations (not part of this work) to find an optimum of the ring width for the MH pellets. The final design is presented in detail with all determined dimensions and their justification.

2.1. Deduced design requirements

At first, definite design requirements for the reactor are deduced in order to improve the above mentioned three performance indicators in the course of the MCS development.

For the cooling efficiency as the second performance indicator, the sensible heat loss is the dominating aspect that occurs at each switching event from the heating (absorption) half cycle to the cooling (desorption) half cycle. The sensible heat loss depends on the temperature difference between hot and cold side and the heat capacity of the reactor. The ratio of the reactor heat capacity to the one of the MH can be denoted as k_C according to Eq. (4):

$$k_C := \frac{C_{rt}}{C_{mh}} = \frac{c_{rt} m_{rt}}{c_{mh} m_{mh}} \tag{4}$$

The variables C_{rt} and C_{mh} herein represent the absolute heat capacities of the empty reactor and MH material respectively, and c_{rt} and c_{mh} their corresponding mass specific heat capacities. Eq. (5) can be formulated for the cooling efficiency η_c considering a lumped 0D-model [16]. It incorporates the heat capacity ratio k_C and the temperature lift ΔT_{lift} and shows their decreasing influence on η_c.

$$\eta_c = 1 - \frac{c_{mh}(1 + k_c)\,\Delta T_{lift}}{\Delta w \, \frac{\Delta H_{R,Des}}{M_{H_2}}} \tag{5}$$

Herein M_{H_2} denotes the molecular mass of hydrogen and the variable Δw denotes the reacted fraction of hydrogen per MH material in wt.-%. This conversion Δw can be increased to the materials maximum Δw_{max} by applying a sufficient small specific hydrogen mass flow as operation condition. Consequently, for a given material and temperature lift the only reactor specific parameter in Eq. (5) is given by k_C. Thus, reducing

k_C can be deduced as the single design requirement to improve the cooling efficiency η_c.

In contrast to the cooling efficiency, the specific cooling power as the first performance indicator is not solely determined by the sensible heat losses. Instead it is also limited by the heat and mass transfer resistance inside the reactor. The specific cooling power can be described with Eq. (6) for a lumped model [16].

$$\dot{q}_c = \frac{\dot{Q}_c}{m_{MH}} = \frac{\dot{m}_{H_2}}{m_{MH}} \left(\frac{\Delta H_{R,Des}}{M_{H_2}} - \frac{c_{mh}\,(1+k_C)}{\Delta w}\,\Delta T_{lift} \right) \tag{6}$$

Herein $\dot{m}_{H_2} \backslash m_{MH}$ denotes the specific discharge rate. Its linear influence on the specific cooling power is obvious. The influence of the heat and mass transport resistance rate on the specific cooling power is not directly recognizable in Eq. (6). But increasing it, decreases the reacted fraction Δw due to the heat and mass transport resistance [17]. Hence the cold generated per half cycle decreases until a further increase of the discharge rate does not increase the cooling power anymore, instead it decreases after passing a maximum [16]. Therefore, lowering the heat and mass transport resistance can be deduced as a second design requirement additionally to a low k_C. They can be specified as the temperature difference $\Delta T_{bed}/\dot{q}$ and the pressure difference $\Delta p_{bed}/\dot{q}$ over the reaction bed per applied heat source, respectively.

The theoretically achievable temperature lift, as the third performance indicator, is determined by the MH material's equilibrium properties and the applied pressures for absorption and desorption. To achieve a reasonable specific cooling power and cooling efficiency at a preferably high temperature lift, the heat capacity ratio k_C has to be small in order to keep the sensible heat losses small. Consequently, as well as for the cooling efficiency itself, lowering the value of k_C as much as possible is deduced as the single design requirement to increase the usable temperature lift.

In summary, realizing low values for the three parameters k_C, $\Delta T_{bed}/\dot{q}$ and $\Delta p_{bed}/\dot{q}$ can be deduced as design requirement to achieve high values for the above-mentioned performance indicators. While for a high cooling efficiency and usable temperature lift it is sufficient to keep the heat capacity ratio k_C low, for a high specific cooling power at the same time, the heat and mass transport resistance have to be low as well. This, however, represents conflicting goals. It can be easily seen considering a plate reactor [18]. Increasing the number of heat exchanger plates on the one hand enhances the heat transport, but on the other hand increases also the heat capacity of the reactor. In contrast, a decreased number of plates lowers heat capacity of the reactor beneficially, but at the same time deteriorates the heat transport properties. This makes the specific cooling power the most challenging performance indicator and requires a model-based design to find the optimal compromise between good heat and mass transport properties and a low reactor mass.

Besides the above deduced requirements, further aspects like pressure resistance and leak tightness for hydrogen and the heat transfer fluid (HTF) have to be adhered to. Additionally, the expansion compensation for the MH bed, filter integration, the filling procedure of MH and the manufacturability have to be considered in a new reactor design.

2.2. Realized reactor concept

In order to achieve the targets of this work of a high thermal performance and at the same time the operation on a specified desorption pressure of 10 bar, the reactor concept presented in the following contains first the selection of an appropriate MH material and second the reactor design itself.

The MH material $Ti_{0.99}Zr_{0.01}V_{0.43}Fe_{0.09}Cr_{0.05}Mn_{1.5}$ [19] is selected, in order to enable the new reactor to operate with FC systems, that require a higher supply pressure than 5 bar. This MH material is also known under the brand name ‚Hydralloy C1'from the German manufacturer GfE (Gesellschaft für Elektrometallurgie mbH). According to its equilibrium characteristic shown in Regarding the cyclic stability, Wanner et al. found only a small degradation of 10 % in hydrogen capacity for C2 in 85,100 cycles [21], which corresponds to 4255 h of operation at a half cycle time of 150 s. This good cycling stability is also assumed to be valid for C1, since it belongs to the same class of AB2-Laves-Phase type materials. Summarizing the material comparison, the premise can be stated that the reactor performance in this study can be compared with the previous prototype despite the usage of a slightly different material.

Fig. 2, this material exhibits a beneficial low desorption temperature of 2 °C even at a pressure of 10 bar.

In comparison, for the almost similar material $Ti_{0.98}Zr_{0.02}V_{0.41}Fe_{0.09}Cr_{0.05}Mn_{1.46}$ (brand name 'Hydralloy C2') [20], that was utilized in the previous study by Weckerle et al., the desorption pressure of 10 bar leads to an equilibrium temperature of 20 °C which does not allow to produce cold in that case. Hence it is not suitable to operate at 10 bar. A lower desorption pressure of 5 bar would be required to reach a temperature close to 0 °C, cf. Fig. 2.

However, for the finally selected material C1 the low equilibrium temperature at 10 bar comes at a price. At the absorption side it requires a significantly higher pressure of 70 bar to reach a reaction temperature close to 60 °C, whereas for the previous used C2 a pressure of 30 bar was sufficient to reach the same temperature. Finally, although the pressure levels are increased (70 bar for absorption and 10 bar for desorption compared to 35 bar and 5 bar for the previous study), the same pressure ratio of 7 is applied. This ensures direct comparability for the following experimental results despite different absolute pressures, since the energy effort to drive the MHCS depends mainly on the pressure ratio.

Except for the different equilibrium pressures, both materials are very similar in their properties, as listed in Table 1, due to an almost similar alloy composition. For instance, both materials exhibit the same maximum hydrogen capacity w_{max} of 1.75 wt.-%. Regarding the other properties, the values corresponding to the desorption are the most important ones, since the desorption represents the determining half cycle. The desorption enthalpy of C1 exceeds the one of C2 by 3.2 %. C1 shows on the one hand a beneficial lower plateau slope for the

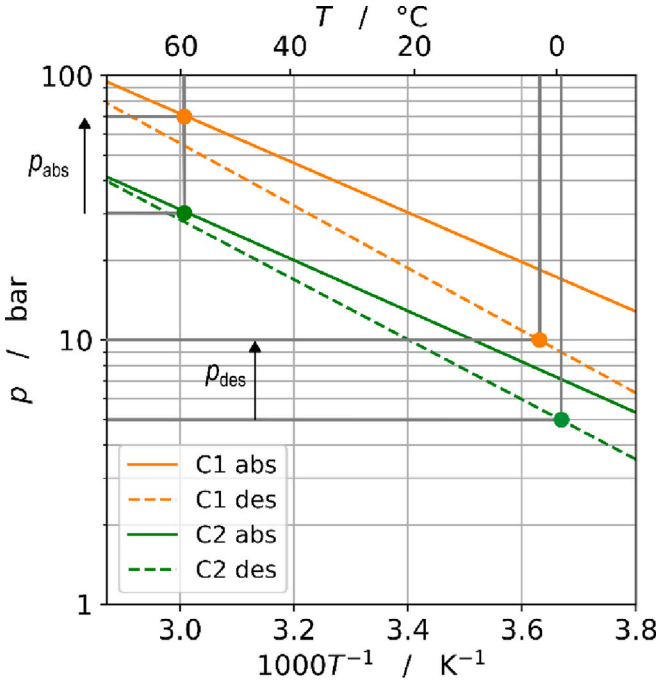

Fig. 2. Equilibrium lines at 0.5*w_{max} for absorption and desorption for the MH materials Hydralloy C1 and C2 (data from [5,15]).

Table 1
Material properties of selected MH materials.

	Hydralloy C1	Hydralloy C2
Alloy composition	$Ti_{0.99}Zr_{0.01}V_{0.43}Fe_{0.09}Cr_{0.05}Mn_{1.5}$ [19]	$Ti_{0.98}Zr_{0.02}V_{0.41}Fe_{0.09}Cr_{0.05}Mn_{1.46}$ [20]
Reaction enthalpy ΔH_R (Abs/Des) [J mol_{H2}^{-1}]	17,922 / 22,606 [5]	18,384 / 21,712 [15]
Plateau slope (Abs/Des) [−]	0.42 / 0.22 [5]	0.47 / 0.42
Hysteresis [−]	0.27	0.11
w_{max} [wt.-%]	1.75 [5]	1.75 [9]

desorption. On the other hand, it exhibits a higher hysteresis between the absorption and desorption pressure. The kinetic coefficient has a very small influence on the performance of a MHCs, as an analysis by means of an analytical model [16] for the previous reactor showed, since the system is mainly heat and mass transport limited. Regarding the cyclic stability, Wanner et al. found only a small degradation of 10 % in hydrogen capacity for C2 in 85,100 cycles [21], which corresponds to 4255 h of operation at a half cycle time of 150 s. This good cycling stability is also assumed to be valid for C1, since it belongs to the same class of AB2-Laves-Phase type materials. Summarizing the material comparison, the premise can be stated that the reactor performance in this study can be compared with the previous prototype despite the usage of a slightly different material.

The reactor design itself is designed from scratch. This allows to best satisfy the requirements above, implying a good heat and mass transfer, but also a lightweight but pressure-resistant system. In contrast, commercial heat exchangers, that were used in the studies of Weckerle and Linder [5,9], are typically not optimized for a small intrinsic heat capacity and often not designed for pressures above 50 bar.

As the basic geometry for the new reactor, a cylindrical tube is chosen, as it is the best shape for a pressure vessel after a spherical shape. Thus, small wall thicknesses can be used to keep the structural mass of the reactor small, in order to achieve a low heat capacity of the reactor. Moreover, a tube reactor is easily scalable in length and modular by using several tubes in parallel as a tube bundle as investigated in [22]. As a quite simple geometry, it is also beneficial for modelling and simulation. According to Yang et al. [23] such a tubular reactor represents one of the three typical configurations, that is used since the early investigations on MH heat pumps. Due to its specific advantages it is still present in a most recent study related to a closed MH heat pump [24].

In order to enhance the heat conductivity inside of the MH bed, compacted composites of the MH material with a mixture of 15 wt% ENG (Expanded Natural Graphite) were used. MH-ENG composites with that amount of ENG are reported to show of approximately 10 W m^{-1} K^{-1} as a stable value for the effective radial heat conductivity after several cycles [25,26]. This value is significantly higher than for pure MH powder, showing approximately 1 W m^{-1} K^{-1} [27]. The stability of the thermal properties for MH-ENG composites was already proven over 1000 cycles [25]. Such composites are subject of current advanced reactor developments, for instance in MH hydrogen compression systems [28].

After this basic design choices, the principle concept of the new reactor is finalized by the definition of the heat management and the hydrogen supply. The heat transfer from the MH-ENG compacts to the HTF is realized radially to the reactor wall in which a HTF flows. The gas supply is also designed radially, but from the inner center. The necessary hole inside the MH-ENG compacts leads to a ring-shape that builds a distribution channel along the tube axis for the hydrogen. This easy-to-implement measure ensures a much shorter mass transfer only through the ring width of the compacts instead of through the whole reactor length, if no central distribution channel exists. Since heat and mass transport are both in radial but opposite direction, this arrangement supports the occurrence of a homogeneous reaction along the bed thickness, that is easier to control and model than a reaction front appearing in radial direction. This basic concept is shown in a cross section of the reactor main part in Fig. 3.

For the selection of the specific diameters marked in Fig. 3, principle considerations like manufacturing limitations and assembly needs as well as simulative parameter studies were considered. At first the inner channel should be as small as possible to avoid unused space and to keep the outer diameter small which allows using a thin wall thickness. However, it should not be too small to avoid a significant flow resistance. Moreover, it should allow the insertion of a rolled-up wire mesh for stabilization and the insertion of an assembly helper tool for filling the reactor tube with the stacked compacts. Finally, 4 mm were chosen as a design assumption for the inner diameter. Regarding the selection of the outer diameter, the ring width is constrained to a minimum of approximately 2 mm to ensure a proper handling of the compressed MH-ENG composites.

Different variations for the outer diameter of the MH-ENG composites were evaluated by using the model published in a previous study [16] to find an optimum between short heat transport distance but also low sensible mass ratio k_C. As final dimensions, an outer diameter of 14 mm were chosen. However, the inner diameter of the reactor tube was designed to 15 mm, in order to allow radial expansion of the inserted composites during activation. After that the MH-ENG compacts are expected to be in direct contact with the inner wall of the reactor tube. It leads to a final reaction bed thickness of 5.5 mm, cf. Fig. 3.

The heat transfer is realized inside the wall of the reactor surrounding the MH-ENG composites. Therefore, axial micro channels are incorporated in order to achieve a high heat transfer coefficient in the herein dominating laminar flow regime. Micro channels are a well-known technique in compact heat exchangers and more recently also reported in advanced MH reactor designs [29,30]. The micro channels in this reactor are of quadratic shape and exhibit a side length of 0.8 mm, cf. Fig. 3. The manufacturability of that integrated micro structure is realized by the use of additive manufacturing. According to the appropriate Nusselt correlation [31] the heat transfer coefficient at 0 °C and operated flow rates up to 2 l min^{-1} is calculated to 1500–2300 W m^{-2} K^{-1}.

For the analytical design evaluation and comparison with a plate reactor in Sec. 2.3 it is necessary to refer the heat transfer only to the

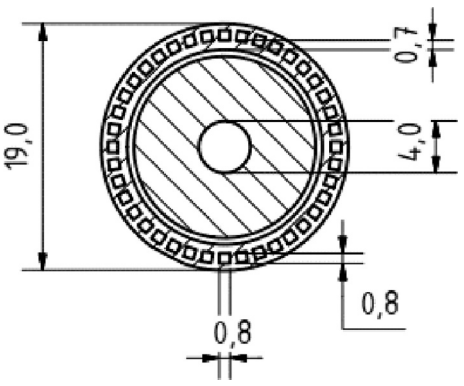

Fig. 3. Cross section of reactor tube with MH-ENG-composites (dimensions in mm).

lateral surface of the reactor tube. Therefore, a factor of 2.5 is calculated as the heat transfer area of the realized micro channels divided by the lateral surface of a reactor tube without microchannels. This leads to a heat transfer coefficient of 3750–5750 W m^{-2} K^{-1} referred to a simple lateral tube surface with an outer diameter of 16.4 mm. Herein an equal heat transfer on all four sides of the micro channel is assumed.

As the construction material for the reactor, the lightweight and high-strength aluminum alloy AlSi10Mg was used. In comparison to the widely used austenitic steel 316L it exhibits an approximately 10 times higher heat conductivity and a roughly 40 % lower volumetric heat capacity at a comparable strength and hydrogen compatibility. Therefore, aluminum is a beneficial choice as structural material for MH applications focusing on thermal performance and is also proven in hydrogen storage applications [32]. The reactor was manufactured in an additive power-bed process, specifically in the selective laser melting (SLM) process. This allows a fast prototyping in few manufacturing steps and has already showed its suitability for MH-reactors in several other studies [33,34]. Although this manufacturing technique allows a high design freedom, this freedom was not fully exploited, since it should be possible, after some modifications, to produce the reactor by conventional manufacturing methods in the future.

The required wall thickness for the reactor tube and the dished and plane heads were calculated according the ASME code. In a conservative assumption, for the reactor tube with its incorporated micro channels, only the inner wall was considered as the supporting structure. The chosen wall thickness of 0.7 mm below the micro channels, cf. Fig. 3, leads to a factor of safety of 2.5 at the operating pressure of 70 bar.

Fig. 4 shows the final design, that is 284 mm in length and consists of 2 tubes of 19 mm outer diameter with common connections for the heat transfer fluid inlet and outlet. A spring allows the compensation of MH expansion of 5 % in axial direction, as the sectional view in Fig. 5 shows. The two caps are manufactured by lathing, using the high-strength alloy *Al* 6082-T6. They provide a pipe nozzle with an attached grip-type tube fitting for the hydrogen connection each. The cabs are screwed inside the reactor tube, sealed by an O-ring (applying DIN ISO 3601) and connected to each other by external pipes. Both are equipped by a sinter-metal filter that have a mean pore size of 0.5 µm, which is assumed to be fine enough since Wanner et al. determined a mean particle size of 7 µm for Hydralloy C1 in fully activated condition [21]. Furthermore, it is expected that the initial pressure surge at the beginning of the absorption half cycle at constant pressure supports the purging of the filter and reduces the tendency for filter blocking. The stack of MH-ENG composites is additionally equipped in its center hole with a rolled-up metal mesh to act as inner stabilization and first filter barrier. The reactor including all the additional parts shown in Fig. 4, but without MH-ENG compacts, has a mass of 172 g. It is then filled with the MH-ENG composites that are prepared from 174 g of MH and 31 g of ENG. According to the maximum hydrogen capacity of the used MH material the reactor is able to store 3.1 g of hydrogen.

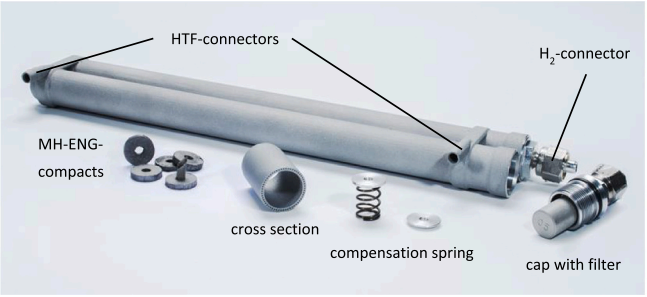

Fig. 4. Reactor with caps and all inner parts and an additional part showing the cross section.

2.3. Design evaluation

The resulting relevant properties for the presented design, denoted as reactor 2.0, are evaluated and compared in Table 2 to the previous plate-based design, denoted as reactor 1.0. The very important thermal mass ratio k_C, that is important for all three performance indicators, could be reduced to 2.2 compared to 3.2 for the first prototype. This could be realized by carefully adjusting the wall thicknesses, a higher bed thickness than reactor 1.0 and the use of the light but high-strength aluminum alloy compared to the stainless steel of reactor 1.0. (In Table 2 the higher bed thickness is represented by the equivalent heat transport length L_{ht}). Without considering the tube fittings, the thermal mass ratio of reactor 2.0 is even 1.6, which is half the value of the previous reactor. This value is assumed to be more realistic for larger sizes of the reactor, where the influence of the fittings will be reduced in comparison to the relatively small sized one of this study. Moreover, also the mass ratio without heat capacities is reduced by 50 % compared to the previous reactor and falls even below one, if the fittings are not considered.

The higher bed thickness of 5.5 mm compared to 0.88 mm for reactor 1.0 on the one hand reduces the thermal mass ration k_C, but on the other hand increases also the heat and mass transport distance. To still realize a small heat transport resistance, MH-ENG-composites are used due to the higher effective heat conductivity λ compared to MH powder and micro HTF channels due to high heat transfer coefficient α to the surrounding fluid. These measures result in slightly lower a heat transport resistance in terms of temperature difference per volumetric heat generation of 1.4 K W^{-1} cm^{-3} compared to 1.5 K W^{-1} cm^{-3} of the first prototype. The Biot number of 2.5 for this study compared to 0.6 reveals that the new reactor is rather limited at the inner heat conduction, while the first prototype is limited at the outer heat transfer to the HTF. For the comparison of both reactors an inner heat conduction resistance between the MH bulk or compact to the reactor wall is neglected.

The mass transport resistance in terms of pressure drop per volumetric hydrogen flow could also be reduced significantly from 10.5 to 1.0 bar g_{H2}^{-1} s cm^3, although the permeability κ of MH-ENG-composites is reported to be much lower than the one of powder bulk used in reactor 1.0. Pohlmann et al. measured a permeability of 3.9e-15 m^2 after 85 cycles for similar Hydralloy C5 pellets but with 5 wt% ENG [26]. For the compacts of this study, comparison between model and experiments showed best accordance for a value of 1.5e-15 m^2, that is in the same order of magnitude as the literature value of Pohlmann. In contrast the pure powder in reactor 1.0 shows a significant higher permeability by 2 orders of magnitude of 1.75e-13 m^2 [16]. Despite that, the reduction of the mass transport resistance for reactor 2.0 is achieved since the center hole of the composites reduce the mass transport distance L_{mt} to just the radial bed thickness, instead of the whole bed length as in reactor 1.0.

3. Experimental setup

The new reactor introduced in the previous section promises a high thermal performance due to its high heat and mass transport capability along with its low structural mass. In order to proof it experimentally, a test setup is required, that will be presented in the following section. It comprises the HTF fluid and hydrogen side as well a control unit for the correct half cycle switching.

The reactor is connected via two 3/2-way ball valves to two HTF loops, each for the hot and the cold side, cf. Fig. 6. Two thermostatic baths with integrated pumps simulate the behavior of an ideal heat sink or source by compensating the produced heat or cold of the reactor and providing a constant inlet temperature to the reactor. As HTF, a mixture of water and 50 Vol.-% nonethylene glycol was used, since it is a commonly used fluid in automotive cooling loops with anti-freeze properties in the range of vehicle operation conditions. The flow rate of the HTF $\dot{V}_{HTF}$ was set constant for each experiment according to the

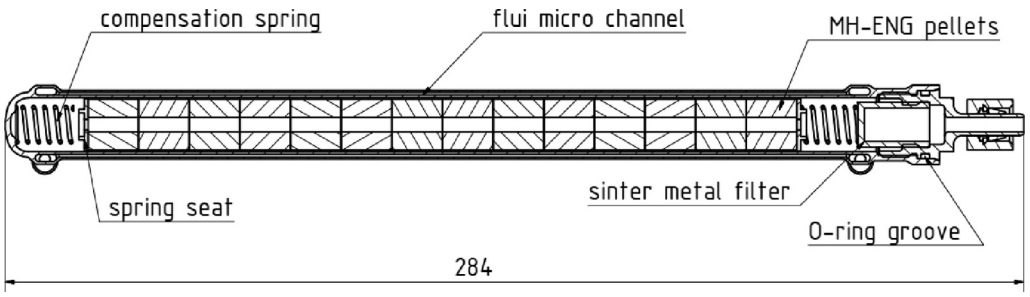

Fig. 5. Sectional view of one reactor tube (dimensions in mm).

Table 2
Design evaluation parameters of this study in comparison to the best reactor in literature.

	Reactor 2.0 from this work	Reactor 1.0 [9]
k_C [−]	2.2 (1.6 w/o fittings)	3.2
$k = m_R/m_{MH}$ [−]	1.5 (0.9 w/o fittings)	3.2
$\Delta T_{MH}/\dot{q}$ [K W^{-1} cm^3]	1.4	1.5
▪ λ [W m^{-1} K^{-1}]	10 [25]	1
▪ α [W m^{-2} K^{-1}]	4500	700
▪ L_{ht} [mm]	5.50	0.88
Bi [−]	3.4	0.6
$\Delta p_{MH}/(\dot{m}\ V)$ [bar g$_{H2}^{-1}$ s cm^3)] *	1.0	10.5
▪ κ [m^2]	1.5e-15	1e-12
▪ L_{mt} [mm]	5.5	279

* at SDR = 7.5 g min^{-1} kg$_{MH}^{-1}$, p_{des} = 10 bar and T_{MH} = 20 °C.

set hydrogen desorption rate $\dot{m}_{H_2,des}$, according to Eq. (7), to achieve a temperature difference $\Delta T_{HTF} = 3$ K between the inlet and outlet of the reactor in steady-state. The variables c_{HTF} and ρ_{HTF} in this equation represent the specific heat capacity and density of the HTF, respectively.

$$\dot{V}_{HTF} = \frac{\dot{m}_{H_2,des}\ \Delta H_{R,des} \Big/ M_{H_2}}{c_{HTF}\ \rho_{HTF}\ \Delta T_{HTF}} \tag{7}$$

The flow rate of HTF is measured in the hot fluid loop with an impeller-type flowmeter that provides the volume flow rate as output. In the cold fluid loop the mass flow is measured directly with a more precise Coriolis-type flowmeter, since the results in this study in terms of thermal power and efficiency are referred to the cold side. The HTF temperature was measured with resistive temperature sensors of type PT100 with their tips pointing in flow direction. The thermal power transferred from the reactor to the HTF is deduced in a caloric way, according to Eq. (8), as the temperature difference over the reactor multiplied with the HTF mass flow $\dot{m}_{HTF}$ and its specific heat capacity, that is considered to be constant in the applied temperature range.

$$\dot{Q}_{HTF} = \dot{m}_{HTF}\ c_{HTF}\ \Delta T_{HTF} \tag{8}$$

On the hydrogen side the gas connectors of both tubes of the reactor are connected and used for both, the inflow and outflow of hydrogen, cf. Fig. 6. Both MFCs act also as a hydrogen gas flow measurement unit. The gas pressure is measured in the connection piping between the inflow MFC, the reactor and the outflow MFC. The conversion of reaction during the absorption and desorption is calculated according to Eq. (9) by integrating the mass flow signal and considering the stored amount of gaseous hydrogen in the void volume V_{void} between the inflow and outflow MFC.

$$\Delta w = \frac{\Delta m_{H_2,abs/des}}{m_{MH}} = \int \dot{m}_{H_2}\, dt - \frac{\Delta p\ V_{void}}{R/M_{H_2}\ T} \tag{9}$$

The void volume was determined to 87.5 mL with a standard deviation of the mean value of 0.4 mL using Argon as an inert gas to prevent reaction in this measurement.

Mixing, pressing and storing of the MH-ENG-composites was conducted at the Fraunhofer Institute for Manufacturing Technology and Advanced Materials (IFAM) under an Argon atmosphere while filling the reactor was performed at atmospheric air. The MH was then activated inside the final setup using 10 cycles with a controlled ramp-up of 1 l$_{std}$/min to the operation pressure of 70 bar at a low temperature of 0 °C. The hold time at 70 bar was between 15 min and 3 h and two times approximately 15 h. Between the absorptions, vacuum was applied at approximately 95 °C with hold times between 30 min and 2 h.

The performance of the reactor 2.0 in terms of specific thermal power and cooling efficiency is evaluated at a constant operation point, that is defined as the operation at constant inlet temperatures for the hot and cold side respectively and at a constant hydrogen flow rate for the desorbing reactor. Each measurement for one operation point consists of

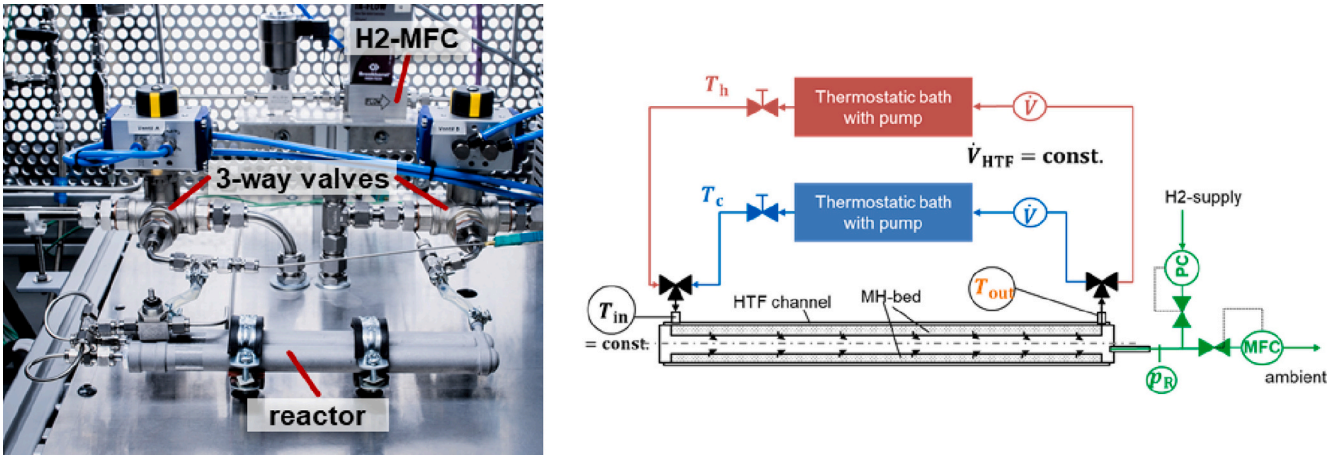

Fig. 6. Experimental setup: picture from the lab (left) and complete schematic view (right).

9 consecutive cycles, as depicted in Fig. 7 to proof the operation to be quasi-steady-state in terms of half cycles times and to have statistically more reliable results. For each desorption half cycle the mean cooling power from the temporal evolution is considered. Subsequently, the mean value of the 9 half cycle means is determined to deduce one resulting value per operation point. In order to deduce the specific thermal power, this value is divided by two times the applied mass of MH, considering the need for two reactors in a final system. To determine the cooling efficiency, the calculated cooling power is divided by the reaction enthalpy and the mean hydrogen mass flow according to Eq. (2).

Fig. 7 shows exemplarily the temporal curves for one experiment at a quasi-steady-state operation point. Each experiment starts with a fully absorbed reactor at 70 bar and at the high temperature level T_h. Then the first desorption is initialized by simultaneously switching both HTF valves to the cold fluid loop, while closing the hydrogen inflow MFC and setting the outflow MFC to the set value. The desorption at constant outflow rate is kept until the hydrogen pressure reaches the desorption end pressure of 10 bar, cf. Fig. 7. This acts as the switching criteria for the half-cycle switching in order to ensure proper operation of a downstream arranged hydrogen consumer on its required pressure level. After reaching the switching criteria the fluid valves are switched to start the absorption half cycle. Accordingly, the outflow MFC for hydrogen is closed and the inflow MFC is opened with a delay of several seconds (specified as a constant time for each experiment). The inflow MF is set to its maximum of 50 l_{std}/min, that fully opens the connection to the pressure reducer. In contrast to the desorption, the absorption therefore occurs at a constant pressure. It is maintained for the same duration as the previous desorption in order to simulate the actual operation of two reactors by the use of just on reactor. After the absorption, the desorption starts again in the way as described before.

As already demonstrated in studies of reactor 1.0 [9] the cooling output can be increased significantly by switching the outlet HTF valves a short time later than the inlet valves. They are actuated only then, when the outlet HTF temperature of the desorbing reactor falls below the outlet temperature of the absorbing reactor. For the same time the hydrogen inlet is closed to prevent heat input from the exothermic absorption in this short intermediate phase. This procedure, denoted as shifted valve switching (TSVS), reduces the sensible heat loss at the switching between the two half cycles. A more detailed description can be found in [9] along with a schematic figure of the HTF paths in the different valve states.

Due to the experimental concept in this study of using just one reactor, the operation strategy of TSVS could not be applied one by one. Instead the TSVS is considered just virtually during the data evaluation. Thereto, the identical reactor in its subsequent absorption half cycle is considered as the second reactor. The thermal power with TSVS applied is then calculated by shifting the corresponding HTF temperature curves backwards by half a cycle, as Fig. 8 exemplarily shows. The bright green and red curves in Fig. 8 show the resulting HTF outlet temperature curves if TSVS is considered in the evaluation.

4. Results

Using the test setup described above, the new reactor presented in this work is characterized to evaluate its performance in terms of specific cooling power and cooling efficiency at different operation conditions regarding temperatures and hydrogen mass flow. Subsequently, the results are compared with the ones of the first prototype - reactor 1.0 - from the studies of Weckerle et al. [9,13].

For each applied set of hot and cold side temperature, different desorption mass flow rates are investigated. The desorption mass flow is considered herein as a specific value normalized against the mass of MH in the reactor, according to Eq. (10). It is denoted as Specific Discharge Rate (SDR) and thus describes how fast the desorbing reactor is discharged.

$$\mathrm{SDR} = \frac{\dot{m}_{H_2}}{m_{MH}} \tag{10}$$

For a given reactor size the SDR is linearly dependent on the power of the subsequently mounted FC, cf. Fig. 1, that is supplied by the desorbed hydrogen. The SDR would be proportional to the half cycle time, if full

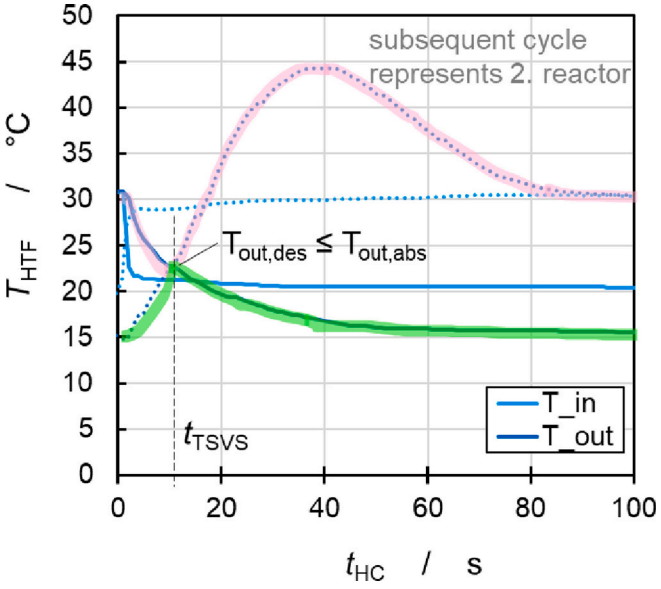

Fig. 8. Imitation of TSVS-operation: Inlet and outlet temperature for the desorption HC (solid line) and the subsequent absorption HC (dotted line) (Exemplarily for 20 °C | 30 °C, 70 bar | 10 bar, 16 l_{std} min^{-1}).

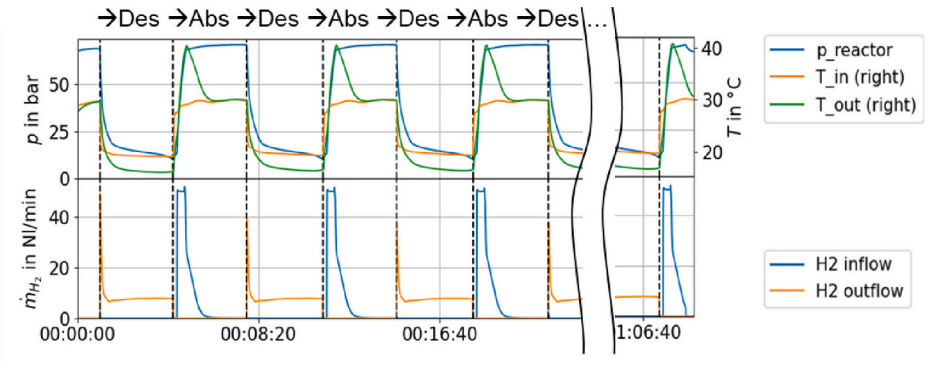

Fig. 7. Reactor operation in subsequent absorption (Abs) and desorption (Des) half cycles.

conversion would be reached for all applied SDRs, and is proportional to the volumetric heat source or sink in the MH bed inside the reactor. Furthermore, an analogy can be drawn to the C-rate of batteries, in which the discharge current is normalized against the battery capacity [17]. Thus, the following results for the specific cooling power, the cooling efficiency and the reaction conversion in Fig. 9, Fig. 10 and Fig. 11 are all plotted against the SDR for different temperature sets. Each experimental point represents the mean of 9 cycles at a quasi-steady-state operation point, evaluated according to the procedure described above. The corresponding error bars show the maximum and minimum occurring in the 9 subsequent half cycles. They are depicted instead of the combined uncertainty of the sensors as the deviation between them represents the higher uncertainty.

For each temperature set corresponding simulation results obtained with a lumped model, that was used in the design process, are additionally shown as dashed lines. A detailed description of the model as well as a complete list of the corresponding parameters for reactor 1.0 can be found in a previous study [16]. The model parameters for the current reactor are based on the results from the design evaluation, consolidated in Table 2. Supplementary parameters are given in Table 3 in the appendix.

4.1. General characteristics

In an ideal edge case, full conversion is reached for any SDR, according to Eq. (6). Here, the specific cooling power could be linearly increased by applying higher SDRs. This theoretical line is shown in Fig. 9 (grey line) as the maximum specific cooling power $\dot{q}_{c,limit}$. It is defined as the maximum considering no losses, especially not the dominating losses due to incomplete reaction from heat and mass transport limitation and due to cooling down the reactor mass itself. Therefore, it can be calculated by the reaction enthalpy multiplied with the SDR, regardless of the applied temperatures and also regardless of the applied reactor design. In a real system, however, the conversion rate decreases at higher SDRs, cf. Fig. 11, that consequently leads to the occurrence of a maximum at an optimal SDR, after that the specific cooling power decreases again. The model results in Fig. 9 illustrate this characteristic curve for the specific cooling power more clearly. The cooling efficiency in Fig. 10 for an ideal system would be maintained at a value of 100 % over all SDRs. For a real system, in contrast, the cooling efficiency starts at an initial value below 100 % due to sensible losses and then decreases further due to the decreasing conversion. Likewise, in Fig. 11 the curve for the conversion in an ideal system would maintain its initial value, that is determined by the used material and applied pressure and temperature boundaries. In a real system, however, it decreases due to heat and mass transport limitation.

4.2. Reference conditions of 20|30 °C

As the first temperature set, 20|30 °C ($T_c|T_h$) was chosen, since this temperature set represents the reference case for reactor 1.0 with the most reported measurement points. According to Fig. 9, for this experiment (green), the new reactor (left) at the lowest measured SDR of 4.2 $g_{H2}\ min^{-1}\ kg_{MH}^{-1}$ shows a specific thermal power of 276 W kg_{MH}^{-1}, that is the same as the maximum for reactor 1.0. However, further increasing the SDR leads to a decline of the specific cooling power for reactor 1.0, which has already passed its maximum, whereas the new reactor reaches higher specific cooling powers. Comparing the maximum of 522 W kg_{MH}^{-1} for reactor 2.0 with the maximum from reactor 1.0, it can be seen that the specific cooling power with the new design is almost doubled.

Looking at the results in the cooling efficiency η_c for the reference experiments (green) in Fig. 10, reactor 2.0 shows 51 % at the maximum specific cooling power, whereas reactor 1.0 shows a higher value of 59 % at its maximum. However, for the new reactor the cooling efficiency can be increased by lowering the SDR. For example, an SDR of 7.8 $g_{H2}\ min^{-1}\ kg_{MH}^{-1}$ leads to a similar efficiency of 61 % but still at a much higher specific cooling power of 448 W kg_{MH}^{-1} compared to reactor 1.0.

To evaluate the performance of the new reactor at an elevated temperature lift of 20 K, Fig. 9 and Fig. 10 also show the results of the following temperature sets of 10|30 °C (blue) and 20|40 °C (red), that are close to the temperature sets of 13|30 °C and 20|42 °C from reactor 1.0. Additionally, the temperature set of 15|35 °C (turquoise) was applied as a condition with also a doubled temperature lift compared to the reference case, but symmetrically around the mid temperature of 25 °C.

4.3. Decreased cold side temperature

The results for reactor 2.0 at the lower cold side temperature of 10 °C (blue curve) show a maximum specific cooling power of 198 W kg_{MH}^{-1} for

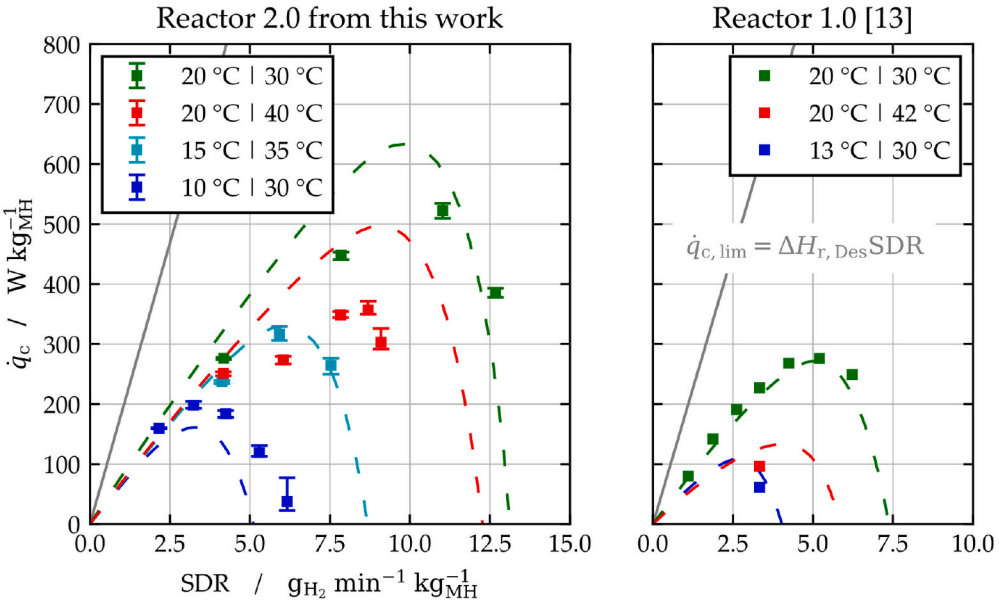

Fig. 9. Specific cooling power of the new design (left) compared to the previous design (right) for different cold and hot side temperatures (T_c | T_h).

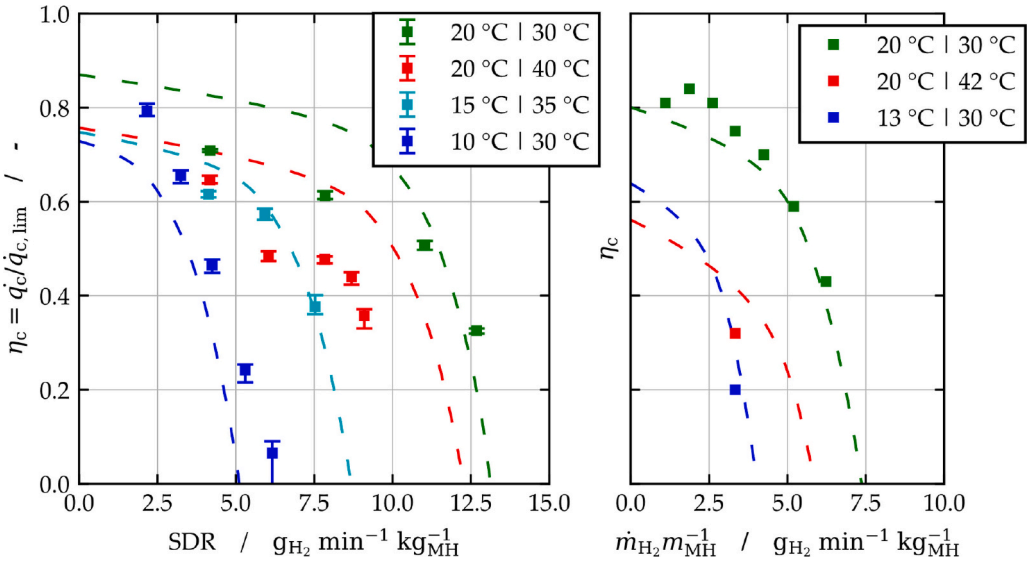

Fig. 10. Cooling efficiency of the new design (left) compared to the previous design (right) for different cold and hot side temperatures (T_c | T_h).

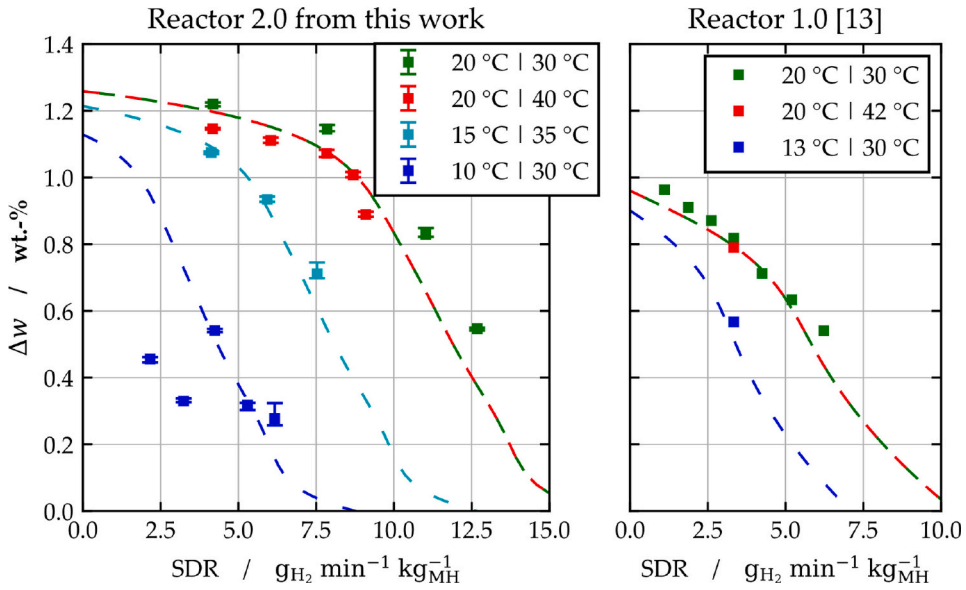

Fig. 11. Reaction conversion of the new design (left) compared to the previous design (right) for different cold and hot side temperatures (T_c | T_h).

an SDR of 3.2 g_{H2} min^{-1} kg_{MH}. The maximum for reactor 2.0 at this temperature set is more than three times higher than 61 W kg_{MH}^{-1} for reactor 1.0. Although for reactor 1.0 this value represents the only data point at this temperature set and is likely not at the optimum SDR, also the maximum from the corresponding model curve of 108 W kg_{MH}^{-1} would be still approximately just half the measured maximum for the current reactor.

For the cooling efficiency at the temperature set of 10|30 °C, cf. Fig. 10, reactor 2.0 reaches a value of 66 % at maximum power that is significantly higher than the value of 20 % for reactor 1.0 and also significantly higher as corresponding model curve for reactor 1.0 predicts.

4.4. Increased hot side temperature

The next experiment at a temperature set of 20|40 °C (red curve) presents also a higher temperature lift of 20 K but by a higher applied hot side temperature, whereas the cold side temperature remains the same as for the reference case. For this temperature set, the maximum measured power is 349 W kg_{MH}^{-1}, cf. Fig. 9, that is more than three times the respective maximum of reactor 1.0. As with the 10|30 °C-set, here only one measurement point for reactor 1.0 is available showing 96 W kg_{MH}^{-1}. The corresponding model curve shows only a slightly higher maximum at 134 W kg_{MH}^{-1} that is still lower than a half of the new reactor. The cooling efficiency at the maximum power is 44 % whereas reactor 1.0 shows 32 %, cf. Fig. 10.

4.5. Symmetrically increased temperature lift

For the additional investigated temperature set of 15 °C cold and 35 °C hot side temperature (turquoise), three operation points at different SDRs were measured. They reveal the occurrence of a maximum specific cooling power of 317 W kg_{MH}^{-1} at an SDR of 5.9 g_{H2} min^{-1} kg_{MH} with a cooling efficiency of 57 %. Comparing this results with the ones of reactor 1.0 at its reference case of 20|30 °C, the new reactor exhibits a similar specific cooling power and efficiency but for a

doubled temperature lift. Moreover, for this temperature set the model represents the measured maximum specific cooling power with the highest accuracy within the measurements of 4 %.

5. Discussion

Having a look at the three model curves of reactor 2.0 with an elevated temperature lift of 20 K, it is apparent that the curve for the highest cold side temperature of 20 °C exhibits the highest specific cooling power and efficiency followed by the one with 15 °C and then 10 °C cold side temperature. Although all three temperature sets have the same temperature lift and therefore the same sensible switching losses. It can be explained by the predominating second effect: Because of the lower cold side temperatures of 10 and 15 °C compared to the 20 °C curve, the desorption at these temperatures is closer to the equilibrium. This leads to an earlier declining curve for the reaction conversion at the cooling half cycle as seen in Fig. 11 and therefore to a reduced heat/cold of reaction per half cycle, whereas the sensible switching losses remain the same.

The superior performance of reactor 2.0 compared to reactor 1.0 can be explained by the improved heat and mass transport capability and the structural heat capacity. At first, the improved heat transport capability leads to a higher possible SDR until the drop of the curve for the conversion occurs, cf. Fig. 11. The later this decrease occurs, the higher the specific cooling power, that can be reached. A declining curve for the conversion with an increasing SDR, as it is apparent in Fig. 11, is well known in literature [17]. For hydrogen storage reactors it describes the depth of discharge at different SDRs. It is caused by an increased temperature difference from the reaction bed to the HTF as a result of a higher heat sink at an increased SDR. This leads, in case of a constant HTF temperature, to a colder temperature inside the reaction bed and therefore to smaller distance to the equilibrium. Therefore, for increased SDRs the full conversion is not reachable anymore. However, with an improved heat transport capability the drop of the curve for the conversion occurs later at higher SDRs, as Fig. 11indicates for the comparison of Reactor 1.0 and 2.0.

The higher possible SDRs of reactor 2.0 for the same conversion than reactor 1.0 can also be explained by a higher mass transport capability. Similarly to the temperature difference between the reaction bed and the outer HTF, there is also a pressure difference between the reaction bed and the free gas volume of the reactor, that increases with an increased SDR. Accordingly, in the case of a better mass transport, the final desorption pressure (set to 10 bar in this study) is only reached at higher SDRs.

Second, the reduced thermal mass of the current reactor leads directly to reduced sensible heat losses. The effect of the reduced thermal mass ratio compared to the previous reactor design can be seen on the one hand in the result plots for the efficiency in Fig. 10: At SDRs close to zero the decreased efficiency for 20 K temperature lift, compared to 10 K, is not as distinct for reactor 2.0 as for reactor 1.0. On the other hand, the reduction of thermal mass can be seen in the slope of the curve for the specific cooling power. Compared to reactor 1.0 the curves for the specific cooling power exhibit a steeper slope at the corresponding same temperature lift. Likewise, the slope at elevated temperature lifts does not decrease as much as for reactor 1.0. For reference, the highest possible slope is represented by $\dot{q}_{c,limit}$.

6. Summary

In this study, three main performance indicators are identified as development targets for a MH reactor used in an open MHCS: the specific cooling power, the cooling efficiency and the temperature lift. Based on these indicators, specific design requirements are deduced, that are in conflict with each other. The conflicting design requirements are a high heat and mass transport capability on the one hand and at the other hand a low heat capacity ratio of the reactor referred to the incorporated mass of MH. Following these requirements as well as previous modelling results, a new reactor design has been developed. It utilizes the MH as composites mixed with ENG for an improved heat conductivity (appr. 10 $W^{-1}\,m^{-1}\,K^{-1}$) inside the reaction bed, micro fluid channels for an improved outer heat transfer and thin 3D-printed aluminum walls in a tubular geometry to keep the structural heat capacity low. Analytical evaluation reveals a reduced heat and mass transport resistance and a lower heat capacity ratio than other reactor designs for this purpose reported in the literature. Additionally, the maximum operation pressure of 70 bar for the reactor in this study succeeds the design pressures of the comparable reactors and broadens the application field in terms of pressure boundaries. Since the design does not exhaust the possibilities of additive manufacturing, but in principal is based on a tube-bundle concept, it allows to be produced by conventional methods in perspective.

Comprehensive characterization at different hot and cold side temperatures and different SDRs are performed and the results are compared to the first prototype at the same pressure ratio p_{high}/p_{low} of 7. In general, the experiments demonstrate the operation at 10 bar desorption pressure by use of the low-temperature alloy ‘Hydralloy C1’. It enables the utilization of the reactor with FCs that require a higher pressure than 5 bar, that was used in the first prototype studies. The results show an 89 % higher specific cooling power of 522 W kg_{MH}^{-1} compared to reactor 1.0 at the reference temperature set of 20|30 °C (temperature lift of 10 K). At a doubled temperature lift of 20 K, for all three temperature sets 10|30 °C, 13|35 °C and 20|40 °C the new reactor achieves a more than doubled specific cooling power at a higher cooling efficiency than the previous prototype. This higher specific cooling power allows to build a MHCS system that needs less MH material for the same thermal output. At the temperature set of 15|35 °C a specific cooling power of 317 W kg_{MH}^{-1} and efficiency of 57 % is achieved, that is nearly the same as the first prototype reaches at half the temperature lift. This increase of temperature lift at the same power makes it more suitable for mobile application in air-conditionings that often require a higher temperature lift due to limited heat exchangers surfaces.

In summary the experiments proved a high thermal performance that can be explained by the reactor construction itself enabling a high heat and mass transport along with a low reactor heat capacity. With this work a significant improvement in reactor design for the open MCS as air-conditioning system in FC vehicles could be shown. It helps to build a compact, lightweight and cost-efficient MCS that meets basic requirements in a mobile applications.

CRediT authorship contribution statement

Alexander Wimmer: Writing – original draft, Visualization, Validation, Software, Resources, Methodology, Investigation, Formal analysis, Data curation, Conceptualization. **Markus Kordel:** Writing – review & editing. **Marc Linder:** Writing – review & editing. **Inga Bürger:** Writing – review & editing, Supervision, Project administration, Methodology, Funding acquisition, Conceptualization.

Declaration of competing interest

The authors declare that they have no known competing financial interests or personal relationships that could have appeared to influence the work reported in this paper.

Acknowledgments

Discussions with Hanna Lösch and Jonina Felbinger have been appreciated. We would also like to thank Marius Lau from the Fraunhofer Institute for Manufacturing Technology and Advanced Materials (IFAM) for producing the MH-ENG composites.

Appendix A. Appendix

A.1. Model parameters for reactor 2.0

Table 3
Supplementary model parameters to Table 2.

Parameter	Symbol	Value
MH material properties		
absorption reaction enthalpy, J mol^{-1}	$\Delta H_{r,abs}$	17,459
desorption reaction enthalpy, J mol^{-1}	$\Delta H_{r,des}$	22,669
polynomial coefficients of PCI for abs (des), –	c_0	−0.21 (0.28)
	c_1	66.28 (−134.5)
	c_2	−1683.2 (1873.51)
	c_3	−1683.2 (−7044.45)
	c_4	−96,220.69 (13,514.4)
	c_5	253,312 (−14,943.32)
	c_6	−411,912.82 (9646.95)
	c_7	432,855.2 (−3383.56)
	c_8	−295,316.37 (498.63)
	c_9	126,507.35
	c_{10}	−30,941.97
	c_{11}	3297.74
	T_{ref}	308.15 (308.15)
maximum total hydrogen capacity, wt.-%	$w_{max,total}$	1.9
plateau mid hydrogen capacity, wt.-%	w_{mid}	1.1
absorption end hydrogen capacity, wt.-%	$w_{abs,end}$	1.54
kinetic constant, s^{-1}	K_0	190,400
activation energy, J	E_a	5.083*10^{-20}
density of MH, kg m^{-3}	ρ_{MH}	6300
mass specific heat capacity of MH, J kg^{-1} K^{-1}	c_{MH}	500
Reactor properties		
inner radius of MH compact, m	r_i	1.7e-3
outer radius of MH compact, m	r_o	7.5e-3
heat transfer coefficient to HTF for des, W m^{-2} K^{-1}	α_{des}	3000*
Operation conditions		
temperature difference of HTF inlet and outlet, K	$\Delta T_{HTF,ab}$	3
Hydrogen and HTF properties		
dynamic viscosity of hydrogen, Pa s^{-1}	η	9.05*10^{-6}*(T / 293) $^{0.68}$
density of HTF, kg m^{-3}	ρ_{htf}	1082
mass specific heat capacity of the HTF, J kg^{-1} K^{-1}	c_{htf}	3260

* It differs from the theoretical value in Table 2, since it is used as fitting parameter in the comparison with experimental results. The lower is reasonable, since no contact resistance from the MH compacts to the reactor wall and no conductivity resistance through the tube is considered.

Data availability

Data will be made available on request.

References

[1] Terlouw T, Rosa L, Bauer C, McKenna R. Future hydrogen economies imply environmental trade-offs and a supply-demand mismatch. Nat Commun 2024;15:7043. https://doi.org/10.1038/s41467-024-51251-7.

[2] Jensen JO, Vestbø AP, Li Q, Bjerrum NJ. The energy efficiency of onboard hydrogen storage. J Alloys Compd 2007;446-447:723–8. https://doi.org/10.1016/j.jallcom.2007.04.051.

[3] Kölbig M, Weckerle C, Linder M, Bürger I. Review on thermal applications for metal hydrides in fuel cell vehicles: operation modes, recent developments and crucial design aspects. Renew Sust Energ Rev 2022:162. https://doi.org/10.1016/j.rser.2022.112385.

[4] Singer G, Köll R, Aichhorn L, Pertl P, Trattner A. Utilizing hydrogen pressure energy by expansion machines – PEM fuel cells in mobile and other potential applications. Appl Energy 2023;343:121056. https://doi.org/10.1016/j.apenergy.2023.121056.

[5] Linder M, Kulenovic R. An energy-efficient air-conditioning system for hydrogen driven cars. Int J Hydrog Energy 2011;36:3215–21. https://doi.org/10.1016/j.ijhydene.2010.11.101.

[6] Wu S, Feng L, Changizian S, Raeesi M, Aiedi H. Analysis of air conditioning system impact on a fuel cell vehicle performance based on a realistic model under actual urban conditions. Int J Hydrog Energy 2022;47:25899–912. https://doi.org/10.1016/j.ijhydene.2022.02.228.

[7] Muthukumar P, Groll M. Erratum to “metal hydride based heating and cooling systems: a review” [international journal of hydrogen energy (2010) 35: 3817–3831]. Int J Hydrog Energy 2010;35:8816–29. https://doi.org/10.1016/j.ijhydene.2010.04.087.

[8] Park J-G, Han S-C, Jang H-Y, Lee S-M, Lee PS, Lee J-Y. The development of compressor-driven metal hydride heat pump (CDMHHP) system as an air conditioner. Int J Hydrog Energy 2002;27:941–4. https://doi.org/10.1016/S0360-3199(01)00187-2.

[9] Weckerle C, Nasri M, Hegner R, Bürger I, Linder M. A metal hydride air-conditioning system for fuel cell vehicles – functional demonstration. Appl Energy 2020:259. https://doi.org/10.1016/j.apenergy.2019.114187.

[10] Malleswararao K, Dutta P, Murthy SS. Applications of metal hydride based thermal systems: a review. Appl Therm Eng 2022:215. https://doi.org/10.1016/j.applthermaleng.2022.118816.

[11] Hirscher M, Yartys VA, Baricco M, Bellosta von Colbe J, Blanchard D, Bowman RC, et al. Materials for hydrogen-based energy storage – past, recent progress and future outlook. J Alloys Compd 2020;827:153548. https://doi.org/10.1016/j.jallcom.2019.153548.

[12] Lototskyy MV, Yartys VA, Pollet BG, Bowman RC. Metal hydride hydrogen compressors: a review. Int J Hydrog Energy 2014;39:5818–51. https://doi.org/10.1016/j.ijhydene.2014.01.158.

[13] Weckerle C, Nasri M, Hegner R, Linder M, Bürger I. A metal hydride air-conditioning system for fuel cell vehicles – performance investigations. Appl Energy 2019:256. https://doi.org/10.1016/j.apenergy.2019.113957.
[14] Wang G, Yu Y, Liu H, Gong C, Wen S, Wang X, et al. Progress on design and development of polymer electrolyte membrane fuel cell systems for vehicle applications: a review. Fuel Process Technol 2018;179:203–28. https://doi.org/10.1016/j.fuproc.2018.06.013.
[15] Weckerle C, Bürger I, Linder M. Numerical optimization of a plate reactor for a metal hydride open cooling system. Int J Hydrog Energy 2019;44:16862–76. https://doi.org/10.1016/j.ijhydene.2019.04.260.
[16] Wimmer A, Linder M, Bürger I. Lumped model for a quasi-continuously operating open metal hydride heat pump system. Appl Therm Eng 2024:241. https://doi.org/10.1016/j.applthermaleng.2023.122250.
[17] Blinov DV, Borzenko VI, Dunikov DO, Romanov IA. Experimental investigations and a simple balance model of a metal hydride reactor. Int J Hydrog Energy 2014;39:19361–8. https://doi.org/10.1016/j.ijhydene.2014.07.048.
[18] Weckerle C, Bürger I, Linder M. Novel reactor design for metal hydride cooling systems. Int J Hydrog Energy 2017;42:8063–74. https://doi.org/10.1016/j.ijhydene.2017.01.066.
[19] Muthukumar P, Linder M, Mertz R, Laurien E. Measurement of thermodynamic properties of some hydrogen absorbing alloys. Int J Hydrog Energy 2009;34:1873–9. https://doi.org/10.1016/j.ijhydene.2008.12.052.
[20] Skripnyuk VM, Ron M. Hydrogen desorption kinetics in intermetallic compounds C2, C51 and C52 with laves phase structure. Int J Hydrog Energy 2003;28:303–9. https://doi.org/10.1016/S0360-3199(02)00081-2.
[21] Wanner M, Hoffmann G, Groll M. Thermodynamic and Structural Changes of an Ab2-Laves-Phase Alloy (Ti0.98 Zr0.02 V0.43 Fe0.06 Cr0.05 Mn1.52) During Extended Thermal Cycling. In: Saetre TO, editor. Hydrogen Power: Theoretical and Engineering Solutions. Dordrecht: Springer Netherlands 1998:257–62.
[22] Mazzucco A, Voskuilen TG, Waters EL, Pourpoint TL, Rokni M. Heat exchanger selection and design analyses for metal hydride heat pump systems. Int J Hydrog Energy 2016;41:4198–213. https://doi.org/10.1016/j.ijhydene.2016.01.016.
[23] Yang FS, Wang GX, Zhang ZX, Meng XY, Rudolph V. Design of the metal hydride reactors – a review on the key technical issues. Int J Hydrog Energy 2010;35:3832–40. https://doi.org/10.1016/j.ijhydene.2010.01.053.
[24] Zhang XY, Ge YT. Performance analysis of metal hydride heat pump system with CFD modelling development and actual reactor designs. Int J Hydrog Energy 2024;94:1146–59. https://doi.org/10.1016/j.ijhydene.2024.11.204.
[25] Dieterich M, Pohlmann C, Bürger I, Linder M, Röntzsch L. Long-term cycle stability of metal hydride-graphite composites. Int J Hydrog Energy 2015;40:16375–82. https://doi.org/10.1016/j.ijhydene.2015.09.013.
[26] Pohlmann C, Röntzsch L, Heubner F, Weißgärber T, Kieback B. Solid-state hydrogen storage in Hydralloy–graphite composites. J Power Sources 2013;231:97–105. https://doi.org/10.1016/j.jpowsour.2012.12.044.
[27] Suda S, Komazaki Y, Kobayashi N. Effective thermal conductivity of metal hydride beds. Journal of the Less Common Metals 1983;89:317–24. https://doi.org/10.1016/0022-5088(83)90340-5.
[28] Lau M, Ehrensberger O, Weißgärber T, Heubner F. Impact of hydride composite materials on thermochemical hydrogen compression. Int J Hydrog Energy 2024;71:562–70. https://doi.org/10.1016/j.ijhydene.2024.04.229.
[29] Meng X, Wu Z, Bao Z, Yang F, Zhang Z. Performance simulation and experimental confirmation of a mini-channel metal hydrides reactor. Int J Hydrog Energy 2013;38:15242–53. https://doi.org/10.1016/j.ijhydene.2013.09.056.
[30] Wang D, Wang Y, Wang F, Zheng S, Guan S, Zheng L, et al. Optimal design of disc mini-channel metal hydride reactor with high hydrogen storage efficiency. Appl Energy 2022;308:118389. https://doi.org/10.1016/j.apenergy.2021.118389.
[31] Shah RK. Chapter VII - Rectangular ducts. In: London AL, Shah RK, London AL, editors. Laminar flow forced convection in ducts. Academic Press; 1978. p. 196–222.
[32] Urbanczyk R, Peinecke K, Meggouh M, Minne P, Peil S, Bathen D, et al. Design and operation of an aluminium alloy tank using doped Na3AlH6 in kg scale for hydrogen storage. J Power Sources 2016;324:589–97. https://doi.org/10.1016/j.jpowsour.2016.05.102.
[33] Bürger I, Sourmelis Terzopoulos VE, Kretschmer C, Kölbig M, Brack C, Linder M. Lightweight reactor design by additive manufacturing for preheating applications using metal hydrides. Int J Hydrog Energy 2021;46:28686–99. https://doi.org/10.1016/j.ijhydene.2021.06.091.
[34] Lesmana LA, Lu C, Chen F, Aziz M. Triply periodic minimal surface gyroid structure as effective metal hydride hydrogen storage reactor: experimental study. Therm Sci Eng Prog 2023;42:101903. https://doi.org/10.1016/j.tsep.2023.101903.

2.3. Paper III: Prove of technological requirements

After a SCP of >500 W/kg$_{MH}$ has been demonstrated, achieved by a model-based development, a high temperature range was still missing in order to achieve vehicle applicability. This leads to the research question of Paper III:

'What are the influencing factors on the achievable temperature lift of the open MHCS and how can they be addressed appropriately?'

The thermal mass of the reactor is identified as the first influencing factor, as it leads to sensitive losses that increase proportionally with increasing temperature lift. Therefore, a reactor design with a low ratio of the reactor's heat capacity to the heat capacity of the MH material is essential. At the same time, however, good heat and mass transfer must be ensured in order to achieve a high SCP. These objectives were already pursued in Paper II making a suitable reactor available. As a second influencing factor, the pressure ratio as high as possible is identified, which is deduced directly from the equilibrium relationship of MHs (Van't Hoff equation). An increased pressure ratio also increases the usable enthalpy available to the open MHCS. On the other hand, however, this reduces the relative operating time. Therefore, an analytical thermodynamic equation was used to determine how far the pressure ratio can be increased in order to achieve optimum energy utilization. The reactor was then characterized at a pressure ratio of 14, which represents a reasonable value, both from an energetic (47% exergy utilization) and vehicle operation (79% relative utilization time) perspective. It was realized by an inlet pressure for the open MHCS of 70 bar and a final outlet pressure of 5 bar.

The increased pressure ratio allowed the generation of elevated temperature lifts of 30 K (10|40 °C) and 40 K (5|45 °C), at which the reactor was comprehensively characterized. As well as for the lower pressure ration of 7 (Paper II), also for the higher pressure ratio of 14, the experimental results showed a good agreement with the lumped model developed of Paper I. With this experiments an application-realistic temperature lift of 40 K with a still high specific power of 229 W/kg$_{MH}$ could be demonstrated. Therewith, the technological aims of this thesis could be fulfilled by a systematic model-based analysis and design process.

Applied Energy 398 (2025) 126396

Contents lists available at ScienceDirect

Applied Energy

journal homepage: www.elsevier.com/locate/apenergy

Metal hydride-based cooling system for fuel cell electric vehicles: Achieving a temperature lift of 40 K

Alexander Wimmer *, Marc Linder, Inga Bürger

Institute of Engineering Thermodynamics, German Aerospace Center (DLR), Pfaffenwaldring 38-40, 70569 Stuttgart, Germany

HIGHLIGHTS

- Open metal hydride cooling system is an energy-efficient A/C for fuel cell vehicles
- High pressure ratio identified as one enabler for achieving a high temperature lift
- 70 bar absorption and 5 bar desorption pressure applied in experiments
- High-performance reactor achieves 386 W/kg$_{MH}$ at 30 K and 229 W/kg$_{MH}$ at 40 K
- Up-scaling study for lab-scale reactor shows efficiency gain of 5 % on vehicle level

GRAPHICAL ABSTRACT

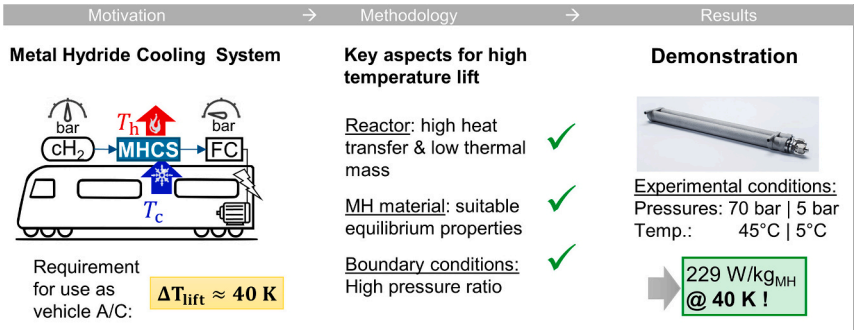

ARTICLE INFO

Keywords:
Mobile application, air-conditioning
Heat pump
Pressure ratio
Energy recovery
Efficiency increase

ABSTRACT

The open metal hydride cooling system (MHCS) is a promising technology to recover compression energy required to fill the pressure tank of a fuel cell electric vehicle. By means of the thermochemical reaction of hydrogen with metal hydrides, the MHCS directly converts the available pressure difference into a heat pump effect to replace the conventional energy-consuming air-conditioning. Previously published studies already demonstrated a high specific power under vehicle-relevant operation. However, only a maximum temperature lift of 20 K was achieved so far, that is considered as too low for application as a vehicle air-conditioner. In order to achieve a high temperature lift, the underlaying thermochemical reaction behavior requires a high pressure ratio. To further reach a high specific power and efficiency at elevated temperature lifts, additionally the applied reactor has to facilitate a high heat transfer and low heat capacity. Thus, in this study experimental investigations using a high pressure ratio of 70 to 5 bar are conducted with a proven reactor-material setup. The comprehensive characterization on different discharge rates show a maximum specific cooling power of 386 W/kg$_{MH}$ at a temperature lift of 30 K and 229 W/kg$_{MH}$ at 40 K, where application-relevant temperatures of 5 °C for the cooling side and 45 °C for rejection side are reached. On the basis of these results a scaling of the lab-scale reactor is calculated revealing a total efficiency improvement on vehicle level in the order of 5 % using the open MHCS.

* Corresponding author.
E-mail address: alexander.wimmer@dlr.de (A. Wimmer).

https://doi.org/10.1016/j.apenergy.2025.126396
Received 13 April 2025; Received in revised form 17 June 2025; Accepted 24 June 2025
Available online 10 July 2025

Nomenclature

c	mass specific heat capacity, $Jkg^{-1}\ K^{-1}$
η_c	cooling efficiency, –
E	energy, J
Ex	exergy, J
ΔH	reaction enthalpy, $Jmol^{-1}$
k	polynomial parameter, –
k_C	Heat capacity ratio of reactor to MH, –
M	molar mass, $kgmol^{-1}$
m	mass, kg
$\dot{m}$	mass flow, kgs^{-1}
p	pressure, Pa
Q	heat, J
$\dot{Q}$	heat flux, W
$\dot{q}$	metal hydride mass specific thermal power, Wkg_{mh}^{-1}
R	universal gas constant, $Jmol^{-1}\ K^{-1}$
R_{H2}	specific gas constant of hydrogen, $Jkg^{-1}\ K^{-1}$
T	temperature, K
ΔT	temperature lift, K
w, Δw	hydrogen capacity, $kg_{H2}\ kg_{mh}^{-1}$

Subscripts

0	standard condition
abs	absorption
amb	ambient
c	cold/cooling
des	desorption
h	hot
H_2	hydrogen
ini	initial
lim	limit
max	maximum
ref	reference
openSys	open system

Abbreviations

0D/1D/2D	zero-, one- or two-dimensional
A/C	air condition
atm	atmosphere
FC	fuel cell
FCEV	fuel cell electric vehicle
HTF	heat transfer fluid
LHV	lower heating value
MFM	mass flow meter
MFC	mass flow controller
MH	metal hydride
MHCS	metal hydride cooling system
PEM	polymer electrolyte membrane
PCI	pressure concentration isotherm
PLC	Programmable logic controller
PRV	pressure reduction valve
R	reactor
SDR	specific discharge rate
TSVS	time shifted valve switching
V	valve
VCS	vapor compression system

1. Introduction

Fuel cell electric vehicles (FCEV) can play a significant role to decarbonize the mobility sector, especially for heavy-duty vehicles like trucks and buses, but also for trains [1]. According to the state of the art, hydrogen in such vehicles is stored as a highly compressed gas in pressurized tanks at 350 or 700 bar [2]. To fill the tank, a remarkable energy input of approximately 15 % of the lower heating value (LHV) is required for compression [3–5] and is not recovered so far. Thus, there is a significant energy potential available to be used onboard. As one promising possibility, metal hydrides (MH) material are known to be able to convert a pressure difference directly into a heat pump effect by a thermochemical gas solid reaction. This principle is used since the first works on metal hydride refrigeration systems in the 1980s [6] and has been further developed [7–13]. However, in the most of these reported machines the pressure difference, needed for the MH to generate the heat pump or cooling effect, is generated also by a second MH material with a slightly different equilibrium behavior and using a heat source as driving force or by an external compressor. It leads to a closed and thermal- or compressor-driven system, which has been extensively investigated in the literature [14–22]. In contrast, an open pressure-driven system is based on an external pressurized hydrogen flow provided for instance by a pressurized gaseous storage. It was first proposed by Linder et al. [10] for use in FCEVs equipped with a high-pressure tank and further reported by studies Meier et al. [23] and Weckerle et al. [24–26] and publications of the authors of this study [27,28]. It is further denoted as open metal hydride cooling system (MHCS). By means of this system, a part of the compression work from the refueling process can be recovered and converted directly into a heat pump effect. From the obtained heat pump effect, the generated cooling power can be used as an energy-efficient air-conditioning (A/C) system, that needs no additional energy from the fuel cell (FC). Therefore, the MHCS could assist or even replace the existing A/C and thus make the FCEV more efficient by diminishing or removing its energy consumption. It leads then to a higher range and lower fuel costs due to a reduced total energy consumption [29].

The working principle of the open MHCS is characterized by two identical MH reactors, that operate counter-cyclically. In the first half-cycle, reactor R1 absorbs hydrogen at a high pressure level, while releasing the heat of reaction to the ambient. The inlet pressure for the open MHCS is on a constant pressure in the range between 30 and 100 bar. This pressure does not equal the actual tank pressure, but is maintained by a subsequent pressure reducer. While reactor R1 absorbs hydrogen from the tank, reactor R2 desorbs hydrogen to the fuel cell, as shown in Fig. 1. Since the inlet pressure of a low-temperature PEM-FC typically used in vehicles is on a significantly lower level (3–12 bar [30]), the desorption reactions takes place on a lower temperature level than the absorption, according to the equilibrium characteristic of the MH-hydrogen reaction. This first half cycle, in which reactor R2 generates cold and R1 releases heat, is shown in Fig. 1. In the second half cycle the reactors are switched, leading reactor R1 to desorb hydrogen

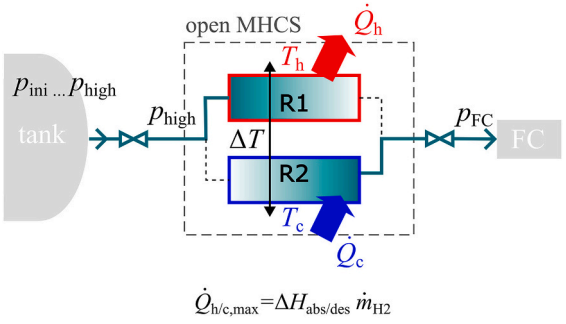

Fig. 1. The open MHCS arranged between a pressure tank and a fuel cell works on the fixed upper pressure level p_{high} and the lower fuel cell pressure p_{FC}.

and to produce cold while reactor R2 is now absorbing and releasing heat. This operation procedure ensures a continuous supply of hydrogen to the FC with a quasi-continuous thermal output.

In the course of the development of the open MHCS as an A/C-system for hydrogen powered vehicles, several research studies have been published so far. Linder et al. [10] identified a suitable MH material and performed first experiments on appropriate pressure levels of 50 bar for absorption and 6 bar for the desorption, resulting in a pressure ratio of 8. A temperature lift of 17 K was achieved at a cold side temperature of 13 °C and a hot side temperature of 30 °C. However, the desorption process was pressure-constrained instead of mass-flow constrained and therefore did not represent the real supply to a FC. Weckerle et al. [24] demonstrated the first operation of an open MHCS on a constant mass-flow with a coupled FC. With a new low-cost reactor filled with another suitable MH material a specific cooling power of 265 W/kg_{MH} was reached, but only at a temperature lift of 10 K [25]. The applied pressure ratio was just slightly decreased to 7 by using 35 bar as the absorption and 5 bar as the desorption pressure. The maximum achieved temperature lift of 22.3 K was also only around 20 K. In previous studies the authors discovered the operation characteristic of an open MHCS on varying discharge rates and presented a novel reactor design specially designed for that application [28]. The new design showed a significantly enhanced specific power of 522 W/kg_{MH} at the same boundary conditions in terms of pressure ratio and temperature lift. However, only the same maximum temperature lift of 20 K was reached.

Thus, it can be concluded, that in the course of the development of the open MHCS, multiple suitable MH materials were identified [10,24], the operation with a coupled FC was demonstrated [24] and a reactor with a high specific power was developed [28]. But only a temperature lift of approximately 20 K for all reported studies was achieved so far. However, typical vehicle A/C systems have an evaporator temperature of approx. 7 °C and a condenser temperature of approx. 45 °C [31]. Hence, reaching a temperature lift of at least 40 K can be seen as the last missing requirement for application suitability. For achieving a high temperature lift, the enabling factors are known from literature. They are at first, a high pressure ratio as it is a direct result of the van't Hoff correlation between reaction temperature and reaction pressure [32]. At second, a material that fits to the available pressure boundaries and intended temperatures [33]. And at third, a reactor facilitating a good heat and mass transport capability with a low heat capacity of its own structure [15].

The work presented herein focuses on two aspects. The first is the experimental demonstration of a high temperature lift for a lab-scale reactor. The second is the question of a proper scale-up of the lab-scale reactor for use in a vehicle. Therefore, the first part presents experimental results of a high-performance reactor, developed in a previous study [28]. It incorporates the metal hydride material $Ti_{0.99}Zr_{0.01}V_{0.43}Fe_{0.09}Cr_{0.05}Mn_{1.5}$ ('Hydralloy C1'), that is suitable for an air-conditioning application in a FCEV, due to its thermodynamic property showing an equilibrium below room temperature at typical FC supply pressures. The experiments are conducted on a pressure ratio of 14, that is significantly higher than in all other studies of an open MHCS aiming for a temperature lift of 40 K. Under this conditions the specific power and cooling efficiency are evaluated, as the relevant performance indicators. The results are used for validating a simplified lumped model as a predesign tool. Additionally, an evaluation of the thermodynamic efficiency is presented. In the second part, the specific characteristic of the lab-scale reactor is used to describe a design procedure for a suitable sizing of the MHCS in a typical vehicle application. It also describes the total achievable efficiency improvement on vehicle level.

2. Methodology

The methodology of achieving a high temperature lift with an open MHCS is described in detail. Section 2.1 describes the selection of an appropriate pressure ratio, in the context of the application in a FCEV, by means of an analysis of the exergy utilization. Section 2.2 describes the applied high-performance reactor and the suitable MH material as the fulfillment of the second precondition besides the high pressure ratio. The test setup with the applied boundary conditions is described in section 2.3. It is followed by a description of the evaluation procedure for determining the power and efficiency characteristics in section 2.4. The methodology part is completed with the presentation of a lumped model in section 2.5 that was used for predesigning the prototype reactor and compared in the results section with the experiments.

2.1. Selection of pressure ratio by exergy utilization

As the pressure ratio plays a significant role for realizing a high temperature lift, it is analyzed how the chosen pressure ratio effects the amount of energy the open MHCS ideally could recover from the pressure tank.

According to the thermodynamic principles, the higher the pressure ratio the higher the usable energetic potential. However, in this context the pressure tank delivers the highest pressure only at the beginning, when the tank is completely full and its pressure is decreasing continuously during discharge until a final residuum pressure is reached. The open MHCS in contrast operates on a fixed upper and lower pressure level, whereby the lower one is determined by the fuel cell inlet pressure, cf. Fig. 1. The upper pressure level, on the other hand, can be set either on a high pressure level close to the initial tank pressure, or on a low level close to the final tank pressure. Due to the fixed upper pressure level, the open MHCS can only operate until the tank reaches this level. A relatively high set upper pressure results into a high pressure ratio and therefore to a high energetic potential. However, only a small amount of the discharged gas flows through the open MHCS can be energetically used. For a relatively low set upper pressure level, the reverse situation occurs. In this regard the question arises, which upper pressure level is the optimum from an energetic point of view in order to use the most of the available energy from the compressed gas. It will be is analyzed in the following.

At first, the available energy of the pressure tank is calculated as the exergy of the contained compressed gas. Considering the tank on ambient temperature T_{amb} and having an initial pressure p_{ini}, it is calculated by an isothermal expansion of a closed system to the ambient pressure p_{amb}. However, most hydrogen pressure tanks for vehicles cannot be discharge completely to ambient pressure during normal operation to allow for a fast refueling process [34]. Instead a residual pressure must remain inside the tank for technical reasons, e.g. 20 bar as specified in the refueling protocol SAE J2601 [35]. Considering a residual pressure p_{empty} inside the empty tank, the exergy is calculated by Eq. (1) assuming an ideal gas. For a 350 bar-tank, 1 bar ambient and 20 bar empty tank pressure the exergy is 5.59 MJ/kg_{H2}, representing 4.7 % of the LHV of the hydrogen (120 MJ/kg).

$$\boldsymbol{Ex} = \boldsymbol{m}_{\mathrm{H_2,tank}} \left(1 - \frac{\boldsymbol{p}_{\mathrm{empty}}}{\boldsymbol{p}_{\mathrm{ini}}}\right) \boldsymbol{T}_{\mathrm{amb}} \boldsymbol{R}_{\mathrm{H_2}} \left(\ln\left(\frac{\boldsymbol{p}_{\mathrm{ini}}}{\boldsymbol{p}_{\mathrm{amb}}}\right) + \frac{\boldsymbol{p}_{\mathrm{amb}}}{\boldsymbol{p}_{\mathrm{ini}}} - 1\right) \tag{1}$$

At second, the maximum usable energy for the open MHCS is calculated. Therefore, only the discharged hydrogen, until the tank pressure equals the upper pressure level p_{high}, must be considered. This usable mass can be calculated by the ideal gas equation leading to Eq. (2):

$$\boldsymbol{m}_{\mathrm{H_2,usable}} = \boldsymbol{m}_{\mathrm{H_2,tank}} \left(1 - \frac{\boldsymbol{p}_{\mathrm{high}}}{\boldsymbol{p}_{\mathrm{ini}}}\right) \tag{2}$$

Considering Eq. (2), the usable energy is then calculated as the isothermal expansion of hydrogen for an ideal open system from p_{high} to p_{low} at ambient temperature. It leads to Eq. (3) assuming an ideal gas.

$$\boldsymbol{E}_{\mathrm{openSys}} = \boldsymbol{m}_{\mathrm{H_2,tank}} \left(1 - \frac{\boldsymbol{p}_{\mathrm{high}}}{\boldsymbol{p}_{\mathrm{ini}}}\right) \boldsymbol{R}_{\mathrm{H_2}} \, \boldsymbol{T}_{\mathrm{amb}} \ln\left(\frac{\boldsymbol{p}_{\mathrm{high}}}{\boldsymbol{p}_{\mathrm{low}}}\right) \tag{3}$$

This energy is referred to the total exergy of a 350 bar-tank and visualized in Fig. 2. It shows the usable energy potential as a function of the set upper pressure level of the open system for different FC pressures.

It reveals a maximum exergy utilization of 74 % for a fuel cell pressure of 1 bar and a decreased maximum of 33 % for a fuel cell pressure of 12.5 bar. The corresponding optimal upper pressure levels are 67 bar for a fuel cell pressure of 1 bar and 110 bar for a fuel cell pressure of 12.5 bar, respectively. The occurrence of a maximum can be explained by two opposing effects: Increasing the upper pressure level p_{high} on the one hand increases the energy per mass of hydrogen an open system can convert, represented in Eq. (3) by the term $R_{H_2}\, T_{amb}\, \ln\left(p_{high}/p_{low}\right)$. On the other hand, an increased upper pressure level reduces the usable amount of hydrogen according to Eq. (2), until the tank pressure reaches p_{high} during discharging.

The selection of the upper pressure level for the open MHCS does not only determine the exergy utilization but also determines how long the system can be used with respect to the total operation time of the FCEV. Therefore, a second y axis is added in Fig. 2, that shows the relative utilization time. It equals the relative usable mass of hydrogen and thus is calculated by Eq. (4).

$$\frac{m_{usable,openSys}}{m_{usable,total}} = \frac{p_{ini} - p_{high}}{p_{ini} - p_{empty}} \tag{4}$$

In this regard Fig. 2 shows for instance for 1 bar FC pressure that the open MHCS can operate for 86 % of the time until the tank is empty at 20 bar, if the upper pressure level is set on the energetical optimum. Selecting an upper pressure level for the open MHCS that is lower than the optimum, the exergy utilization decreases, but the coverage of the operation can be increased. Therefore, as part of a preliminary design choice, one has to find a compromise in the pressure range between the optimum pressure, which exhibits the best exergy potential, and the lower pressure limit p_{emtpy} which leads to 100 % utilization time.

From a MH reaction point of view, a high exergy utilization does not allow to generate more cold or to pump more heat per hydrogen mass flow, since this is determined by the reaction enthalpy ΔH_R of the MH material. Instead, an increased pressure ratio will allow a higher temperature lift for the same specific cooling power, or a higher specific cooling power for the same temperature lift. Both aspects will be addressed in the experimental part of this work.

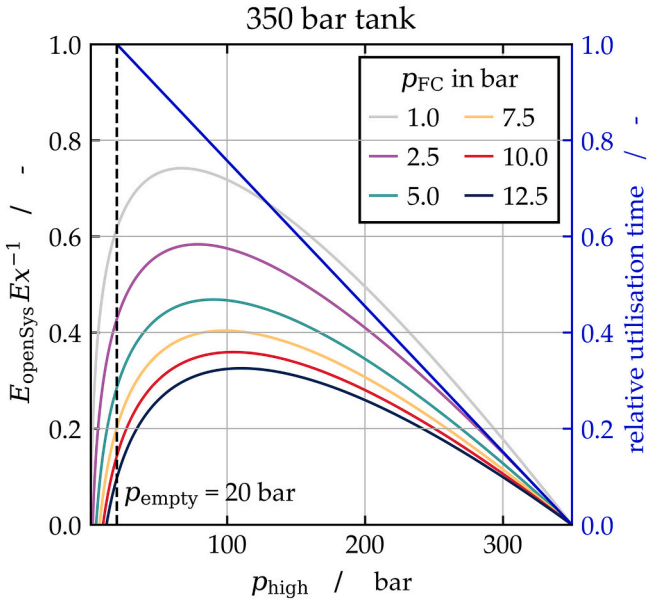

Fig. 2. Energy potential of an open system that works between p_{high} and p_{FC} in relation to the total exergy of a 350 bar-tank. In addition, the blue line shows the operation time of an open system until the tank pressure reaches p_{high} in relation to the total time of tank discharging, that is considered empty at 20 bar. (For interpretation of the references to colour in this figure legend, the reader is referred to the web version of this article.)

2.2. Description of the reactor prototype

The MH reactor used in this work has already been presented in detail in [28] and is therefore only briefly described here in its main features. Its design aims especially on a good heat and mass transport with a low structural heat capacity at the same time. It shows a functional integrated design completely out of thin-walled aluminum. The concept is based on a tube bundle in a simple version with two connected tubes, each with an outer diameter of 19 mm, cf. Fig. 3. Therefore, it is scalable in length and in number of parallel tubes, forming a kind of tube bundle reactor in a scaled-up version. As the MH material, the interstitial AB_2-based material $Ti_{0.99}Zr_{0.01}V_{0.43}Fe_{0.09}Cr_{0.05}Mn_{1.5}$ is utilized. It is also known under its brand name 'Hydralloy C1' from the manufacturer Gfe (Gesellschaft für Elektrometallurgie mbH) and represents a commercially available material, which can easily be obtained in the lower two-digit kilogram range needed for use in the end application in vehicles. It features a maximum hydrogen capacity of appr. 1.75 wt.-% and is highly cyclic stable. As a low temperature MH, it is suitable in principle for cooling purposes in a FCEV. At a desorption pressure of 5 bar, which is typical for the FC supply, it shows an equilibrium temperature of −16 °C at the plateau mid. This allows still a high power even at low cooling temperatures (5–10 °C), as there is a high distance to the equilibrium. On the absorption side, a pressure of a least 70 bar is required to fully absorb hydrogen at 45 °C. The MH material is not used as a loose powder, but mixed with graphite and then compacted to pellets, in order to realize a high heat conductivity inside the reaction bed. The stacked ring-shaped pellets form an inner hydrogen distribution channel inside the reactor tube to realize a high axial mass transport. The heat transfer is provided via a heat transfer fluid (HTF), that flows inside the reactor wall through micro channels with a diameter of 0.7 mm. They are produced in the course of the additive manufacturing of the entire reactor. The reactor is filled with 178 g of MH. Its lightweight design leads to a low heat capacity ratio of reactor structure related to MH material of 2.4 with and 1.7 without considering the hydrogen connection fittings. A low heat capacity ratio is important to reduce the sensible heating losses, that occur due to the alternating switching between hot and cold side and therefore essential to achieve a high temperature lift. Additionally, it is also important to keep the temperature difference between HTF and reaction bed low, to achieve a high net temperature hub. In this regard the reactor features a high heat transport capability in terms of temperature difference per heat source power of 1.4 K W^{-1} cm^3.

2.3. Test setup

The test setup for characterizing the reactor in the quasi-continuous operation procedure of an open MHCS is schematically shown in Fig. 4. A photographic representation of the test rig can be found in a previous publication in which the same setup was used [28]. The test setup consists of two domains, the hydrogen gas side and the thermal side with two HTF loops. The Hydrogen side simulates the integration of the open MHCS in the hydrogen path between tank and FC. The gas supply from the laboratory provides 150 bar and is further reduced by a pressure reduction valve to a fixed pressure of 70 bar. The pressure reduction valve is followed by a mass flow meter and a blocking valve. The outlet of hydrogen to the ambient is routed via a mass flow controller. Between the gas inlet from the supply line and the outlet to the ambient, the reactor is connected via a cross type fitting that also connects a pressure sensor to monitor the reactor pressure during the half cycles. The half cycle operation is controlled by a programmable logic controller (PLC). In the absorption half cycle, it sets the outlet mass flow controller to zero and opens the inflow blocking valve. In the desorption half cycle, it

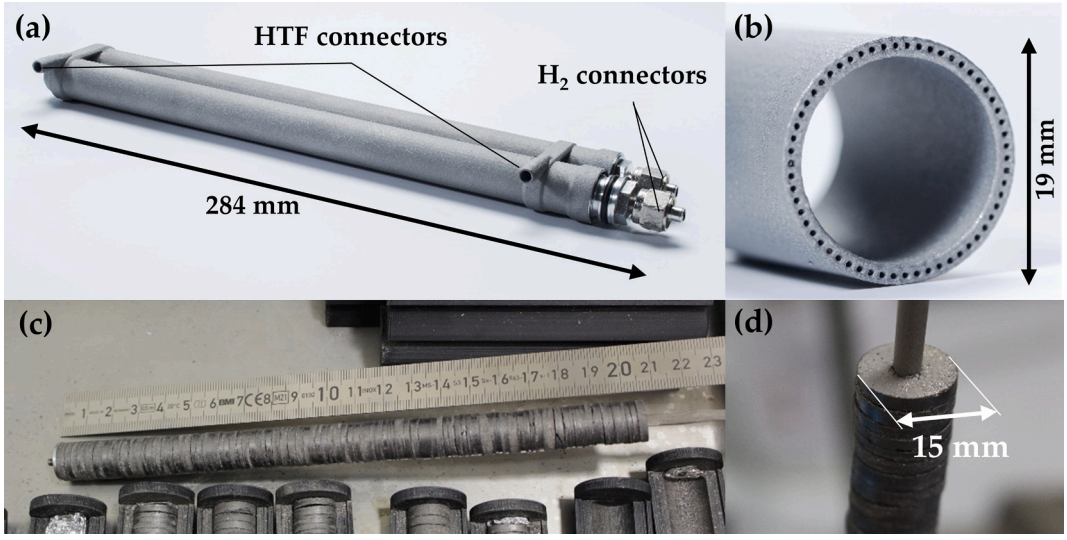

Fig. 3. Additive manufactured reactor prototype made of aluminum with caps (a), cross section of single tube wall with integrated micro channels (b), stacked metal hydride grahite pellets before insertion and (c) detailed view of pellet with central filter mesh (d).

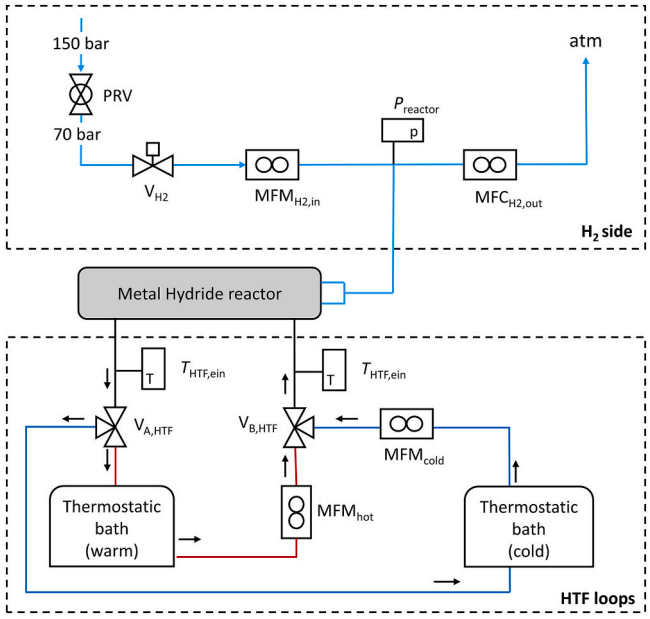

Fig. 4. Schematic of test setup showing the reactor arranged between the hydrogen side on the top and heat transfer fluid (HTF) side on the bottom.

closes the inflow blocking valve and sets the outlet flow controller to a defined value. The flow controller maintains the constant hydrogen mass flow while the pressure of the reactor is decreasing from the initial 70 bar to the final pressure of 5 bar. When the pressure reaches 5 bar, the desorption half cycle ends and the absorptions half cycle starts again. The absorption on a constant pressure is hold for the same duration as the previous desorption took. This allows to simulate the real operation with two reactors by use of only one reactor.

From an energetic point of view, according to the exergy analysis in Sec. 2.1, the optimal upper pressure for the chosen FC inlet pressure of 5 bar would be 90 bar instead of 70 bar. It would lead to an exergy utilization of 47 % and a relative utilization time of 79 %. For the chosen pressure of 70 bar, however, the exergy utilization decreases only slightly to 46 %, but the utilization time increases to 85 %. It shows therefore a good compromise between energetic potential and utilization time.

In the thermal domain of the test setup, two thermostatic baths with internal pumps and external flow meters are arranged in order to take up the absorption heat and desorption cold, respectively. They simulate the heat exchangers to the ambient and vehicle cabin by providing constant inlet temperatures for the hot and cold side. The thermal power of the reactor is measured via the temperature difference between HTF inlet and outlet, the HTF flow and its heat capacity. The HTF flow is set depending on the applied hydrogen mass flow in order to achieve a constant temperature difference between inlet and outlet of 3 K in the steady state phase after the initial cool-down phase at each half cycle. Two three-way-valves at the HTF inlet and outlet of the reactor are controlled by the PLC and connect the reactor either with the hot or cold fluid loop depending on the active half cycle.

2.4. Evaluation of performance

For the evaluation of the thermal performance in the experiments, three main performance indicators can be used, according to [28]. One of these is found to be the temperature lift itself, that shows the grade of the thermal output. On a certain temperature set, two additional performance indicators can be evaluated. The first is the specific cooling power related to the applied mass of MH, cf. Eq. (5). It determines the necessary mass of MH for a certain cooling power and therefore the total mass and size of the open MHCS in an application. Especially for a vehicle integration, a high specific power is important.

$$\dot{q}_c = \frac{\dot{Q}_c}{m_{MH}} \tag{5}$$

The second important performance indicator is the cooling efficiency, introduced by Weckerle et al. It is defined as the actual cooling power divided by the material limited cooling power, that is determined by the desorption enthalpy ΔH_{des} of the material multiplied with the hydrogen flow rate. The cooling efficiency defined in Eq. (6) is therefore explicitly not a thermodynamic efficiency, but a material related one.

$$\eta_c = \frac{\dot{Q}_c}{\Delta H_{des}\, \dot{m}_{H_2}} \tag{6}$$

The temporal course of the thermal output is not constant during the desorption half cycle, due to the temperature change at the beginning. Therefore, for calculating the cooling efficiency as well as the specific cooling power, the mean value over the half cycle is considered.

Previous studies showed that on a fixed temperature set the resulting

cooling power and cooling efficiency depend on the discharge mass flow leading to a characteristic curve. In this regard the specific discharge rate (SDR) was introduced as a parameter that denotes the constant hydrogen flow rate at the desorption half cycle normalized by the used mass of MH, cf. Eq. (12). It is a measure of the forced reaction rate, if a neglectable free gas volume inside the reactor is assumed. In a real system with a fixed reactor size the SDR is proportional to the FC power.

$$\mathbf{SDR} := \frac{\dot{m}_{H_2}}{m_{MH}} \tag{7}$$

An optimized valve control strategy was introduced by Weckerle et al., that reduces the switching losses and hence increases the average thermal output. It is based on a time shifted valve switching (TSVS) of the HTF outlet valve compared to the inlet valve. To reproduce this strategy in a single-reactor test setup, the TSVS is considered only in the postprocessing during the data evaluation. Thereto, from the half cycle start to the time of the delayed valve switching, the HTF outlet temperature from the subsequent absorption half cycle is used instead of the current one. The subsequent absorption cycle from the same reactor thus simulates the parallel absorbing reactor in a normal two-reactor configuration. The point of the delayed valve switching is determined herein, when the outlet temperature of the current desorption half cycle equals the outlet temperature of the subsequent absorption half cycle.

2.5. Lumped model

The following briefly describes a model, previously introduced in [27], that is parametrized for the current reactor and that is validated with additional experimental data from this study. This lumped model is based on a steady state approach and considers the energy balance for a half cycle. It is obtained by two subsequent simplification steps in the spatial domain, shown in Fig. 5 (a). In a first step the 3D reactor model is simplified to a 2D representation of the half of the cross plane, cf. Fig. 5 (b), since the reactor tube is assumed to be ideal rotational symmetric. In a second step only the predominating radial effects are considered, leading to a 1D profile for the temperature and pressure across the reaction bed. Therefrom a mean temperature difference can be deduced linking the mean HTF temperature with the 0D representation for the lumped MH mass, where the kinetic equation is applied on, cf. Fig. 5 (c).

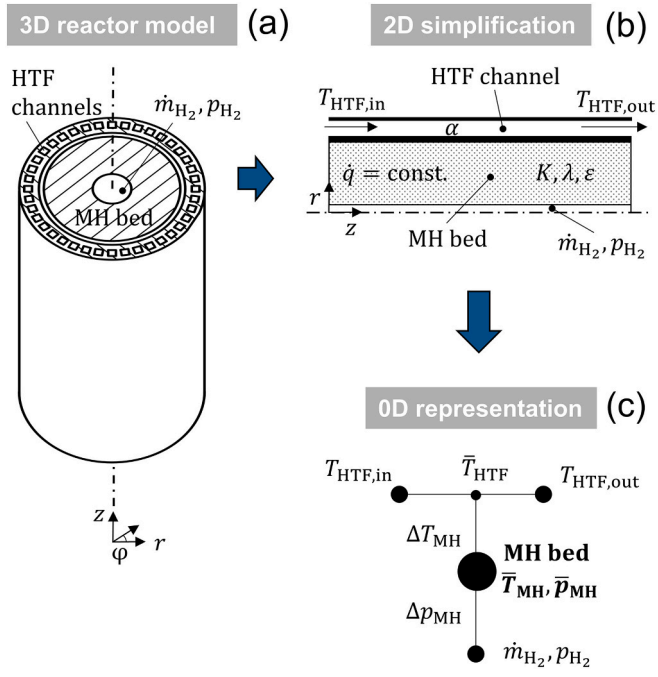

Fig. 5. Model reduction of MH reactor to lumped mass representation.

The MH material properties are implemented considering the kinetic constants and a hydrogen-concentration dependent function for the reaction equilibrium. Therefore, the measured pressure concentration isotherms (PCI) from literature [10] are fitted with a polynomial function at a reference temperature T_{ref} of 30 °C and are temperature compensated by the van't Hoff equation with the reaction enthalpy ΔH_{abs} for absorption and ΔH_{des} for desorption, as an additional fitting parameter respectively. It leads to Eq. (8), where p_0 denotes the reference pressure of 1.013 bar.

$$\frac{p}{p_0} = \exp\left\{\frac{\Delta H_{abs/des}}{R}\left(\frac{1}{T_{ref}} - \frac{1}{T}\right)\right\}\sum_{i=0}^{n} k_i w^i \tag{8}$$

The parameters k_i of the fitting polynomial are listed in Table 2 in the appendix. The comparison between experimental data and polynomial fit is shown in Fig. 6 for the absorption (abs) as well as for the desorption (des) line.

The polynomial function for the equilibrium pressure is applied on the expression for the reaction kinetics of the lumped MH mass, whereas the temperature and pressure at this mass point are determined by the 1D steady-state temperature and pressure profiles. Using the resulting equation, the reaction conversion is calculated as a function of the applied hydrogen mass flow. In combination with the reaction enthalpy it defines the produced heat of reaction per half cycle. This generated cold is further reduced by the sensible heat, which is required to cool down the reactor from the hot to the cold temperature level. It yields the net thermal cooling power, shown by Eq. (9).

$$\dot{q}_c = \frac{\dot{m}_{H_2}}{m_{MH}}\left(\frac{\Delta H_{des}}{M_{H_2}} - \frac{c_{MH}\,(1 + k_C)}{\Delta w}\,\Delta T_{lift}\right) \tag{9}$$

In the same way the cooling efficiency can be calculated, represented by Eq. (10).

$$\eta_c = 1 - \frac{c_{MH}(1 + k_c)\,\Delta T_{lift}}{\Delta w\,\frac{\Delta H_R}{M_{H_2}}} \tag{10}$$

The parameter k_C in eqs. (9) and (10) denotes the important heat capacity ratio of the reactor structure to the contained MH material, cf. Eq. (11).

$$k_C := \frac{c_{reactor}\,m_{reactor}}{c_{MH}\,m_{MH}} \tag{11}$$

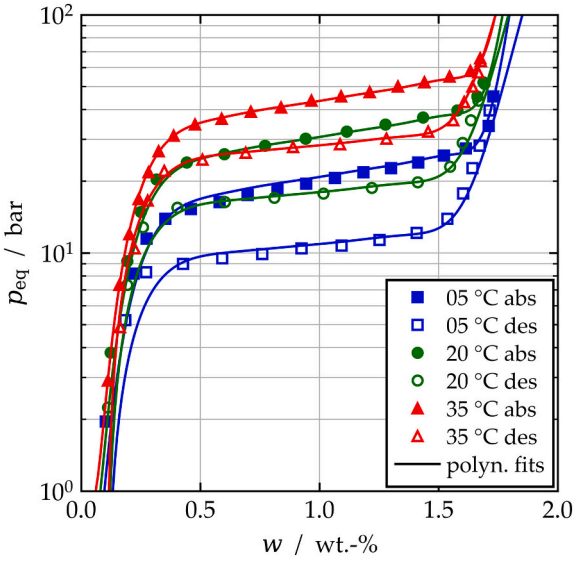

Fig. 6. Polynomial fitting of the experimental PCIs of Hydralloy C1 from [10].

3. Results of characterization

The following presents experimental results conducted in a setup, which fulfills the prerequisites for reaching a high temperature lift as it consists of a high-performance reactor operated at a high pressure ratio of 14. The first section describes the obtained characteristics in terms of specific cooling power and cooling efficiency for temperature lifts from 20 K to 40 K. For each temperature setting the results with and without the applied TSVS-strategy are presented and compared to the state of the art. In a subsequent section the results are used to validate the lumped model of the reactor. The third section takes another approach for evaluating the efficiency by assuming a closed system with an ideal compressor. This enables the comparison with an electrically or mechanically-driven refrigeration cycle.

3.1. Specific cooling power and cooling efficiency

The plot on the left hand side of Fig. 7 shows the MH mass specific cooling power as a function of the SDR for different applied cold and hot side temperatures (T_c and T_h) and with applied TSVS-strategy. The right plot of Fig. 7 shows the same results without considered TSVS. Each data point represents the mean over 9 cycles on constant boundary conditions and therefore a steady-state operation point. The corresponding error bars show the minimum and maximum of the evaluated cycles. The temperature sets are chosen in the way to symmetrically increase the temperature lift ΔT_{lift} from 20 K to 40 K around a mid-temperature of 25 °C. Additionally the temperature set of 5|25 °C ($T_c|T_h$) is applied, where only the cold side is reduced by 20 K from the reference temperature.

For every temperature set, the experimental data in Fig. 7, as well as the results from the lumped model, show a characteristic profile for the specific cooling power with a maximum at an optimal SDR. It is caused by two contradictory effects that occur for an increasing SDR. As a first effect, the increased SDR leads directly to an increased conversion rate and therefore to a higher thermal power per mass of MH. For an idealized case, this is represented by a straight line in Fig. 7, denoted as $\dot{q}_{c,lim}$. It is determined only by the reaction enthalpy of the used MH neglecting sensible heat losses. The seconds effect is shown by the results of the hydrogen section in Fig. 8, in which a decreasing reaction conversion Δw per half cycle at increasing SDR is visible. This is caused by an increasing temperature difference from the HTF to the reaction bed, which leads to the equilibrium being reached earlier. Consequently, the final desorption pressure of 5 bar is reached at a reduced conversion and less reaction cold can be generated, whereas the sensible loss caused by the cooling down phase remains the same. Exceeding the optimal SDR, the cold per half is reduced to such an extent that the sensible heat loss dominates.

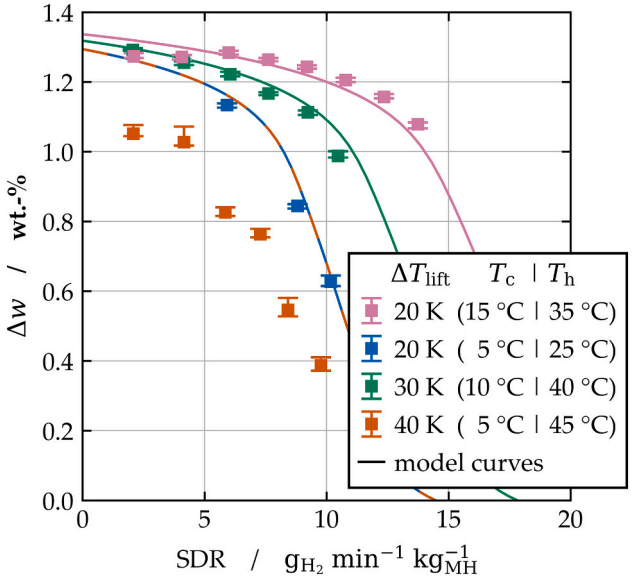

Fig. 8. Reaction conversion depending on the specific discharge rate for different temperature settings.

The temperature setting of 15|35 °C shows the lowest investigated temperature lift of 20 K. This setting is applied, since the previous experiments of this reactor with 10 bar desorption pressure were conducted at this temperatures as well. The results in Fig. 7 show a maximum specific cooling power of 613 W/kg$_{MH}$ that leads to less than 2 kg$_{MH}$ per Kilowatt cold. It is roughly doubled than the result of 317 W/kg$_{MH}$ for the previous experiment at 10 bar, shown in Fig. 7 (left) as grey dotted line. From a MH reaction perspective, the higher specific cooling power compared to the 10 bar-experiment is reasonable, since the reduced pressure of 5 bar leads to a higher distance from the equilibrium

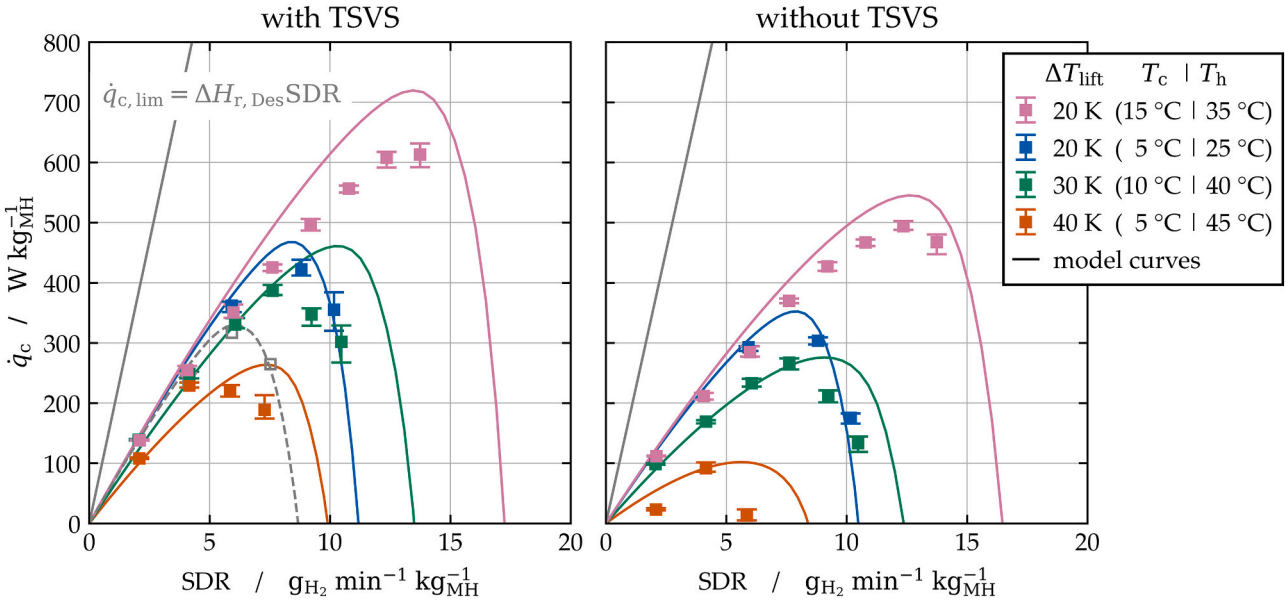

Fig. 7. MH mass specific cooling power for different temperature settings, applying the TSVS-strategy (left) and without it (right). Grey dashed line and grey empty points show previous results on 15|35 °C at 10 bar back pressure [28].

at the desorption. Thus, a higher conversion rate and therefore specific cooling power is possible before the characteristic line declines due to a significant reduced conversion, cf. Fig. 8.

The temperature setting of 5|25 °C also applies a temperature lift of 20 K, compared to the 15|35 °C-setting. However, the experimental results show a lower characteristic for the specific cooling power in Fig. 7 with a significantly reduced maximum at 422 W/kg$_{MH}$. This is remarkable, since both experimental setups not only have the same temperature lift, but also have the same pressure ratio and therefore use the same energy potential. It can be explained by the crucial effect of the cold side temperature. The lower cold side temperature of 5 °C leads to a smaller distance to the equilibrium at the desorption end pressure. In contrast, on the absorption side, the 5|25 °C-setting benefits from a higher distance from the equilibrium. It enables shorter regeneration times within the available half cycle time, that is determined by the parallel desorption of the second reactor. However, as Fig. 8 shows for the reaction conversion, the system is able to fully absorb even at 35 °C in the available half cycle time. That implies both systems are only desorption limited. The 15|35 °C-setting reaches a higher specific power, since 15 °C cold side temperature has a higher distance from the equilibrium, at the applied desorption end pressure, than 5 °C. It shows that not only the pressure ratio is important for a high performance. It determines only the upper physical limit. However, for a high-performance system a proper choice of absolute temperature and pressures for a certain material is equally important.

For the experiments at 30 and 40 K temperature lift, Fig. 7 shows the principle behavior of a decreasing specific power with increasing temperature lift. The maximum cooling power for the 30 K-experiment is 386 W/kg$_{MH}$. The lower value compared to the 15|35 °C-setting (20*K*) can be explained by two main effects that occur. At first, the higher temperature lift directly leads to a higher sensible loss at each half cycle switching. At second, the reduced cold side temperature of 10 °C is closer to the equilibrium and therefore allows only a lower SDR before the conversion per half cycle drops significantly, as shown in Fig. 8.

The highest temperature lift of 40 K was applied by a cold side temperature of 5 °C and a hot side temperature of 45 °C and thus represents the most relevant setting for application as a vehicle A/C. The corresponding characteristic in Fig. 7 reveals a further reduced specific cooling power of 229 W/kg$_{MH}$. It is nearly the same the first prototype for an open MHCS reached [25], however at 40 instead of 10 K temperature lift. Leading to 4.4 kg MH material per Kilowatt, it can be considered as suitable for scaling up in a mobile system.

The results for the conversion in Fig. 8 reveal a further aspect in addition to the principle behavior of a decreasing conversion with increasing SDR and the earlier decrease for a reduced cold side temperature. Fig. 8 shows moreover, that the principle behavior applies to all curves except the curve for the 5|45 °C-experiment. For this temperatures, the measured values for the conversion Δw are clearly below the ones of the 5|25 °C-setting, despite the same cold side temperature. It can be explained by a lower starting point of Δw for the cold half-cycle. This implies that the regeneration in the absorption half cycle could not be finished completely, since the hot side temperature of 45 °C is too close to the equilibrium temperature at 70 bar. It means that for the selected material and an upper pressure level of 70 bar, the maximum hot side temperature is somewhere between 40 and 45 °C. In order to increase the performance at 45 °C and higher temperatures, the absorption pressure must therefore be increased. Considering the results of the model, Fig. 8 show the same conversion line for 5|25 °C and 5|45 °C, which was also expected for experimental results. It confirms that the absorption limitation, which is not considered in the model so far, becomes relevant for this case.

Fig. 9 shows the cooling efficiency for the investigated temperature setting as a function of the SDR. The curves show a similar course to that of the conversion, since a decreased conversion leads directly to a lower efficiency. For the cooling efficiency, however, also the sensible heat losses from the half cycles switches are relevant. They lead to a greater difference of the various curves on the y-axis, showing a significantly reduced cooling efficiency for an increased temperature lift, even for a low SDR. The resulting cooling efficiencies for the highest specific cooling power are between 48 and 59 %. The characteristic shows an increasing value for a reduced SDR, which is due to a corresponding higher conversion. This trend is observed for all applied temperature sets except for the 40 K-curve. Here the measurement point for the lowest or second lowest SDR have to be considered as outlier.

3.2. Model validation

As it can be seen in the comparison of experiment and simulation (in Fig. 7 and Fig. 9), the model presented in Sec. 3 describes the characteristic for the cooling power and efficiency for most of the temperature sets quiet well. The corresponding model parameters are listed in Table 3 in the appendix. The mean deviation for the maximum power and the

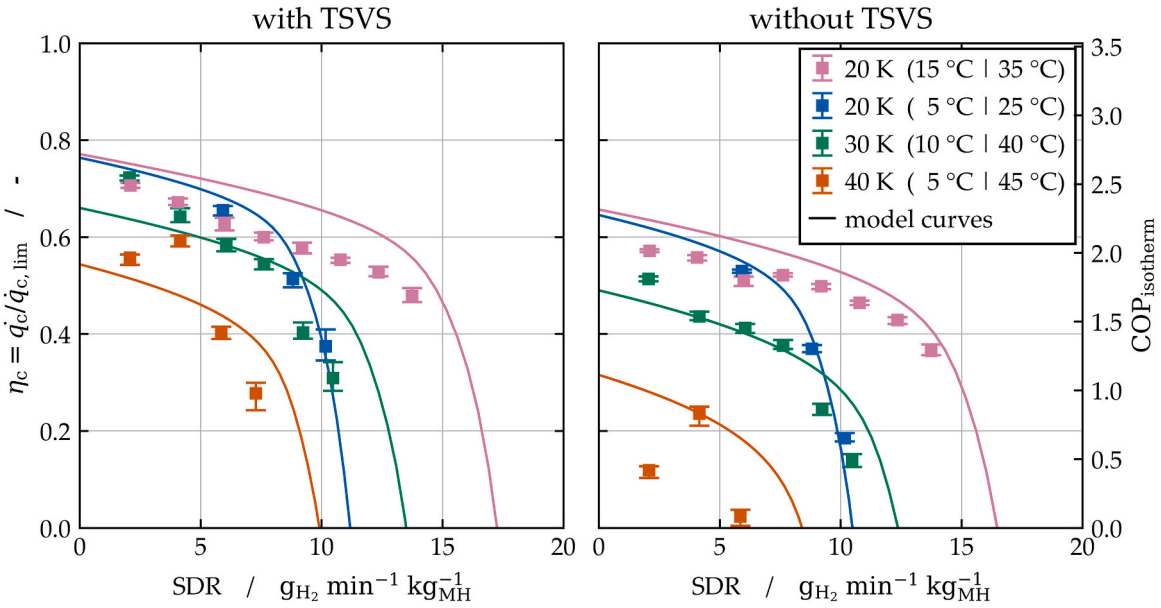

Fig. 9. Cooling efficiency for different temperature lits ΔT_{lift} ($T_c|T_h$) as the cooling power normalized by the material limit, determined by the reaction enthalpy.

corresponding efficiency is only 16 % and even lower for the case without TSVS. As a result, it can be considered as a valid predesign tool for reactor development, material evaluation and performance prediction on different temperature boundaries. Herein the temperature setting of 5|45 °C is excluded, since the model is not valid for the herein occurring absorption limitation Thus it has to pointed out that the model is only valid if the MH inside the reactor can be fully regenerated in the regeneration half cycle. For the presented setup this is not possible any more at the hot side temperature of 45 °C, since this temperature is too close to the equilibrium. Hence a possible absorption limitation is necessary to be implemented in the model.

The model predicts the optimal SDR precisely for 15|35 °C and 5|25 °C with a deviation of 2 % and 4 % respectively, whereas for 10|40 °C and 5|45 °C the deviation is significantly higher at 34–78 %. However, the knowledge of the correct optimal SDR is important to be implemented in a hydrogen flow controller that prevents the system from a dropping performance caused by a too high discharge rate. Consequently, it must be noted that the model is valid for reactor pre-design, but not valid for use in a controller. Instead it is rather recommended to fit the experimentally obtained performance points by a fitting function for each temperature set, as exemplarily shown in Fig. 11, in order to generate a characteristic map.

Comparing the reactor performance between with and without TSVS, Fig. 7 and Fig. 9 show a significant improvement in power and efficiency for the case with applied TSVS. The improvement increases with increased temperature lift from about 30 % for 10 K to 45 % for 30 K to even 250 % for the highest temperature lift of 40 K. This effect is reasonable, since an increased temperature lift increases also the sensible losses caused by the HTF, that are primarily aimed to mitigate by the TSVS.

The measurements are in good alignment with the first demonstration of Weckerle et al. [24], where an improvement of 26 % was reported at a temperature lift of 10 K. Thus, it can be stated, that the application of TSVS is even more important for increased temperature lifts.

3.3. Thermodynamic efficiency

In the previous chapter the cooling efficiency η_c was used as a material related evaluation parameter for the efficiency. It indicates to which extend the material is utilized by the realized reactor design under the applied operation conditions. Therefore, it is especially useful for reactor assessment and for predesigning a scaled-up system for an application (cf. Sec. 4). However, it does not represent a thermodynamic efficiency. In contrast, the available energy for an open MHCS on a certain pressure ratio, calculated in Sec. 2.1, can be taken as a reference. Even though this energy is available for free in a FVEC, it is worth analyzing how well this energy is utilized from a thermodynamic point of view.

Thereto, the system is considered separately from the hydrogen flow between high-pressure tank and low-pressure FC. Instead, the hydrogen outlet is virtually connected with the inlet via an ideal assumed compressor. Fig. 10 shows this setup, representing a closed system. The two pressure regulators from the FCEV integration setup are retained for this configuration. Therefore, the compressor has to deliver a constant pressure of 70 bar, sucking hydrogen at a constant pressure of 5 bar. The minimal energy, that is required for this compression, is determined by the isothermal process, that equals the calculation for the usable exergy of an open system in Sec. 2.1. This leads to the definition of an isothermal Coefficient of Performance ($COP_{isotherm}$) in Eq. (12), assuming the hydrogen being heated up to ambient temperature before entering the compressor

$$\mathbf{COP_{isotherm}} = \frac{\dot{\boldsymbol{Q}}_c}{\dot{\boldsymbol{m}}_{H_2}\, \boldsymbol{R}_{H_2}\, \boldsymbol{T}_{amb}\, \ln\left(\frac{\boldsymbol{p}_{high}}{\boldsymbol{p}_{low}}\right)} \tag{12}$$

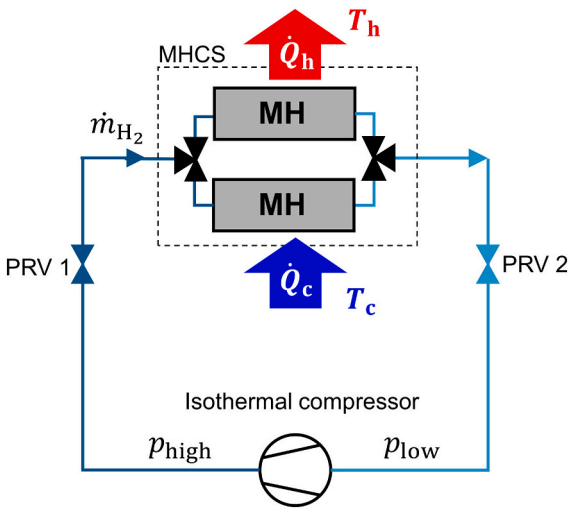

Fig. 10. Flow diagram of the metal hydride cooling system (MHCS), closed by an assumed isothermal compressor.

The results for this theoretical setup can be taken from the secondary y-axis in Fig. 9. Since according to Eq. (12) the $COP_{isotherm}$ is proportional to the cooling efficiency η_c, it shows the same behavior of a reduced SDR leading to a higher COP with the disadvantage of a lower specific power. For the optimum SDR the corresponding $COP_{isotherm}$ is at approximately 1.5 for the temperature lifts of 20 K and 30 K and can be increased to a 2.5 for the 20 K-settings by lowering the SDR. The result shows that the present reactor uses the available energy with a COP in the same range as the COP of a conventional vapor compression system (VCS), that typically has a COP of 2. At this point, it must be emphasized that the reference value for the VCS is electrical or mechanical energy causing fuel costs and a reduction of vehicle range. Whereas the reference for the open MHCS is unused available energy and thus leads to no further energy consumption for the vehicle but instead to an overall increase in system efficiency.

4. Discussion on sizing for applications

For a vehicle application with a certain available hydrogen flow rate, the question arises, how large the lab-scale system should be scaled up in terms of applied mass of MH and what thermal power could be achieved by it. In order to determine an appropriate size, a diagram for the absolute cooling power as a function of the applied MH mass is beneficial. The deduction of such a diagram using the mass specific characteristics of a prototype reactor is presented in the following. It is exemplarily conducted for the reactor of this work using the experimental results from Sec. 3.

The scaling considered in this section is meant not to affect the reactor concept itself. The current reactor could therefore be scaled either by the number or the length of tubes, or a modular scaling is realized with several reactors in parallel. At first, a certain temperature setting is chosen as the thermal design point. The corresponding measurement data for the specific power and cooling efficiency are then approximated with a fitting function, as Fig. 11 (left) shows for the 10|40 °C-experiment of the current reactor using a polynomial function (cf. Table 4 for coefficients). In the second step, the optimal MH mass is determined for the specific hydrogen flow rate available in the target FCEV. It is obtained by dividing the design flow rate by the optimal SDR. As an example, an available hydrogen flow rate of 55 g min^{-1} is assumed, which corresponds to a FC power of 55 kW at an efficiency of 50 % (LHV_{H2} = 120 MJ/kg). This assumed power represents the typical average continuous FC power of a FC-powered bus, whereas for a FC-powered truck or train this value has to be approximately doubled. With the optimal SDR of 7.97 g min^{-1} kg_{MH}^{-1} from the fitting function in

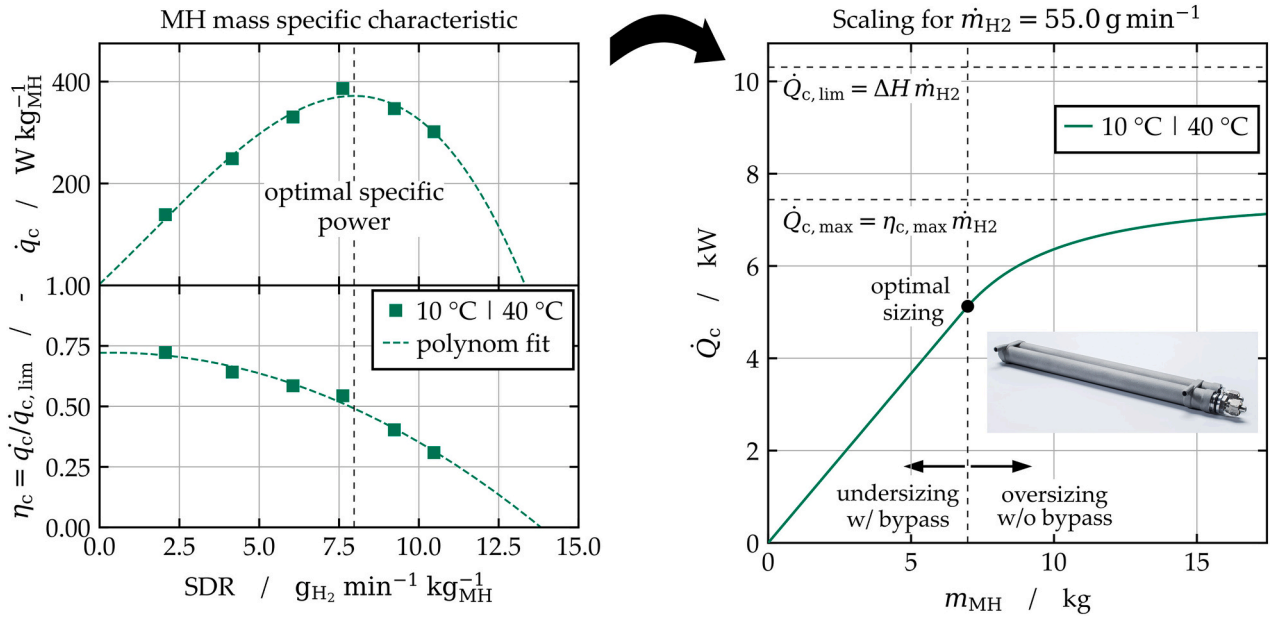

Fig. 11. Polynomial fitted reactor characteristic for experiments on T_c=10 °C and T_h=40 °C (left), and scaling case for $\dot{m}_{H2}$ = 55 g min^{-1} showing the effect of utilized MH mass on the absolute cooling power (right).

Fig. 11 (left) the optimal mass is calculated to be 7 kg. It refers to a scale-up factor of 20 related to the presented lab-scale prototype, which is assumed to be feasible since the presented prototype is relatively small and a bundle version with 25 tubes is currently under construction. The corresponding absolute cooling power on this optimal design point is 5.1 kW, calculated by the optimal MH mass multiplied with the maximum specific cooling power of the fitting function (372 W/kg$_{MH}$). From an application point of view, the continuous cooling power of 5 kW could cover the base cooling load of the assumed FC bus.

As an alternative to this optimal size, the use of a smaller system for this hydrogen flow rate is also possible, but would lead to a SDR above the optimum and a consequently lower cooling output than possible. To prevent this suboptimal operation, a permanent bypass is assumed that only allows the amount of hydrogen to flow through the MHCS which leads to the optimum SDR. It ensures the system to actually achieve the maximum cooling power, that is possible with this lower MH mass. In general, a linear graph from zero to the optimal sizing point can be drawn, cf. Fig. 11 (right), defining a region, which can be denoted as undersizing region. In contrast, the region that is related to a system exceeding the optimal MH mass, is denoted as oversizing region. In this region, the graph for the absolute cooling power is calculated directly with the specific power from the fitting curve in Fig. 11 (left) at the corresponding SDR, without the need to consider a bypass.

As a result, Fig. 11 (right) shows in principle that upscaling the system by an increased mass of MH increases the obtained cooling power in every case. For sizes from zero to the optimal mass, the power raises with a constant gradient. In this undersizing design region, a higher MH mass could reduce the bypassed hydrogen flow and therefore could use the available hydrogen flow to a higher extend resulting in a higher thermal output. For scaled-up systems exceeding the optimal mass, no bypass is needed any more and the cooling output increases further due to an increased cooling efficiency at a reduced SDR (cf. Fig. 11 left). However, the curve has a declining gradient, implying that a further increase in mass increases the cooling output only to a smaller extend. Sizing the system in this oversizing region, thus requires a disproportional higher mass.

Fig. 11 (right) additionally shows two horizontal lines representing upper limits. The upper defines the material limited cooling power $\dot{Q}_{c,lim}$, determined only by the reaction enthalpy multiplied with the hydrogen flow rate and considering no sensible losses. The second line defines the maximum cooling power $\dot{Q}_{c,max}$ the current reactor could reach. It is determined by the maximum cooling efficiency that would be reached at full conversion for a SDR going to zero and could therefore only be reached with an infinite high MH mass.

The method described above of deducing a diagram which shows the achievable cooling power for different sizes of the MHCS, is now applied in order to calculate the efficiency gain on vehicle level. Thereto a reference vehicle is considered, equipped with a conventional electricity powered A/C with a typical COP of 2 [31]. In the above-mentioned example case, the reference bus has to use 2.5 kW electrical power for the generation of 5 kW cold, that the open MHCS can generate from the available hydrogen flow without electricity consumption. It reduces the FC output of the reference vehicle to 52.5 kW compared to the retained full 55 kW-output of the MHCS-equipped vehicle. As a result, the application of the open MHCS shows an efficiency improvement of 4.8 % at the optimal sizing. A sizing with a higher MH mass can further increase the efficiency improvement, albeit to a lesser extent. For instance, doubling the MH mass to 14 kg increases the cooling output of the open MHCS only to 6.9 kW, cf. Fig. 11 (right). For this higher cooling power, the reference bus would require 3.45 kW electrical power and hence would have a reduced net FC output of 51.55 kW. Consequently, the vehicle equipped with the open MHCS shows an increased efficiency improvement of 6.7 %, but with a doubled system size compared to the optimal sizing.

In order to emphasize the economic relevance of the calculated efficiency improvement, a rough estimation of the fuel cost saving is given. Assuming a yearly operation time of 2500 h for a commercially operated FC bus and a hydrogen price of 8 €/kg$_{H2}$, a yearly cost saving of 3200 to 4400 € depending on the sizing of the MHCS is calculated. Thus, an amortization period of less than 10 years is very likely.

It should be noted that this efficiency is only apparent for a steady-state FC operation at this design point (temperatures and hydrogen flow rate) and if the produced cold is actually required and would have been produced electrically instead. For a more detailed analysis of the efficiency gain at vehicle level going beyond this pre-dimensioning methodology, the dynamic profiles of the FC and cold load have to be considered as well. Therefore, either a dynamic simulation model, like the one in [36], or interpolations in between a characteristic map

deduced from the experimental results could be suitable.

5. Conclusion

This work aimed to achieve an application relevant temperature lift of the open MHCS to allow its use as a air-condition system in a vehicle. Therefore, in the first section, the optimal pressure ratio of the open MHCS is discussed, with respect to the best energy recovery from the compression state of the gaseous hydrogen inside a pressure tank of a FEV. For each specified low pressure, it reveals an optimal high-pressure level for the best exergy utilization. However, a compromise has to be found between exergy utilization and coverage of operation time. Moreover, the analysis shows that lowering the back pressure (FC supply pressure) increases the exergy utilization in every case.

In order to generate a higher temperature lift than 20 K, which was the highest achieved values published so far, at first, a high-performance reactor from a previous study is used. It facilitates a high heat transfer at a low one structural mass at the same time. At second, an increased pressure ration of 14 is selected, realized by a decreased back pressure of 5 bar compared to 10 bar in the previous study. The experiments show an almost doubled specific cooling power of 613 W/kg_{MH} at reference conditions of 15|35 °C, that is caused by the higher available energy potential. It represents the highest value known in literature for an open MHCS. Moreover, higher temperature lifts of 30 K and 40 K could be demonstrated along with a comprehensive reactor characterization under these conditions. As expected, it shows a decreasing maximum specific power with increasing temperature lift, but still reaches 229 W/kg_{MH} for 5 °C cold and 45 °C hot side temperature. Considering also the result at 5|25 °C and 10|40 °C, and comparing all results with each other, it shows furthermore, that for achieving a high temperature lift it is not sufficient to apply a high pressure ratio and use a high-performance reactor. Additionally, a suitable selection of the MH material for the chosen pressure and temperature conditions is also important. T.

The predicted results of a lumped mass model, are compared with the experimental obtained characteristics and showed a maximum deviation of 16 % for the highest specific power and corresponding cooling efficiency over all investigated temperature settings. Since the model was also able to represent the results on a lower back pressure in a previous study, it can be considered as a valid tool for pre-dimensioning a reactor under various temperature and pressure boundaries.

Further on, a method is presented to describe the cooling output of a scaled-up system and the resulting efficiency improvement for the FCEV. An example vehicle with a 55 kW-FC (at 50 % FC efficiency) at thermal design point of 10|40 °C, shows a total efficiency improvement by 4.8 % at the optimal scale of 7 kg MH. A further increase of the MH mass by 57 % could push the efficiency gain to even 6.3 %.

In conclusion, the experimental demonstration of a temperature lift of 40 K at a cooling temperature of 5 °C reaching a specific power of >200 W/kg indicated, that the performance requirements for the application as a air-conditions system in a FCEV can be accomplished on lab-scale. A scaled version of this system promises a significant efficiency improvement of ~5 % on vehicle level and could therefore assist the establishment of FCEVs for a decarbonized mobility sector.

CRediT authorship contribution statement

Alexander Wimmer: Writing – original draft, Visualization, Validation, Software, Resources, Methodology, Investigation, Formal analysis, Data curation, Conceptualization. **Marc Linder:** Writing – review & editing, Funding acquisition. **Inga Bürger:** Writing – review & editing, Supervision, Resources, Project administration, Funding acquisition, Conceptualization.

Declaration of competing interest

The authors declare that they have no known competing financial interests or personal relationships that could have appeared to influence the work reported in this paper.

Acknowledgment

Discussions with Hanna Lösch and Markus Kordel have been appreciated.

Appendix A. Appendix

Table A1
Parameters of PCI fitting polynomial.

	Absorption ($n = 11$)	Desorption ($n = 8$)
T_{ref} in °C	30	30
ΔH_R (Abs/Des) in J mol_{H2}^{-1}	17,459	22,669
k_0	−0.21	0.28
k_1	66.28	−134.5
k_2	−1683.2	1873.51
k_3	20,079.61	−7044.45
k_4	−96,220.69	13,514.4
k_5	253,312	−14,943.32
k_6	−411,912.82	9646.95
k_7	432,855.2	−3383.56
k_8	−295,316.37	498.63
k_9	126,507.35	
k_{10}	−30,941.97	
k_{11}	3297.74	

Table A2
Model parameters.

Parameter	Symbol	Value
Metal hydride material properties		
maximum total hydrogen capacity, wt.-%	$w_{max,total}$	1.9
plateau mid hydrogen capacity, wt.-%	w_{mid}	1.1
absorption end capacity, wt.-%	$w_{abs,end}$	1.54
kinetic constant, s^{-1}	K_0	190,400
activation energy, J	E_a	$5.083*10^{-20}$
density of MH, kg m^{-3}	ρ_{MH}	6300
mass specific heat capacity of MH, J kg^{-1} K^{-1}	c_{MH}	500
Reactor properties		
inner radius of MH compacts, m	r_i	1.7e-3
outer radius of MH compacts, m	r_o	7.5e-3
heat transfer coefficient to HTF for des, W m^{-2} K^{-1}	α_{des}	3000
heat capacity ratio related to MH, –	k_C	2.2 (1.6 w/o fittings)
effective heat conductivity of MH compacts, W m^{-1} K^{-1}	λ	10 [37]
effective permeability of MH compacts, m^2	κ	1.5e-15
Operation conditions		
temperature difference of HTF inlet and outlet, K	ΔT_{HTF}	3
Hydrogen and HTF properties		
dynamic viscosity of hydrogen, Pa s^{-1}	η	$9.05*10^{-6}*(T / 293)^{0.68}$
density of HTF, kg m^{-3}	ρ_{htf}	1082
mass specific heat capacity of the HTF, J kg^{-1} K^{-1}	c_{htf}	3260

Table A3
Parameters of polynomial fitting function for measurement on 10|40 °C-setting.

	Specific cooling power ($n = 3$)	Cooling efficiency ($n = 2$)
p_0	5.068	0.722
p_1	117.758	0.003
p_2	5.363	−0.004
p_3	−1.067	

Data availability

Data will be made available on request.

References

[1] Link S, Stephan A, Speth D, Plötz P. Rapidly declining costs of truck batteries and fuel cells enable large-scale road freight electrification. Nat Energy 2024;9:1032–9. https://doi.org/10.1038/s41560-024-01531-9.

[2] Jorgensen SW. Hydrogen storage tanks for vehicles: recent progress and current status. Curr Opin Solid State Mater Sci 2011;15:39–43. https://doi.org/10.1016/j.cossms.2010.09.004.

[3] Ahluwalia RK, Hua TQ, Peng JK. Fuel cycle efficiencies of different automotive on-board hydrogen storage options. Int J Hydrogen Energy 2007;32:3592–602. https://doi.org/10.1016/j.ijhydene.2007.03.021.

[4] Durbin DJ, Malardier-Jugroot C. Review of hydrogen storage techniques for on board vehicle applications. Int J Hydrogen Energy 2013;38:14595–617. https://doi.org/10.1016/j.ijhydene.2013.07.058.

[5] Jensen JO, Vestbø AP, Li Q, Bjerrum NJ. The energy efficiency of onboard hydrogen storage. J Alloys Compd 2007;446-447:723–8. https://doi.org/10.1016/j.jallcom.2007.04.051.

[6] Nishizaki T, Miyamoto K, Yoshida K. Coefficients of performance of hydride heat pumps. Journal of the Less Common Metals 1983;89:559–66. https://doi.org/10.1016/0022-5088(83)90372-7.

[7] Dantzer P, Orgaz E. Thermodynamics of the hydride chemical heat pump: model (I). J Chem Phys 1986;85:2961–73. https://doi.org/10.1063/1.451006.

[8] Lee SG, Kim YK, Lee JY. Operating characteristics of metal hydride heat pump using Zr-based laves phases. Int J Hydrogen Energy 1995;20:77–85. https://doi.org/10.1016/0360-3199(93)E0005-6.

[9] Willers E, Groll M. Evaluation of metal hydride machines for heat pumping and cooling applications: evaluation des machines à hydrure métallique dans les applications de pompes à chaleur et de refroidissement. Int J Refrig 1999;22:47–58. https://doi.org/10.1016/S0140-7007(97)00056-X.

[10] Linder M, Kulenovic R. An energy-efficient air-conditioning system for hydrogen driven cars. Int J Hydrogen Energy 2011;36:3215–21. https://doi.org/10.1016/j.ijhydene.2010.11.101.

[11] Linder M, Mertz R, Laurien E. Experimental results of a compact thermally driven cooling system based on metal hydrides. Int J Hydrogen Energy 2010;35:7623–32. https://doi.org/10.1016/j.ijhydene.2010.04.184.

[12] Ge YT, Lang PY. Performance analysis of a metal hydride refrigeration system. Appl Therm Eng 2023;234:121264. https://doi.org/10.1016/j.applthermaleng.2023.121264.

[13] Zhang XY, Ge YT. Performance analysis of metal hydride heat pump system with CFD modelling development and actual reactor designs. Int J Hydrogen Energy 2024;94:1146–59. https://doi.org/10.1016/j.ijhydene.2024.11.204.

[14] Muthukumar P, Groll M. Erratum to "metal hydride based heating and cooling systems: a review" [international journal of hydrogen energy (2010) 35:3817–3831]. Int J Hydrogen Energy 2010;35:8816–29. https://doi.org/10.1016/j.ijhydene.2010.04.087.

[15] Muthukumar P, Kumar A, Raju NN, Malleswararao K, Rahman MM. A critical review on design aspects and developmental status of metal hydride based thermal machines. Int J Hydrogen Energy 2018;43:17753–79. https://doi.org/10.1016/j.ijhydene.2018.07.157.

[16] Malleswararao K, Dutta P, Murthy SS. Applications of metal hydride based thermal systems: a review. Appl Therm Eng 2022:215. https://doi.org/10.1016/j.applthermaleng.2022.118816.

[17] Lototskyy M, Sekhar B, Muthukumar P, Linkov V, Pollet B. Niche applications of metal hydrides and related thermal management issues. J Alloys Compd 2015;645:S117–22.

[18] Kim KJ, Feldman KT, Lloyd GM, Razani A. Compressor-driven metal-hydride heat pumps. Appl Therm Eng 1997;17:551–60.

[19] Magnetto D, Mola S, DaCosta DH, Golben M, Rosso M. A metal hydride Mobile air conditioning system. SAE International; 2006.

[20] Muthukumar P, Patil MS, Raju NN, Imran M. Parametric investigations on compressor-driven metal hydride based cooling system. Appl Therm Eng 2016;97:87–99. https://doi.org/10.1016/j.applthermaleng.2015.10.155.

[21] Jana S, Muthukumar P. Experimental studies on a closed cycle compressor operated metal hydride based cooling system with large hydrogen inventory. Int J Hydrogen Energy 2023. https://doi.org/10.1016/j.ijhydene.2023.07.007.

[22] Park J-G, Han S-C, Jang H-Y, Lee S-M, Lee PS, Lee J-Y. The development of compressor-driven metal hydride heat pump (CDMHHP) system as an air conditioner. Int J Hydrogen Energy 2002;27:941–4. https://doi.org/10.1016/S0360-3199(01)00187-2.
[23] Meier K, Kurtz C, Weckerle C, Hubner M, Bürger I. Air-conditioning system for vehicles with on-board hydrogen. Appl Therm Eng 2018;129:1150–9. https://doi.org/10.1016/j.applthermaleng.2017.10.087.
[24] Weckerle C, Nasri M, Hegner R, Bürger I, Linder M. A metal hydride air-conditioning system for fuel cell vehicles – functional demonstration. Appl Energy 2020:259. https://doi.org/10.1016/j.apenergy.2019.114187.
[25] Weckerle C, Nasri M, Hegner R, Linder M, Bürger I. A metal hydride air-conditioning system for fuel cell vehicles – performance investigations. Appl Energy 2019:256. https://doi.org/10.1016/j.apenergy.2019.113957.
[26] Weckerle C, Bürger I, Linder M. Numerical optimization of a plate reactor for a metal hydride open cooling system. Int J Hydrogen Energy 2019;44:16862–76. https://doi.org/10.1016/j.ijhydene.2019.04.260.
[27] Wimmer A, Linder M, Bürger I. Lumped model for a quasi-continuously operating open metal hydride heat pump system. Appl Therm Eng 2024:241. https://doi.org/10.1016/j.applthermaleng.2023.122250.
[28] Wimmer A, Kordel M, Linder M, Bürger I. High Performance Reactor of a Metal Hydride Based Cooling System for Air-Conditioning of Fuel Cell Electric Vehicles. SSRN. 2024.
[29] Pöhl J, Wimmer A, Bürger I, Kordel M, Heckert F. Improving driving range for FCEVs by use of an innovative metal hydride air-conditioning system. World Hydrogen Technology Convention; 2021.
[30] Fuel Cell Technologies Office Multi-Year Research, Development and Demonstration Plan, https://www.energy.gov/sites/prod/files/2015/05/f22/fcto_myrdd_storage.pdf.
[31] Lee Y, Jung D. A brief performance comparison of R1234yf and R134a in a bench tester for automobile applications. Appl Therm Eng 2012;35:240–2. https://doi.org/10.1016/j.applthermaleng.2011.09.004.
[32] Dornheim M. Thermodynamics of metal hydrides: Tailoring reaction enthalpies of hydrogen storage materials. In: Moreno Piraján JC, editor. Thermodynamics - interaction studies - solids, liquids and gases. Rijeka: IntechOpen; 2011.
[33] Kölbig M, Weckerle C, Linder M, Bürger I. Review on thermal applications for metal hydrides in fuel cell vehicles: operation modes, recent developments and crucial design aspects. Renew Sustain Energy Rev 2022:162. https://doi.org/10.1016/j.rser.2022.112385.
[34] de Miguel N, Acosta B, Baraldi D, Melideo R, Ortiz Cebolla R, Moretto P. The role of initial tank temperature on refuelling of on-board hydrogen tanks. Int J Hydrogen Energy 2016;41:8606–15. https://doi.org/10.1016/j.ijhydene.2016.03.158.
[35] Fueling protocols for light duty gaseous hydrogen surface vehicles. J2601. SAE. International 2020. https://doi.org/10.4271/J2601_202005.
[36] Kordel M, Radler D. Applied metal hydride system optimization to improve hydrogen fuel cell system performance in Mobile heavy-duty applications. ECS Trans 2024;114:713. https://doi.org/10.1149/11405.0713ecst.
[37] Dieterich M, Pohlmann C, Bürger I, Linder M, Röntzsch L. Long-term cycle stability of metal hydride-graphite composites. Int J Hydrogen Energy 2015;40:16375–82. https://doi.org/10.1016/j.ijhydene.2015.09.013.

3. Discussion

The three core publications of this thesis showed the model-based analysis, development and experimental characterization of a high-performance reactor for the desorption-driven open MHCS. In the following section, first, the discovered characteristics of this specific MH-system are discussed in the context of the other MH-based refrigeration or heat pump systems, as they are the heat-driven and the compressor-driven closed MH-system, see section 1.2.2. Furthermore, as one main application of such system is the utilization as an energy-efficient air-conditioner in a fuel cell electric vehicle (FCEV), in the second part, the technology is also compared with other technologies, especially with the concept of a mechanical expansion machine which also uses the potential energy (enthalpy) related to the onboard pressure tank.

3.1. Characteristics of the desorption-driven open MH-system

This work shows for the first time a comprehensive analysis of the characteristics of an open thermochemical refrigeration or heat pump system that operates at constant outlet flow. In order to discuss the characteristic followed by this kind of operation in a wider context, the three types of MH heat pump/refrigeration, described in the introduction part and depicted in Fig. 2, are compared in detail. A key difference between them in terms of operation characteristics are the variables which are kept constant over time from outside and the internal variables which are time-dependent.

- For the **heat-driven closed MH-system**, the heat source temperature in the regeneration half cycle represents the only constant variable, whereas the pressures and the hydrogen mass flow are internal non-constant variables in both half-cycles.
- For the **compressor-driven closed MH-system**, in both half cycles the compressor speed represents the constant variable that is applied in most reported configurations.
- For the **open MH-system**, it must be differed between the two half cycles. In the absorption half cycle a constant pressure is present, where as in the desorption half cycle a constant hydrogen flow rate is present resulting from a downstream arranged consumer, e.g. the fuel cell in a FCEV.

Accordingly, the three systems show different degrees of freedom during operation. Both the heat- as well as the compressor-driven MH-systems show the half cycle time and the amount of initially charged hydrogen as additional degrees of freedom besides the heat source

temperature or the compressor speed, respectively. In contrast, for the open MHCS studied in this work, the half cycle time is not a free variable. Instead it was found to be a result of the set desorption mass flow and consumer's pressure level, that represent the corresponding degree of freedom for the open MHCS system, see Tab. 2.

Tab. 2: Comparison between the three types of MHCS

	Heat-driven closed MHCS **[50]**	Compressor-driven closed MHCS **[38]**	Desorption-driven open MHCS **[44]**
Energy expend	Thermal energy	Compressor work	Enthalpy (previous spend compressor work for H_2 storage or distribution)
Fixed temperature levels	T_s, T_h, T_c	T_h, T_c	T_h, T_c
Fixed pressures	-	$p_\mathrm{compr,max}$	p_abs, $p_\mathrm{des,end}$
Behavior during steady-state operation	p_abs, p_des ≠ const. $\dot{m}_\mathrm{abs}$, $\dot{m}_\mathrm{des}$ ≠ const. $\boldsymbol{T_\mathrm{s}}$ **= const.**	p_abs, p_des ≠ const. $\dot{m}_\mathrm{abs}$, $\dot{m}_\mathrm{des}$ ≠ const. $\boldsymbol{n_\mathrm{compr}}$ **= const.**	$\boldsymbol{p_\mathrm{abs}}$ **= const.,** $\dot{m}_\mathrm{abs}$ ≠ const. p_des ≠ const., $\boldsymbol{\dot{m}_\mathrm{des}}$ **= const.**
Degrees of freedom	T_s, $m_\mathrm{H2,initial}$, t_hc	n_compr, $m_\mathrm{H2,init}$, t_hc	p_abs, $p_\mathrm{des,end}$, $\dot{m}_\mathrm{des}$

Generalized operation characteristics

The specific boundaries, summarized in Tab. 2, are considered in this work in a combined zero- and one-dimensional steady-state model (Paper I), that thereby extends the variety of literature-available models [48, 51] to this kind of MH-systems. It presents for the first time a model for a MH heat pump/refrigerator that is able to calculate not only the efficiency, but also the mean thermal power without solving the time-dependent differential equation for the reaction kinetics. The model results revealed a characteristic dependency of the thermal power and efficiency on the gas flow rate of the discharge side. This principle behavior could be validated with two different reactor concepts, a plate reactor [45] (Paper I) and a tube bundle (Paper II) under a variety of temperature settings and also at different discharge end pressures (Paper III). It is schematically depicted in Fig. 4 and will be discussed in the following at first for the SCP and at second for the cooling efficiency.

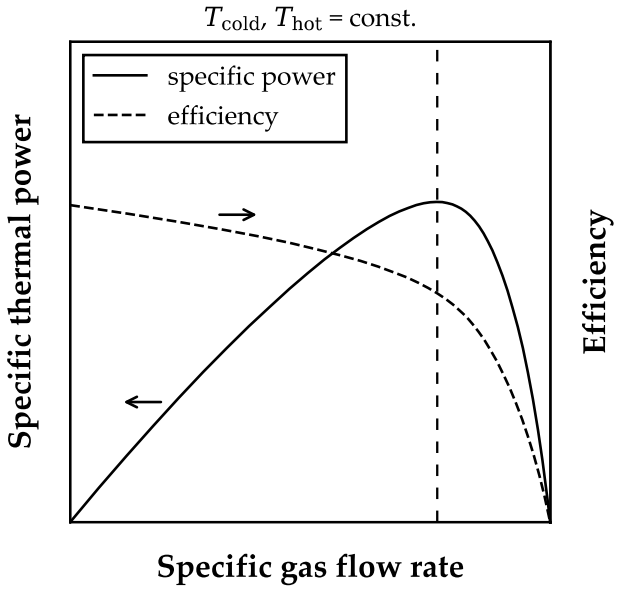

Fig. 4: Generic operation characteristic of the desorption-driven open MH-system

In Fig. 4, on the one hand, the SCP is shown on the left y-axis over the specific gas flow rate being discharged. It shows a clear maximum at an optimum specific discharge rate. The reason for the maximum is the occurrence of two contradictory effects. On the one hand an increased flow rate directly leads to an increased rate of heat release during the thermochemical reaction. On the other hand, an increased specific discharge rate leads to a decreased reaction conversion resulting in a decreased amount of reaction heat per half cycle and the predominance of the sensible heat losses. Thus, it was found that the maximum SCP does not occur for the full, but for a reduced conversion at an optimal specific discharge rate.

The strong effect of the discharge rate on the conversion can be considered as an analogy to the current-dependent usable capacity of electrochemical energy storages like lead-batteries [52]. It is also known in literature for MH-based hydrogen storage system [53]. However, for hydrogen storage application this effect is mostly not relevant during operation, since the storage reactor is mostly designed to the requirement to ensure full capacity at the highest occurring discharge rate. In contrast for the desorption-driven MH-system, the effect is of particular relevance and leads to an optimal operation point in terms of thermal power.

The efficiency on the other hand, is shown in Fig. 4 on the right y-axis versus the specific discharge rate. It is considered herein as the net thermal power (reduced by sensible losses) related to the maximum thermal power that is determined solely by the reaction enthalpy

multiplied by the discharge rate. For the efficiency, in contrast to the thermal power, no maximum occurs. Instead it is decreasing with increasing discharge rate, due to the reduced conversion. The opposed direction of power and efficiency shows that the highest efficiency is not reached at the optimum operation point, but could be increased for a lower gas flow rate with the drawback of a lower SCP. It has to be noted that the characteristic curves for power and efficiency in Fig. 4 are only valid for a fixed hot and cold side temperature. Another temperature set consequently results into another curve, but shows the same characteristic shape.

This operation characteristic for power and efficiency described above was so far unknown for the desorption-driven open MH system and complements the known characteristics of the two closed MH-systems. The literature reports that for both the heat- and the compressor-driven system an optimal half-cycle time and an optimal amount of initial hydrogen leads to a maximum thermal power. For the desorption-driven system however, the parameter that causes a maximum in thermal power was found to be the optimal desorption flow rate. Moreover, an additional analogy exists with the compressor-driven closed MH-system. Lloyd et al. [54] showed in a numerical study that the power can be increased with increased volume flow rate, with the drawback of a decreased efficiency. A similar relation was found for the desorption-driven open system, but for the mass flow instead of the volume flow. However, with more practical relevance, since the desorption-driven system shows a real constant mass flow to a hydrogen consumer, whereas the compressor-driven system in general does not show a constant volume flow at a set compressor speed.

Consequences of operation characteristic

From the investigated characteristic shown in Fig. 4 two main consequences can be deduced. The first one is related to a preferable operation strategy: The declining course of the thermal output after the optimum discharge rate suggests to avoid higher discharge rates than the optimum by using a hydrogen bypass path. It retains the maximum thermal power in case the hydrogen demand is too high for the MH-system. In a technical system it could be realized with a combination of a passive pressure-controlled bypass and an active mass flow controller at the outlet of the MH-system actively limiting the mass flow rate. For the controller, a characteristic map that contains the optimal discharge rates for different temperatures is therefore deduced from various characteristic curves. They are either generated by use of the presented model (Paper I) or by the experimental characterization procedure from Paper II and III.

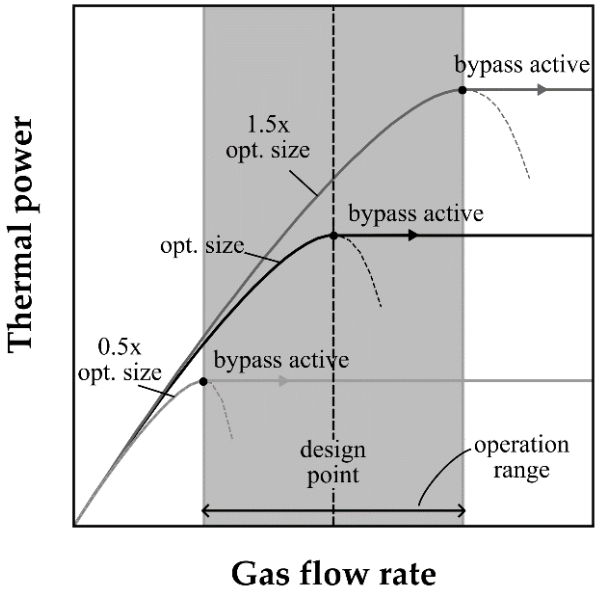

Fig. 5: Absolute thermal power over absolute gas flow rate for different sized MHCSs

The second consequence of the discovered characteristics of the desorption-driven open MH-system is related to the scaling strategy: The mass specific representation of the characteristic allows to determine the optimal scaling in terms of applied mass of MH to get the highest power density for a certain design mass flow rate, as exemplarily shown in Fig. 5 with the black line. For the case of a hydrogen consumer, which operates not at a constant but more dynamically in a range around a mean flow rate, it furthermore reveals that a larger size could be beneficial. As the line for 1.5x optimal mass in Fig. 5 exemplarily shows, at first it leads to a higher thermal output at the design point, due to a higher efficiency at the decreased specific discharge rate. At second, the higher scaled system is able to produce an increased thermal output instead of being limited in the thermal power, if the gas flow exceeds the design point. However, such an oversized system also has the disadvantages of higher investment cost, higher installation space and an increased weight.

In the present thesis, the operation characteristic was described for the reaction system of metal hydride and hydrogen. Besides the application as an air conditioner for FCEV in the motivation of this work, the findings presented herein can be transferred to any other case where the investigated system is applied between a high pressure hydrogen supply (e.g. pressure tanks or pipelines) and a low pressure hydrogen consumer. By use of other pressure levels and an appropriate selection of the MH material in the wide variety of available MHs, also other temperature levels can be addressed, where the MHCS could is used for instance in a

refrigerated truck [55] or as a stationary heat pump [56]. In those cases, similar sizing and operation problems occur, which can be solved by applying the results of this work.

Moreover, the model and characterization method described with the three publications is not only restricted to MH-based systems. Instead it is relevant for all kind of thermochemical gas-solid reaction systems that are operated at a constant desorption mass flow under the prerequisite of a conversion-dependent reaction kinetic. Therefore, the findings of this work can be applied to the development of other thermochemical heat pumps. For example, they can be applied for thermochemical systems working with water vapor as the gaseous reaction partner as they are subject of research as an industrial heat pump for upgrading waste heat to process heat [57]. Thereby the system can be integrated into process steam levels in which often a constant mass flow to a steam consumer is present and therefore fulfils the prerequisite to transfer the results from this work.

Applicability of developed tool for reactor design

The model developed in this work does not only represent the validated operation characteristic, but it can also be used as an ideal pre-design tool. In the early phase of reactor design several parameters can be considered as variables that can be varied either by reactor dimensioning, material selection or setting of operation conditions and are known to have a strong influence on the system performance [58]. For example, on reactor side such variables are the MH bed thickness and heat transfer coefficient. On MH material side for instance the MH bed porosity or the MH heat conductivity can be adjusted and on operation side the discharge rate can be varied to find the maximum thermal power. Moreover, the influence of the back pressure and the influence of different hot and cold side temperatures are of interest in most cases. This leads to a large parameter domain. In literature, however, only a transient 2D model is present so far for the description of desorption-driven open MHCS [59]. The model of this work, in contrast, shows an approximately 20 times faster computation, due to its steady-state approach, and thus facilitates large parameter variations and optimizations in the pre-design phase. It helps in the first step to get a proper basis for the design parameters. In a subsequent step the existing 2D transient model can be used to verify the assumptions made in the simplified model, for example the assumed homogenous reaction. Therefore, the steady-state 0D+1D model from this work enables a model-based reactor design from the beginning and closes the gap to obtain an overall development process.

In this work, as presented in the three published papers, such a model-based design process was conducted to build a high-performance reactor that reaches a higher SCP, cooling efficiency and temperature lift than reported in literature so far (summarized in Tab. 3). The developed reactor showed an 89% higher specific power at equal conditions (Paper I) as the plate reactor of Weckerle et al. [49] as the only known open MHCS in literature that was operated on a constant desorption mass flow. Referred not only on MH mass, but on the total mass of the reactor, the specific power could be increased by a factor of 3 and even higher for elevated temperature lifts. Whereas the previous system showed 15 kg per Kilowatt cooling power, the system of this work shows a system mass of only 5 kg (both without fluid pumps and valves). The thermal power could also be increased compared with the first experimental work of such system of Linder et al. [43], despite its beneficial mode of operation at constant outlet pressure instead of a constant flow rate.

Tab. 3: Performance comparison of open MHCS reported in literature

Author	**MH material**	**Reactor concept**	**Operation**	**Pressure ratio [-] (p_{max} [bar] / p_{min} [bar])**	**ΔT [K] (T_{hot} [°C] |T_{cold} [°C])**	**SCP [W/kg$_{MH}$]**
Linder et al. (2011) **[43]**	$TiMn_2$-based	Bundle (76 mm OD) of 372 fluid tubes (1.8 mm OD), MH powder in between	Const. H_2-outlet pressure	8.3 (50/6)	17 (30|13)	563
Weckerle et al. (2019) **[44, 49]**	$TiMn_2$-based	Plate heat exchanger with 1.67 mm mean plate distance, alternately filled with MH powder and fluid	Const. H_2-outlet flow rate	7 (35/5)	10 (30|20) 17 (30|13) 22 (42|20)	276 61 96
This work (Paper II and III) (2025)	$TiMn_2$-based	MH-ENG compacts in 15 mm tube with 4 mm bore, fluid micro channels in reactor wall	Const. H_2-outlet flow rate	7 (70/10)	10 (30|20) 20 (30|10) 20 (35|25) 20 (40|20)	522 198 317 349
				14 (70/5)	20 (15|35) 30 (10|40) 40 (5|45)	613 386 229

A broader view in the literature indicates that the reactor performance is most comparable with the compressor-driven MH system, since the hydrogen flow rate for such system is reported in several studies to occur nearly constant when operated at constant compressor-speed [42]. In contrast, the heat-driven system shows a highly non-constant mass flow during each half cycle, whereas the pressure remains nearly constant [60]. Comparing the experimental results achieved in this thesis (Paper II and III) with the literature of experimental studies on the compressor-driven system Tab. 1, it is seen that the achieved SCP outperformances not only the previous open systems but also the most comparable compressor-driven systems. It applies also for the temperature lift, which at 40 K is the highest one demonstrated so far, also for the compressor-driven system. In this regard it has to be mentioned that this temperature lift is not only an academic result, but rather represents the lower limit of the real required temperature lift for a vehicle air-conditioning system, which is addressed as target application [61].

These results were enabled, at first by a model-assisted development process, but also by the implementation of an established heat conduction enhancement method and the use of additive manufacturing. As the established measure to increase the low heat conductivity of MH powder, MH composite compacts were utilized consisting of a mixture of MH particles and 15 wt.-% expanded natural graphite [62]. The technique of additive manufacturing was mainly used for function integration in terms of integrated micro cooling channels. But it also avoided additional connection items, which would add parasitic thermal mass instead. So far, the innovative technology of additive manufacturing was used in literature only for MH-based heat [63] or hydrogen storage systems [64]. With this work it was used for the first time for a MH heat pump or refrigeration reactor, where its utilization has even more advantages. Likewise, for the first time high-strength aluminum was used for such a reactor, as proposed for instance by Magnetto et al. [40], in order to lower the mass and especially the crucial heat capacity of the reactor. The reactor developed in this work served then as an ideal basis for an upscaled version by a factor of >10, to build a system in the order of 5 KW for a subsequent technology integration project.

3.2. Evaluation of technological concept

The open MHCS of this work is developed with the intention to replace the conventionally used vapor compression system (VCS) in the air-conditioning unit in a FCEV in order to increase the total vehicle efficiency. In the subsequent section, the MHCS technology is compared in this context with a mechanical expander as another technology that recovers the potential

energy stored in the compressed gas in the high-pressure tank. As a reference for a mechanical expander, the study by Singer et al. [6] is referred to and for the MHCS the results of Paper II and III are considered. A configuration with a 700bar-tank and a fuel cell inlet pressure of 5 bar is considered, as it represents the case for which the MHCS prototype of this study was designed and characterized. The results of Singer et al. for the mechanical expander are evaluated originally with a fuel cell inlet pressure of 15 bar. They are recalculated for the following comparison with an inlet pressure of 5 bar, using the original methodology..

For a 700bar-tank and a 5bar-fuel cell the maximum possible energy, that an ideal expansion machine can generate, can be calculated by the exergy of a closed thermodynamic system according to Eq. (7), following the first principles of classical thermodynamics.

$$-w_{\mathrm{ex}} = h_{\mathrm{tank,initial}} - h_{\mathrm{FC,in}} - T_{\mathrm{amb}}\left(s_{\mathrm{tank,inital}} - s_{\mathrm{FC,in}}\right) + v_{\mathrm{tank,initial}}\left(p_{\mathrm{FC,in}} - p_{\mathrm{tank,inital}}\right) \tag{7}$$

For the assumed pressures it results in a specific energy of 4.76 MJ per kilogram hydrogen. Considering a fuel cell efficiency of 50% related to the LHV of hydrogen of 120 MJ/kg, an ideal expansion machine could supply additional energy that corresponds to a range increase of 7.9%. Alternatively, it can be considered as a reduced fuel consumption, denoted as fuel cost reduction in the following.

The ideal expansion machine is compared with an ideal open MHCS consisting of two ideal reactors that ensure full reaction conversion and have no thermal mass and therefore only show the sensible heat loss that results from the MH mass itself. Considering a real suitable MH material, that was used in the built-up reactor (Paper II and III) and a temperature lift of 30 K, this ideal system has a cooling efficiency η_{c} of 90%. According to Eq. (8), which is deduced from the definition of the cooling efficiency with the heat of reaction ΔH_{des}, the cooling power $\dot{Q}_{\mathrm{c}}$ related to the electrical fuel cell power P_{FC} corresponds to 17%.

$$\frac{\dot{Q}_{\mathrm{c}}}{P_{\mathrm{FC}}} = \frac{\Delta H_{\mathrm{des}}}{\mathrm{LHV}_{\mathrm{H_2}}\,\eta_{\mathrm{Fc}}} \tag{8}$$

For calculating the corresponding range increase it is assumed that this ratio of thermal to electrical power is actually required by the vehicle as an air-conditioning load and would have been generated instead by means of an energy-consuming conventional VCS, as schematically depicted in Fig. 6.

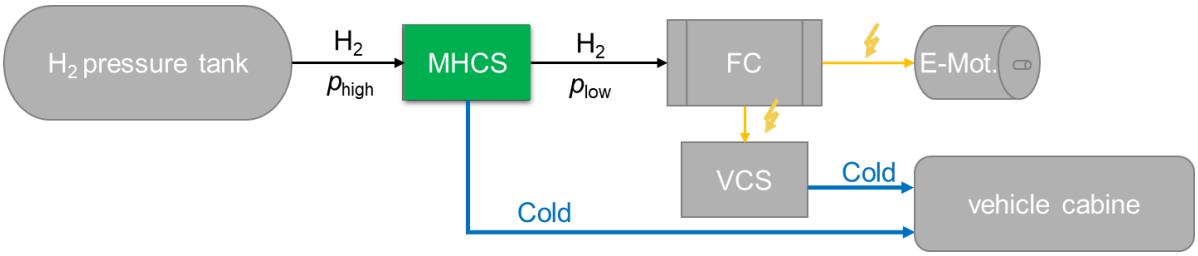

Fig. 6: Integration of the open MHCS and the conventional VCS in the power architecture of a fuel cell electric vehicle

Considering a typical COP of the conventional refrigeration system to be 2 [65], the fuel cost reduction for the ideal MHCS is calculated to 9.3% according to Eq. (9).

$$\text{fuel cost reduction} = \frac{1}{1 - \frac{\dot{Q}_c}{P_{FC}}\,\eta_c\,\frac{1}{COP}} - 1 \tag{9}$$

As shown in Paper III the possible utilization time has to be considered to get a more practical value for the fuel cost reduction reached by the MHCS. Considering it for the realized system of this work and an assumed empty tank pressure of 35 bar from the study of Singer et al., the fuel cost reduction is slightly reduced from 9.3 to 8.8%. As depicted in Fig. 7, it is still significantly higher than the corresponding range increase that can be generated by an ideal expansion system.

The higher possible range increase of the MHCS with an ideal reactor compared with the ideal expander is reasonable, since in this calculation a non-ideal refrigeration machine with a $COP<COP_{carnot}$ is considered as reference. In this context an ideal expander with a subsequent ideal Carnot-refrigeration machine would have the highest range increase, but is obviously not realistic.

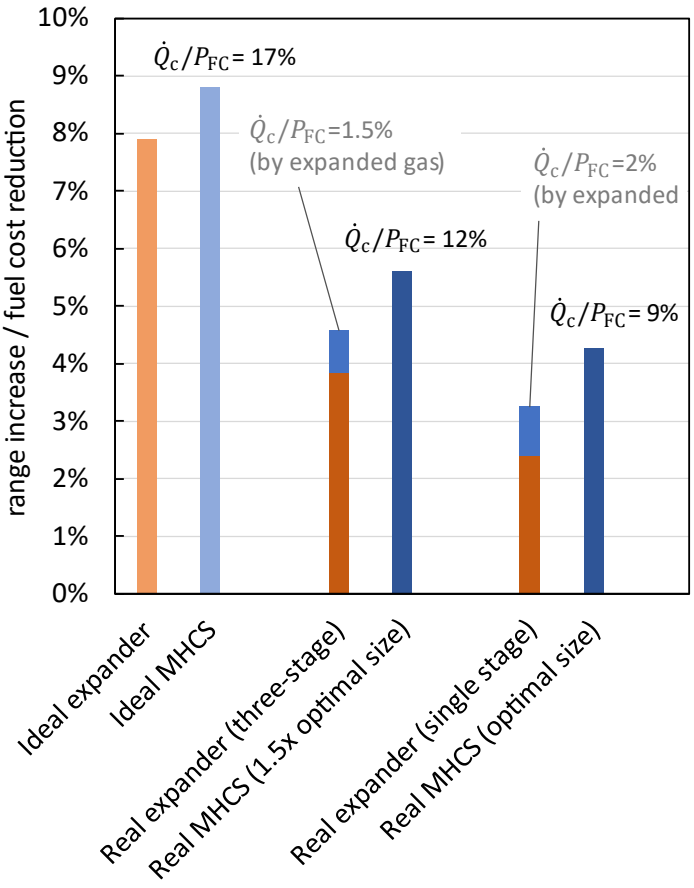

Fig. 7: Comparison between a hydrogen expander (calculated accordingly to Singer et al. [6]) and the MHCS (this work) in terms of range increase/fuel cost reduction for different realizations

Following the comparison of the ideal systems of the expander and the MHCS, real implementations are considered with their corresponding fuel cost reduction/range increase potential. For an implementation of the expander as a three stage machine the calculation according to the referred study shows a range increase of 4.6% assuming an isentropic efficiency of 60% for each stage. Due to the low gas temperature after the isentropic expansion, the expander could also generate an additional cooling power. However, this cooling power is only 1.5% of the fuel cell power [6], which according to Eq. (9) corresponds to only 0.7% of additional range increase. The three stage expander is a complex, heavy and costly system with the benefit of a higher efficiency compared to a single stage system. It can be therefore compared with the oversized MHCS with 1.5 times the optimal size, which also results in a higher efficiency with the drawback of a larger system. Considering the results of the built-up reactor of this thesis (Paper III, 30 K temperature lift), a cooling output of 12% of the fuel cell

power can be deduced. According to Eq. (9) it corresponds to a range increase of 5.6%, which is significantly higher than for the three-stage expander, see Fig. 7.

Due to the high complexity, Singer et al. proposed rather a single-stage than a three-stage expander as a more realistic variant for vehicle applications. It achieves a range increase potential of only 3.2%, including 0.8% range increase for the extra cooling effect. This less complex and more compact expander concept can be compared with the MHCS sized to an optimal mass leading to the highest power density. Based on the results of Paper III (30 K temperature lift) a range increase of 4.3% can be calculated, which is again higher than the single-stage expander also for this most vehicle-relevant implementation variant.

In conclusion, the technical evaluation of the MHCS in comparison with the competing technology of the hydrogen expander reveals a clear efficiency advantage for the MHCS under the prerequisite that the generated cold is actually required. The comparison, summarized in Fig. 7, shows this efficiency advantage is not only true for the ideal case, but also for the efficiency-focused and the mobility-focused implementation. Whereas for the considered expansion system only theoretical studies are available [5, 6], the results of Paper II and III enabled to calculate the potential fuel cost reduction for the MHCS on an experimental basis.

4. Summary of contributions

In this thesis, the characteristics of the open metal hydride cooling system (MHCS) were fundamentally investigated in order to optimize the system for application in hydrogen powered vehicles. The following main findings were incorporated in a model-based development of a new reactor design, that has proven an advanced thermal performance.

A simplified **model** was developed, which determines the mean specific cooling power (SCP) and cooling efficiency as the main outputs of interest. It considers a steady-state, lumped 0+1D-apporach, transferrable to other thermochemical gas-solid reactions showing a conversion-dependent kinetic and being operated at constant desorption flow rate. The model was validated with available experimental data. The main influences on power and efficiency, that were identified and considered in the developed model, are as follows:

- Metal hydride material: thermodynamic and kinetic parameters
- Boundary conditions: in- and outlet pressure, temperatures, desorption mass flow rate
- Reactor: heat and mass transport characteristics, heat capacity ratio

The developed model was used in a **numerical analysis** to investigate the thermal performance at different specific discharge rates representing fuel cell consumption rates. It was found that the specific discharge rate has a major influence on the quasi-continuous operation in two half cycles. An increasing specific discharge rates significantly decreases the conversion per half cycle, which leads to increasing thermal losses. It contradicts with a simultaneously increasing heat source rate and thus results in the following two characteristics for the thermal performance:

- Decreasing cooling efficiency with increasing specific discharge rate
- Maximum in specific thermal power at optimum specific discharge rate

In the course of a **technology demonstration** these findings were considered and the model was used as a numerical tool to design a new high-performance reactor. The reactor uses pelletizing methods established in literature to enhance heat conduction in the reaction bed, micro channels to enhance heat transfer to the laminar flow of the heat transfer fluid and additive manufacturing to reduce the reactor heat capacity. A developed test procedure with only one reactor reduces time and financial effort and allows comprehensive characterization

at different discharge rates. The experimental results represent technological milestones and fulfil typical requirements for the target application in vehicles.

The experiments at a pressure ratio of 7 demonstrated:

- Maximum SCP of 511 W/kg_{MH} at 20|30 °C
  (+89% compared to the literature at comparable conditions)
- Requirement of only 5 kg system mass per kilowatt
  (only 1/3 compared to literature)

Further experiments at a pressure ratio of 14 demonstrated:

- Enhanced SCP for the same reactor from 317 to 613 W/kg_{MH} at 15|35 °C
- For the first time a temperature lift of 40 K (5|45 °C) at a SPC of 229 W/kg_{MH}

Concluding, the discovery of the characteristics of the open MHCS and the model-based development of a lightweight reactor with an experimentally proven performance increase of over 80% as well as a two times higher temperature lift, have now set the scientific and technological basis for integrating the technology into a real fuel cell electric vehicle.

Bibliography

[1] Davis SJ, Lewis NS, Shaner M, Aggarwal S, Arent D, Azevedo IL, et al. Net-zero emissions energy systems. Science. 2018;360. https://doi.org/10.1126/science.aas9793.

[2] Link S, Stephan A, Speth D, Plötz P. Rapidly declining costs of truck batteries and fuel cells enable large-scale road freight electrification. Nat Energy. 2024;9:1032–9. https://doi.org/10.1038/s41560-024-01531-9.

[3] Durbin DJ, Malardier-Jugroot C. Review of hydrogen storage techniques for on board vehicle applications. Int J Hydrogen Energy. 2013;38:14595–617. https://doi.org/10.1016/j.ijhydene.2013.07.058.

[4] Jensen JO, Vestbø AP, Li Q, Bjerrum NJ. The energy efficiency of onboard hydrogen storage. J Alloys Compd. 2007;446-447:723–8. https://doi.org/10.1016/j.jallcom.2007.04.051.

[5] Wieser S, Muck N, Scharmach M. Hydrogen Expansion Work in Fuel Cell Electric Passenger and Heavy-Duty Vehicles by Simulative Assessment: A Comparison. IEEE Ind Appl Mag. 2023;29:59–69. https://doi.org/10.1109/MIAS.2022.3214021.

[6] Singer G, Köll R, Aichhorn L, Pertl P, Trattner A. Utilizing hydrogen pressure energy by expansion machines – PEM fuel cells in mobile and other potential applications. Appl Energy. 2023;343:121056. https://doi.org/10.1016/j.apenergy.2023.121056.

[7] Kim YM, Shin DG, Kim CG. On-Board Cold Thermal Energy Storage System for Hydrogen Fueling Process. Energies. 2019;12. https://doi.org/10.3390/en12030561.

[8] Wu S, Feng L, Changizian S, Raeesi M, Aiedi H. Analysis of air conditioning system impact on a fuel cell vehicle performance based on a realistic model under actual urban conditions. Int J Hydrogen Energy. 2022;47:25899–912. https://doi.org/10.1016/j.ijhydene.2022.02.228.

[9] Hirscher M, Yartys VA, Baricco M, Bellosta von Colbe J, Blanchard D, Bowman RC, et al. Materials for hydrogen-based energy storage – past, recent progress and future outlook. J Alloys Compd. 2020;827:153548. https://doi.org/10.1016/j.jallcom.2019.153548.

[10] Gollsch M, Linder M. Influence of structural changes on gas transport properties of a cycled CaO/Ca(OH)2 powder bulk for thermochemical energy storage. J Energy Storage. 2023;73:108790. https://doi.org/10.1016/j.est.2023.108790.

[11] Stengler J, Bürger I, Linder M. Thermodynamic and kinetic investigations of the SrBr2 hydration and dehydration reactions for thermochemical energy storage and heat transformation. Appl Energy. 2020;277:115432. https://doi.org/10.1016/j.apenergy.2020.115432.

[12] Preisner NC, Linder M. A Moving Bed Reactor for Thermochemical Energy Storage Based on Metal Oxides. Energies. 2020;13. https://doi.org/10.3390/en13051232.

[13] Sakintuna B, Lamari-Darkrim F, Hirscher M. Metal hydride materials for solid hydrogen storage: A review. Int J Hydrogen Energy. 2007;32:1121–40. https://doi.org/10.1016/j.ijhydene.2006.11.022.

[14] Sandrock G. A panoramic overview of hydrogen storage alloys from a gas reaction point of view. J Alloys Compd. 1999;293-295:877–88. https://doi.org/10.1016/S0925-8388(99)00384-9.

[15] Dornheim M. Thermodynamics of Metal Hydrides: Tailoring Reaction Enthalpies of Hydrogen Storage Materials. In: Moreno Pirajáan JC, editor. Thermodynamics - Interaction Studies - Solids, Liquids and Gases. Rijeka: IntechOpen; 2011. https://doi.org/10.5772/21662.

[16] Züttel A. Materials for hydrogen storage. Mater Today. 2003;6:24–33. https://doi.org/10.1016/S1369-7021(03)00922-2.

[17] Vyazovkin S, Burnham AK, Criado JM, Pérez-Maqueda LA, Popescu C, Sbirrazzuoli N. ICTAC Kinetics Committee recommendations for performing kinetic computations on thermal analysis data. Thermochim Acta. 2011;520:1–19. https://doi.org/10.1016/j.tca.2011.03.034.

[18] Ron M. The normalized pressure dependence method for the evaluation of kinetic rates of metal hydride formation/decomposition. J Alloys Compd. 1999;283:178–91. https://doi.org/10.1016/S0925-8388(98)00859-7.

[19] Vlasenko MI, Korotenko MM, Lytvynenko SL, Pyshna DV, Morozov IA, Stratilat DP, et al. On the prospects of using metal hydrides in nuclear energy. Nucl Phys At Energy. 2020;21:308–11. https://doi.org/10.15407/jnpae2020.04.308.

[20] Dunikov D, Blinov D. Extraction of hydrogen from a lean mixture with methane by metal hydride. Int J Hydrogen Energy. 2020;45:9914–26. https://doi.org/10.1016/j.ijhydene.2020.01.201.

[21] Felbinger J, Haverich J, Bürger I, Linder M. Thermodynamic characterisation and application of the ZrNi–H metal hydride system in the low-pressure regime. J Mater Chem A. 2024;12:6075–86. http://doi.org/10.1039/D3TA06667C.

[22] Sandrock G, Suda S, Schlapbach L. Applications. In: Schlapbach L, editor. Hydrogen in Intermetallic Compunds II: Surface and Dynamic Properties, Applications. Berlin, Heidelberg: Springer Berlin Heidelberg; 1992. p. 197–258. https://doi.org/10.1007/3-540-54668-5_12.

[23] Young K. Metal Hydrides☆. Reference Module in Chemistry, Molecular Sciences and Chemical Engineering: Elsevier; 2018. https://doi.org/10.1016/B978-0-12-409547-2.05894-7.

[24] Lutz M, Linder M, Bürger I. High capacity, low pressure hydrogen storage based on magnesium hydride and thermochemical heat storage: Experimental proof of concept. Appl Energy. 2020;271:115226. https://doi.org/10.1016/j.apenergy.2020.115226.

[25] Reilly JJ, Holtz A, Wiswall RH, Jr. A New Laboratory Gas Circulation Pump for Intermediate Pressures. Rev Sci Instrum. 1971;42:1485–6. https://doi.org/10.1063/1.1684913.

[26] Lau M, Ehrensberger O, Weißgärber T, Heubner F. "Impact of hydride composite materials on thermochemical hydrogen compression". Int J Hydrogen Energy. 2024;71:562–70. https://doi.org/10.1016/j.ijhydene.2024.04.229.

[27] Lototskyy MV, Yartys VA, Pollet BG, Bowman RC. Metal hydride hydrogen compressors: A review. Int J Hydrogen Energy. 2014;39:5818–51. https://doi.org/10.1016/j.ijhydene.2014.01.158.

[28] Dornheim M, Baetcke L, Akiba E, Ares J-R, Autrey T, Barale J, et al. Research and development of hydrogen carrier based solutions for hydrogen compression and storage. Prog Energy. 2022;4:042005. https://doi.org/10.1088/2516-1083/ac7cb7.

[29] Muthukumar P, Groll M. Erratum to "Metal hydride based heating and cooling systems: A review" [International Journal of Hydrogen Energy (2010) 35: 3817–3831]. Int J Hydrogen Energy. 2010;35:8816–29. https://doi.org/10.1016/j.ijhydene.2010.04.087.

[30] Malleswararao K, Dutta P, Murthy S S. Applications of metal hydride based thermal systems: A review. Appl Therm Eng. 2022;215. https://doi.org/10.1016/j.applthermaleng.2022.118816.

[31] Golben PM, DaCosta D, Sandrock G. Hydride-based cold-start heater for automotive catalyst. J Alloys Compd. 1997;253-254:686–8. https://doi.org/10.1016/S0925-8388(96)02927-1.

[32] Kölbig M, Weckerle C, Linder M, Bürger I. Review on thermal applications for metal hydrides in fuel cell vehicles: Operation modes, recent developments and crucial design aspects. Renewable Sustainable Energy Rev. 2022;162. https://doi.org/10.1016/j.rser.2022.112385.

[33] Wolf S. Hydrogen sponge heat pump. Annual Intersociety Energy Conversion and Engineering Conference. Newark, Del. 1975

[34] Wongsuwan W, Kumar S, Neveu P, Meunier F. A review of chemical heat pump technology and applications. Appl Therm Eng. 2001;21:1489–519. https://doi.org/10.1016/S1359-4311(01)00022-9.

[35] Maeda H, Kubo H, Aoki H, Mitsui H. Compression-Type Metal Hydride Heat Pump System. Transactions of the Japan Society of Mechanical Engineers Series B. 1991;57:3925–30. https://doi.org/10.1299/kikaib.57.3925.

[36] Tao Y, Lee H, Hwang Y, Radermacher R, Wang C. Electrochemical compressor driven metal hydride heat pump. Int J Refrig. 2015;60:278–88. https://doi.org/10.1016/j.ijrefrig.2015.08.018.

[37] Kim KJ, Lloyd GM, Feldman KT, Razani A. Thermal analysis of the Ca0.4Mm0.6Ni5 metal–hydride reactor. Appl Therm Eng. 1998;18:1325–36. https://doi.org/10.1016/S1359-4311(98)00007-6.

[38] Park J-G, Jang K-J, Lee PS, Lee J-Y. The operating characteristics of the compressor-driven metal hydride heat pump system. Int J Hydrogen Energy. 2001;26:701–6. https://doi.org/10.1016/S0360-3199(01)00006-4.

[39] Park J-G, Han S-C, Jang H-Y, Lee S-M, Lee PS, Lee J-Y. The development of compressor-driven metal hydride heat pump (CDMHHP) system as an air conditioner. Int J Hydrogen Energy. 2002;27:941–4. https://doi.org/10.1016/S0360-3199(01)00187-2.

[40] Magnetto D, Mola S, DaCosta DH, Golben M, Rosso M. A Metal Hydride Mobile Air Conditioning System. SAE Trans. 2006;115. https://doi.org/10.4271/2006-01-1235.

[41] Muthukumar P, Patil MS, Raju NN, Imran M. Parametric investigations on compressor-driven metal hydride based cooling system. Appl Therm Eng. 2016;97:87–99. https://doi.org/10.1016/j.applthermaleng.2015.10.155.

[42] Jana S, Muthukumar P. Experimental studies on a closed cycle compressor operated metal hydride based cooling system with large hydrogen inventory. Int J Hydrogen Energy. 2023. 10.1016/j.ijhydene.2023.07.007.

[43] Linder M, Kulenovic R. An energy-efficient air-conditioning system for hydrogen driven cars. Int J Hydrogen Energy. 2011;36:3215–21. https://doi.org/10.1016/j.ijhydene.2010.11.101.

[44] Weckerle C, Nasri M, Hegner R, Bürger I, Linder M. A metal hydride air-conditioning system for fuel cell vehicles – Functional demonstration. Appl Energy. 2020;259. https://doi.org/10.1016/j.apenergy.2019.114187.

[45] Weckerle C, Bürger I, Linder M. Novel reactor design for metal hydride cooling systems. Int J Hydrogen Energy. 2017;42:8063–74. https://doi.org/10.1016/j.ijhydene.2017.01.066.

[46] Bürger I, Linder M. Operation strategies for gas solid reactions in thermal energy storage systems. J Energy Storage. 2021;40. https://doi.org/10.1016/j.est.2021.102767.

[47] Lee SG, Kim YK, Lee JY. Operating characteristics of metal hydride heat pump using Zr-based laves phases. Int J Hydrogen Energy. 1995;20:77–85. https://doi.org/10.1016/0360-3199(93)E0005-6.

[48] Lloyd GM, Way TR. Cooling power/efficiency diagrams for a compressor-driven metal hydride heat pump. ASHRAE Transactions. 1997;103:384–91. https://www.osti.gov/biblio/345248

[49] Weckerle C, Nasri M, Hegner R, Linder M, Bürger I. A metal hydride air-conditioning system for fuel cell vehicles – Performance investigations. Appl Energy. 2019;256. https://doi.org/10.1016/j.apenergy.2019.113957.

[50] Nagel M, Komazaki Y, Uchida M, Suda S, Matsubara Y. Operating characteristics of a metal hydride heat pump for generating cooled air. Journal of the Less Common Metals. 1984;104:307–18. https://doi.org/10.1016/0022-5088(84)90415-6.

[51] Nishizaki T, Miyamoto K, Yoshida K. Coefficients of performance of hydride heat pumps. Journal of the Less Common Metals. 1983;89:559–66. https://doi.org/10.1016/0022-5088(83)90372-7.

[52] Doerffel D, Sharkh SA. A critical review of using the Peukert equation for determining the remaining capacity of lead-acid and lithium-ion batteries. J Power Sources. 2006;155:395–400. https://doi.org/10.1016/j.jpowsour.2005.04.030.

[53] Blinov DV, Borzenko VI, Dunikov DO, Romanov IA. Experimental investigations and a simple balance model of a metal hydride reactor. Int J Hydrogen Energy. 2014;39:19361–8. https://doi.org/10.1016/j.ijhydene.2014.07.048.

[54] Lloyd GM, Razani A, Kim KJ. Performance Characteristics of a Compressor-Driven Metal Hydride Refrigerator. J Energy Res Technol. 1998;120:305–13. https://doi.org/10.1115/1.2795052.

[55] Kordel M, Radler D. Applied Metal Hydride System Optimization to Improve Hydrogen Fuel Cell System Performance in Mobile Heavy-Duty Applications. ECS Trans. 2024;114:713. https://doi.org/10.1149/11405.0713ecst.

[56] Klockow EM. Applications of Metal Hydride Heat Pumps in Hydrogen Infrastructure [Master Thesis]: Universität Stuttgart; 2022. https://elib.dlr.de/191818/.

[57] Bouché M, Richter M, Linder M. Heat transformation based on CaCl2/H2O – Part B: Open operation principle. Appl Therm Eng. 2016;102:641–7. https://doi.org/10.1016/j.applthermaleng.2016.03.102.

[58] Muthukumar P, Kumar A, Raju NN, Malleswararao K, Rahman MM. A critical review on design aspects and developmental status of metal hydride based thermal machines. Int J Hydrogen Energy. 2018;43:17753–79. https://doi.org/10.1016/j.ijhydene.2018.07.157.

[59] Weckerle C, Bürger I, Linder M. Numerical optimization of a plate reactor for a metal hydride open cooling system. Int J Hydrogen Energy. 2019;44:16862–76. https://doi.org/10.1016/j.ijhydene.2019.04.260.

[60] Linder M, Mertz R, Laurien E. Experimental results of a compact thermally driven cooling system based on metal hydrides. Int J Hydrogen Energy. 2010;35:7623–32. https://doi.org/10.1016/j.ijhydene.2010.04.184.

[61] Lee Y, Jung D. A brief performance comparison of R1234yf and R134a in a bench tester for automobile applications. Appl Therm Eng. 2012;35:240–2. https://doi.org/10.1016/j.applthermaleng.2011.09.004.

[62] Pohlmann C, Röntzsch L, Heubner F, Weißgärber T, Kieback B. Solid-state hydrogen storage in Hydralloy–graphite composites. J Power Sources. 2013;231:97–105. https://doi.org/10.1016/j.jpowsour.2012.12.044.

[63] Bürger I, Sourmelis Terzopoulos VE, Kretschmer C, Kölbig M, Brack C, Linder M. Lightweight reactor design by additive manufacturing for preheating applications using metal hydrides. Int J Hydrogen Energy. 2021;46:28686–99. https://doi.org/10.1016/j.ijhydene.2021.06.091.

[64] Lesmana LA, Lu C, Chen F, Aziz M. Triply periodic minimal surface gyroid structure as effective metal hydride hydrogen storage reactor: Experimental study. Therm Sci Eng Prog. 2023;42:101903. https://doi.org/10.1016/j.tsep.2023.101903.

[65] Sukri MF, Musa MN, Senawi MY, Nasution H. Achieving a better energy-efficient automotive air-conditioning system: a review of potential technologies and strategies for vapor compression refrigeration cycle. Energy Effic. 2015;8:1201–29. https://doi.org/10.1007/s12053-015-9389-4.